AD-A115 463 DAVID W TAYLOR NAVAL SHIP RESEARCH AND DEVELOPMENT CE--ETC F/G 20/4
KINEMATICS OF SHIP WAKE FLOW. THE SEVENTH DAVID W. TAYLOR LECTU--ETC(U)
APR 82 K WIEGHARDT
UNCLASSIFIED DTNSRDC-81/093 NL

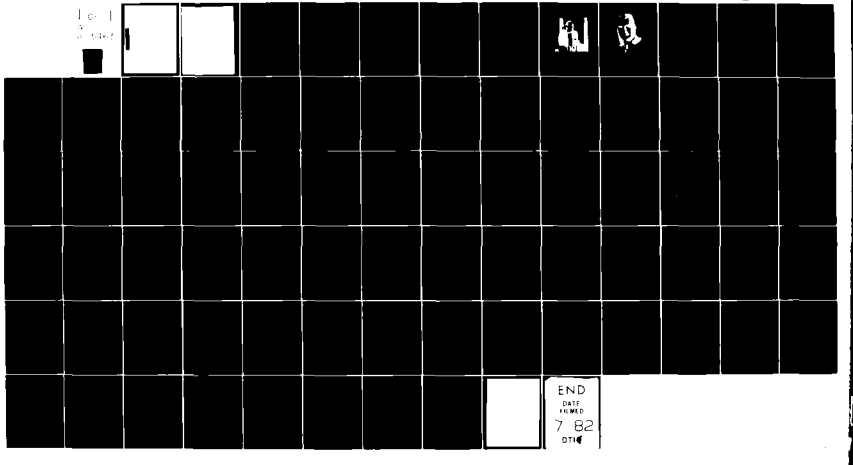

END
DATE FILMED
7 82
DTIC

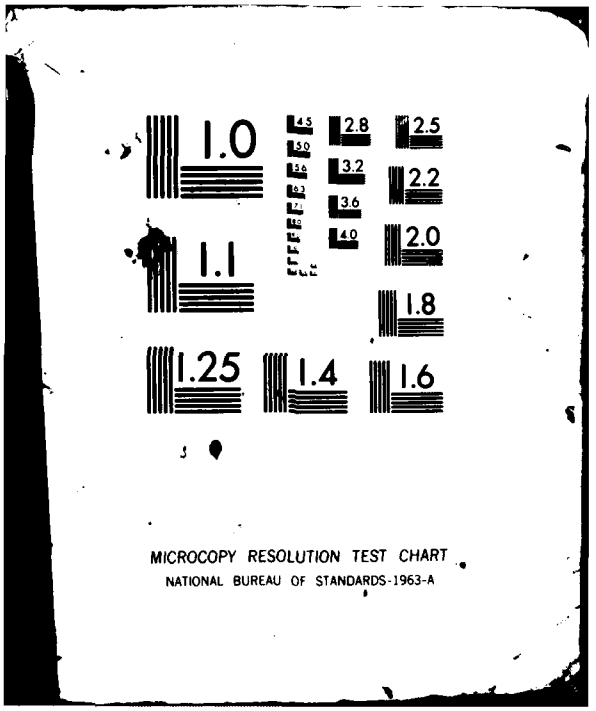
1.0
1.1
1.25
1.4
1.6
1.8
2.0
2.2
2.5
2.8
3.2
3.6
4.0
4.5
5.0
5.6
6.3
7.1
MICROCOPY RESOLUTION TEST CHART
NATIONAL BUREAU OF STANDARDS-1963-A

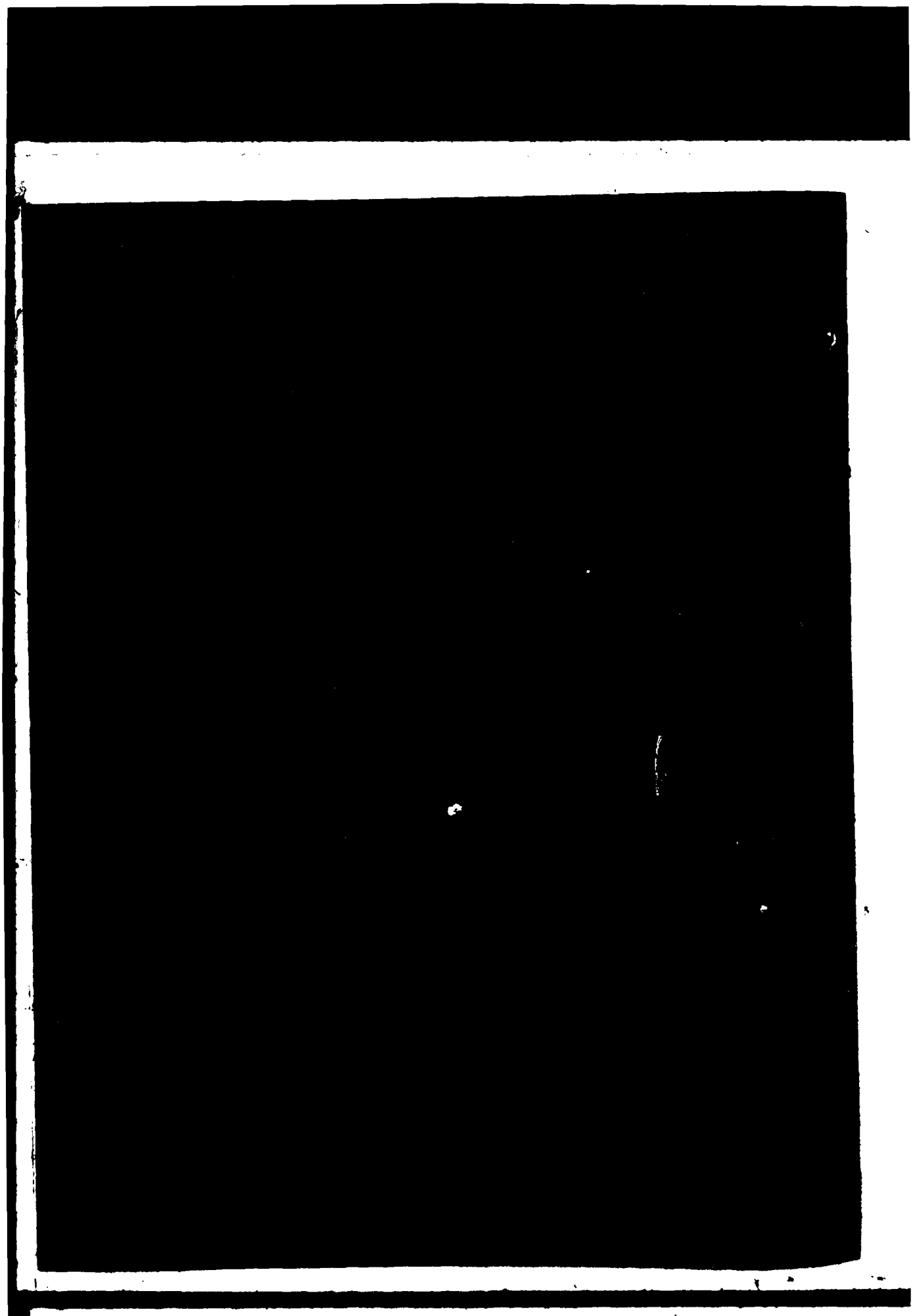

UNCLASSIFIED

SECURITY CLASSIFICATION OF THIS PAGE (When Data Entered)

REPORT DOCUMENTATION PAGE		READ INSTRUCTIONS BEFORE COMPLETING FORM
1. REPORT NUMBER DTNSRDC-81/093	2. GOVT ACCESSION NO. AD-A115 463	3. RECIPIENT'S CATALOG NUMBER
4. TITLE (and Subtitle) KINEMATICS OF SHIP WAKE FLOW THE SEVENTH DAVID W. TAYLOR LECTURES		5. TYPE OF REPORT & PERIOD COVERED Final 6. PERFORMING ORG. REPORT NUMBER
7. AUTHOR(s) Karl Wieghardt		8. CONTRACT OR GRANT NUMBER(s)
9. PERFORMING ORGANIZATION NAME AND ADDRESS		10. PROGRAM ELEMENT, PROJECT, TASK AREA & WORK UNIT NUMBERS Work Unit 1500-001
11. CONTROLLING OFFICE NAME AND ADDRESS David W. Taylor Naval Ship Research and Development Center Bethesda, Maryland 20084		12. REPORT DATE April 1982 13. NUMBER OF PAGES 76
14. MONITORING AGENCY NAME & ADDRESS(if different from Controlling Office)		15. SECURITY CLASS. (of this report) UNCLASSIFIED 15a. DECLASSIFICATION/DOWNGRADING SCHEDULE

16. DISTRIBUTION STATEMENT (of this Report)

APPROVED FOR PUBLIC RELEASE: DISTRIBUTION UNLIMITED

17. DISTRIBUTION STATEMENT (of the abstract entered in Block 20, if different from Report)

18. SUPPLEMENTARY NOTES

19. KEY WORDS (Continue on reverse side if necessary and identify by block number)

Boundary Layers
Wakes
Ship Flow

20. ABSTRACT (Continue on reverse side if necessary and identify by block number)

DD FORM 1 JAN 73 1473 EDITION OF 1 NOV 65 IS OBSOLETE
S/N 0102-LF-014-6601

UNCLASSIFIED

SECURITY CLASSIFICATION OF THIS PAGE (When Data Entered)

TABLE OF CONTENTS

	Page
LIST OF FIGURES	iii
PREFACE	vii
KINEMATICS OF SHIP WAKE FLOW	1
INTRODUCTION	1
EXPERIMENTAL FINDINGS	2
TWO VORTICITY NUMBERS	6
TRANSITION FROM ROTATIONAL TO IRROTATIONAL FLOW	7
SUMMARY	11
APPENDIX - REMARKS ON THE DEFORMATION RATE IN POTENTIAL FLOW	59
REFERENCES	63

LIST OF FIGURES

1 - Model Geometry and Divergence Data	12
2 - Cross Flow in Plane x = -858	14
3 - Cross Flow in Plane x = -157	15
4 - Cross Flow in Plane x = -73	16
5 - Cross Flow in Plane x = -53	17
6 - Cross Flow in Plane x = -38	18
7 - Cross Flow in Plane x = -19	19
8 - Cross Flow in Plane x = 0	20
9 - Cross Flow in Plane x = 50	21
10 - Cross Flow in Plane x = 100	22
11 - Cross Flow in Plane x = 200	23
12 - Isotachs of Longitudinal Velocity u in Plane x = -858	24

Page

13 - Isotachs of Longitudinal Velocity u in Plane x = -73 25

14 - Isotachs of Longitudinal Velocity u in Plane x = -53 26

15 - Isotachs of Longitudinal Velocity u in Plane x = -38 27

16 - Isotachs of Longitudinal Velocity u in Plane x = -19 28

17 - Isotachs of Longitudinal Velocity u in Plane x = 0 29

18 - Isotachs of Longitudinal Velocity u in Plane x = 50 30

19 - Isotachs of Longitudinal Velocity u in Plane x = 100 31

20 - Isotachs of Longitudinal Velocity u in Plane x = 200 32

21 - Longitudinal Vorticity at x = -157 33

22 - Longitudinal Vorticity at x = -53 34

23 - Longitudinal Vorticity at x = -19 35

24 - Longitudinal Vorticity at x = 100 36

25 - Magnitude of Vorticity $/\vec{\omega}/$ at x = -73 37

26 - Magnitude of Vorticity $/\vec{\omega}/$ and W_K at x = -19 38

27 - Magnitude of Vorticity $/\vec{\omega}/$ at x = 50 39

28 - Isobars $p/\rho\ U_\infty^2$ at x = -19 40

29 - Isobars $p/\rho\ U_\infty^2$ at x = 50 41

30 - Lines for Constant Angle between Velocity and Vorticity at x = -19 42

31 - Lines for Constant Angle between Velocity and Vorticity at x = 50 43

Page

32 - Magnitude of Acceleration $/\vec{a}/$ (Divided by U_∞) at $x = -19$ 44

33 - Longitudinal Force by Reynolds Stresses $K_1/\rho\ U_\infty^2$ vs Horizontal Wall Distance Δy at $z = -1.5$ in Various Test Planes 45

34 - Profiles of Longitudinal Velocity u and of Static Pressure $p/\rho\ U_\infty^2$ vs Horizontal Wall Distance Δy at $z = -1.5$ in Various Test Planes 46

35 - Velocities u and v in the Horizontal Plane $z = -1.5$ at Various Stations x 47

36 - Force Components K Resulting from Reynolds Stresses: Lines for K_1 = const and Arrows for Cross Component $\sqrt{K_2^2 + K_3^2}$ in the Vertical Plane $z = -1.5$ at $x = -19$ 48

37 - Magnitude of Vorticity $|\vec{\omega}_*| = |\vec{\omega}|\frac{L}{2}/U_\infty^2$ at $x/L = 0.95$ after [2] 49

38 - Kinematic Vorticity Number W_K at $x = -73$ 50

39 - Kinematic Vorticity Number W_K at $x = 50$ 51

40 - Dynamical Vorticity Number W_D at $x = -73$ 52

41 - Dynamical Vorticity Number W_D at $x = -19$ 53

42 - Dynamical Vorticity Number W_D at $x = 50$ 54

43 - Turbulent Plane Jet: Vorticity Numbers W_D and W_K for Two Velocity Profiles 55

44 - Laminar Stagnation Point Flow: Streamlines, Isobars, and Velocity Profile 56

45 - Laminar Stagnation Point Flow: Vorticity Numbers W_K and W_D 57

46 - Round Laminar Jet: Velocity Profile and W_K vs Distance from Axis 58

47 - Elliptical Strut in Potential Flow at Angle of Incidence $\gamma = 15°$: Streamlines and Lines for Constant Deformation Rate 62

PREFACE

The David W. Taylor Lectures were conceived to honor our founder in recognition of his many contributions to naval architecture and naval hydrodynamics. Admiral Taylor was a pioneer in the use of hydrodynamic theory and mathematics for the solution of naval problems. He established a tradition of applied scientific research at the "Model Basin" which has been carefully nurtured through the decades and which we treasure and maintain today. It is in this spirit that we have invited Prof. Karl Wieghardt to be a David W. Taylor Lecturer.

Prof. Wieghardt was born in Vienna, Austria, in 1913. From 1932 to 1935 he attended the Technical High School in Dresden, Germany. He began studies at the University of Göttingen in 1935 and received the degree of Dr. rer. nat. in 1938 for studies of the lift distribution on a rectangular airfoil. In 1945 he received a Dr. habil degree for research on the energy equation of boundary layers and earned the status of university lecturer. From 1938 to 1949 he was employed by the Kaiser-Wilhelm Institute for Flow Research (now the Max-Planck Institute), where he did aerodynamics and general flow research. In 1949 he went to Teddington, England, as a consultant on hydrodynamics for the Admiralty Research Laboratory. Returning to Germany three years later, he joined the faculty of the Institute for Shipbuilding at the University of Hamburg, where he has been a full professor since 1960. He is a member and past president of the German Society for Applied Mathematics and Mechanics (GAMM) and a past member of the Resistance Committee of the International Towing Tank Conference (1957-1969).

KINEMATICS OF SHIP WAKE FLOW

INTRODUCTION

For the usual merchant ship at constant speed in calm water one can calculate the wave drag approximately and even the three-dimensional boundary layer up to say 90% of the ship length. But we do not know where and how the boundary layer separates and mixes with the general secondary flow behind the ship to form the near-wake flow which the propeller has to face and which the propeller itself influences. Isotachs of the nominal or even of the effective wake can tell only part of the truth.

Along the ship, vorticity is produced in the boundary layer, and the vector $\vec{\omega} = \text{rot } \vec{v}$ lies in the vertical plane, parallel to the frame and perpendicular to the main flow. So, a vorticity line, i.e., a line parallel to the vorticity vector at any point, would just go round the hull girthwise at the parallel midship. Yet, further on in the wake, one usually finds what looks like a strong longitudinal vortex pair, even when there are no bilge vortices as with our model. Hence, our starting question was: how are these vorticity lines bent and bundled? Usual boundary-layer tests normal to the hull cannot answer this question. What we wanted was a general survey of the details of the mean flow near the stern.

For this we used a double model of a ship with block coefficient 0.85 in a wind tunnel (scale 1:95): length 2.74 m, breadth 0.404 m, depth 0.148 m, and air speed 27 m/s, giving a Reynolds number of 5 million. The model was hung up on wires in a slotted wall test section (diameter 1.2 m, length 6 m). The pressure distribution on the model corresponded very well to that of potential flow as calculated by the Hess-Smith method, except for the stern itself, of course.[1*]

Measurements were made in 12 vertical planes, x = const, at a narrow 3- by 3-mm grid in the y- and z-directions (sideward and upward). By linear numerical differentiation in the y- and z-directions and by graphical differentiation in the longitudinal x-direction all nine velocity gradients could be determined. Figure 1 shows the test planes and their sections. In some planes there were more than 1,000 test points. Basic data at each point are three velocities and the static pressure, giving nine velocity gradients and three vorticity components, i.e., 16,000 data in one single plane.

---

*A complete listing of references is given on page 63.

Obviously, such tests can be made only by on-line measuring with a computer. All these tests were made by Dr. J. Kux who also had introduced Laser-Doppler-Velocimetry (LDV) to the Hamburg Institute. However, the test probe here had to be as simple as possible. Hence, a calibrated five-hole tube (diameter 3 mm) was always held in the x-direction. Only tests with a positive pressure in the front hole were evaluated. So we have no data not only next to the body but also in the most interesting regions with the strongest cross flow, turbulence, and shear. Yet, at least, now we know where hot wire or LDV tests are mostly needed as a supplement.

It is, of course, impossible to state precise error limits for all test data. Yet, the continuity equation renders a certain control, although one must not expect too much of the sum of three differential quotients derived from measured curves. Since div $\vec{v}$ has the dimension 1/time, we divided it by the deformation rate d as shown in Figure 2 vs y for z = -1.5 mm (z=0 is the horizontal plane through the axis of the nonexisting propeller). At least for the three stern planes x = -38, -19, and 0 mm we get rather similar "curves." That is, chance errors of the differentiation must be small compared with systematic errors of the tube due to turbulence and shear at comparable side distances y. For example, for the plane x = 0, we know from LDV tests that there the local turbulence degree can be over 100%, so that the rms value of the longitudinal fluctuation is greater than the mean velocity. Besides, any tube of finite size straightens the flow in its neighborhood. Hence, in particular in the most interesting regions, we will have systematic errors. However, results found with little scatter everywhere in the flow field may be trusted, at least qualitatively.

EXPERIMENTAL FINDINGS

Figures 2 through 11 show the secondary flow in the test planes. It is directed upward and inward to the midship plane to fill the hole in the fluid which the midship has produced. The horizontal plane through the propeller axis is at z = 0, the keel at z = -44.5 mm. All velocities are normalized by U_∞, the velocity of the oncoming flow. At the end of the parallel midship, at x = -858 mm in Figure 2, no bilge vortices have formed. The blank region at $z \leq 0$ in Figures 5 through 7 indicates a separated flow region. In Figure 11 a holding strut (diam 30 mm) is to be seen.

It is amazing how smooth and repeatable these data are. Measurements were made line after line, as in TV, and the test time for each plane was more than a week. Yet, only in a few cases did differentiated quantities of one line not fit those of the neighboring lines. Usually, even in the wake, the mean flow turned out to be more stable and stationary than could be expected.

Isotachs of the longitudinal velocity component u are given for some planes in Figures 12 through 16. The distortions of a few lines near the keel are caused by the wake of a span wire under the keel of the model with a diameter of 1.2 mm at x = -380 mm. Separation seems again to begin near z = 0 (Figures 13 through 16). At the edge of this zone strong velocity gradients are to be expected.

Figures 3 through 11 of the secondary flow suggest the formation of a longitudinal vorticity component $\omega_1 = w_y - v_z$. Numerically it could easily be found by integrating the circulation around each little square 3 by 3 mm. At the end of the parallel midship (Figure 2) it is less than 5/m in our test region, i.e., at least a few millimeters off the model wall. (Since we have divided all velocities by U_∞ the dimension of our $\vec{\omega}$ is 1/m instead of 1/s.) Yet, already at x = -157 mm (Figure 21) the maximum of ω_1 is about 20/m, and this remains almost the same down into the wake at x = 100 mm (Figures 22, 23, and 24).

In Figures 22 and 23 there is also a longitudinal vorticity in the opposite, negative sense up to -5/m. To explain this, one may imagine the double model turned by 90° about the longitudinal axis; see the double model of a ship with a small breadth and a rising keel line toward the stern. Near the new keel (the former waterline) the cross flow would be smaller and it would produce negative vorticity since the tests were now made on the port instead of the starboard side.

Since the longitudinal vorticity changes so little downstream, one might, perhaps, describe it by tubes of potential vortices. In the wake these starboard and port vortices attract each other and the originally V-shaped vorticity region is folding up.

But this would not be the main point. For it turns out that the cross components of vorticity ω_2 and ω_3 are mostly much larger than the longitudinal component ω_1. In Figure 25 at x = -73 mm the magnitude of the complete vorticity vector $/\vec{\omega}/$ has a maximum value of about 80/m in the test region. At x = -19 mm (Figure 26) it is still 80/m but now at the edge of the separated region off the wall. Further downstream, in the wake, the maximum has decreased to less than 50/m (Figure 27).

Incidentally, such a region with high vorticity (and Reynolds stresses) must not be confused with a strong potential vortex with high underpressure in its core. Here, the static pressure field is rather even as Figure 28 shows for x = -19 mm. Also in the wake, at x = 50 mm (Figure 29), the pressure changes only little in spite of the high cross vorticity of the mean velocity field.

Another way to become acquainted with this intricate three-dimensional mean flow is to ask for the angle between the velocity and vorticity vectors. Since usually the velocity is directed mainly in the longitudinal x-direction, this angle is also approximately the one between x and $\vec{\bar{\omega}}$. For x = -19 mm, Figure 30 shows this angle $\sphericalangle\, \vec{\bar{v}}, \vec{\bar{\omega}}$. An acute angle is found only in the hollow groove of the section with the maximum of longitudinal vorticity ω_1. Only there is a kind of longitudinal vortex roll. Everywhere else, especially in the region with $/\vec{\bar{\omega}}/_{max}$, velocity and vorticity are almost perpendicular to each other. This is also true for the wake at x = 50 mm (Figure 31) where the angle between $\vec{\bar{v}}$ and $\vec{\bar{\omega}}$ becomes small only near the vertical midship plane due to symmetry reasons.

That velocity and vorticity are mostly perpendicular to each other, not only in any two-dimensional flow or in a boundary but also after separation in the wake and at greater distances from the wall, becomes quite trivial when looking at the time average of the Navier-Stokes equation

$$\vec{\bar{a}} = \text{grad } \vec{\bar{v}}^2/2 - \vec{\bar{v}} \times \vec{\bar{\omega}} = -\frac{1}{\rho} \text{grad } \bar{p} - \nu \text{ rot } \vec{\bar{\omega}} + \vec{\bar{K}}(\text{Re.str.})$$

where $\vec{\bar{K}}$(Re.str.) represents the resultant force due to Reynolds stresses. Contours of $/\vec{\bar{a}}/$ at x = -19 are shown in Figure 32. In wake flow, because there are still velocity differences in particular in the longitudinal component, the term grad $\vec{\bar{v}}^2/2$ is still existent. On the other hand, the static pressure field is almost level and the viscous term for the mean flow is negligible. Farther on, far away from the hull, Reynolds stresses and their resultant forces are also small. Hence, the second term $\vec{\bar{v}} \times \vec{\bar{\omega}}$ must almost cancel the first one, and this implies that the angle between $\vec{\bar{v}}$ and $\vec{\bar{\omega}}$ is not too small.

When one does trust in all these data, one may add the pressure gradients to the acceleration components to get the resultant forces of the Reynolds stresses. An example is given in Figure 33: the longitudinal force component K_1 in the

horizontal plane z = -1.5 mm vs the distance from the hull $y - y_{hull}$ at various planes of constant x. At x = -63 mm the boundary layer is still adjacent as the turbulent friction force is adverse to motion, i.e., in the negative x-direction. But at x = -53 mm this force has disappeared or is even in the positive x-direction near the wall. Hence, in this z-plane, separation seems to occur between x = -63 and -53 mm. This would be difficult to find out from velocity profiles alone as given in Figure 34: u vs wall distance $\Delta y = y - y_{hull}$, which is, of course, not the correct normal to the hull (the static pressure is fairly constant in each x-plane). Flow directions projected to the horizontal plane z = -1.5 mm are shown in Figure 35.

Another example of Reynolds forces is given in Figure 36 where lines of K_1 = -2, -4, and -8/m are shown in the plane x = -19 mm. In some points near the keel all three force components are indicated. Near the keel the Reynolds forces are directed toward the keel to compensate for the opposite gradients there (cf Figure 28) and the inertial forces. In principle, one could even try to check the hypothesis of eddy viscosity locally; but then, the velocity components would have to be differentiated twice.

At last, a remark on a *similarity rule*. Professor Mori, Hiroshima, has told us that he had also found high cross vorticity near the stern of a towed 3-m model as published in 1975.[2] Some of his results are plotted in Figure 37 where $/\vec{\omega}_*/ = L/2\ |\vec{\omega}|/U_\infty$ with L = model length. To compare these tests in water with ours in air, we use U_∞ and the boundary-layer thickness δ at the end of the model corresponding to the end of a flat plate with the same length

$$\delta = 0.085\ L\ Rn^{-0.1} \pm 3\% \text{ for } 10^6 \leq Rn \leq 10^9$$

as derived from measurements by Winter and Gaudet.[3] Then the maximum for $|\vec{\omega}|\delta/U_\infty$ is 4 for our double model in air and 2.6 for the Japanese model in water with a coarser test grid. Hence, at least for the order of magnitude one may expect for a ship with L = 200 m, U = 7.1 m/s, Fn = 0.16, $Rn = 1.2 \cdot 10^9$, and δ = 2.1 m a cross vorticity up to 10/s.[4]

TWO VORTICITY NUMBERS

The most spectacular test result is the region with high cross vorticity. Yet, when can we speak of high or low vorticity? Strictly speaking this question does not make sense because vorticity has a dimension, namely 1/s or here, after division with U_∞ 1/m. Only with solid bodies, quantities such as strain, torsion, or shear are dimensionless; with fluids they are rates. Hence, C. Truesdell[5] introduced a local, kinematic vorticity number W_K where

$W_K = |\vec{\omega}|/d$ = magnitude of vorticity over deformation rate, $(d^2=\vec{\omega}^2+2 \text{ div } \vec{a})$,

$\vec{a}$ = acceleration in stationary flow, or

$\vec{a}$ = grad $\vec{v}^2/2 - \vec{v} \times \vec{\omega}$, or written in full

$$d^2 = \underbrace{2(u_x^2+v_y^2+w_z^2)}_{\text{"strains"}} + \underbrace{(w_y+v_z)^2 + (u_z+w_x)^2 + (v_x+u_y)^2}_{\text{"shears"}}$$

For example, for a straight vortex line with peripheral velocity proportional to $(\text{radius})^n$ this number becomes $W_K = |n+1/n-1|$. Hence, for the potential vortex with $n = -1$, $W_K = 0$, of course, but for a rotating rigid body without any deformation $n = 1$ and $W_K \to \infty$. In pure shear flow and hence in any tube flow (laminar or turbulent) $W_K = 1$ exactly because there is no acceleration and no div $\vec{a}$. In a boundary layer W_K is practically also equal to 1, but only approximately.

Applying this measure to the mean velocity field of our turbulent stern flow yields the lines W_K in Figures 38, 26, and 39 for the planes x = -73, -19, and 50 mm. The region with the highest $|\vec{\omega}|$-values has become "invisible," since here W_K is everywhere between 0.75 and 1; i.e., almost all deformation is due to vorticity and div $\vec{a}$ is positive but small compared with $\vec{\omega}^2$.

On the other hand, in the hollow groove of the sections a longitudinal vortex roll is formed and marked by a maximal value of $W_K \simeq 2$ at x = -19 (Figure 26). Here, there is more rotation than deformation of the fluid particles and div $\vec{a}$ is negative.

At greater wall distances and in particular later in the wake, W_K decreases to and below 0.5 at the edge of the test range. Obviously, the fluid particles

originally contaminated with vorticity produced in the boundary layer have been diluted by the nonrotating particles swept into the wake from outside by the secondary transverse flow.

C. Truesdell[5] was also looking for a simple local measure indicating the magnitude of error one would make in calculating a laminar flow by neglecting vorticity or assuming potential flow. As a dynamic vorticity number he defined

$$W_D = \frac{|\vec{v}\times\vec{\omega}|}{\left|\frac{\partial\vec{v}}{\partial t} + \text{grad } \vec{v}^2/2\right|}$$

or for stationary flow simply

$$W_D = |\vec{v}\times\vec{\omega}| / |\text{grad } \vec{v}^2/2|$$

For a straight vortex line with peripheral velocity proportional to r^n, $W_D = |(n+1)/n|$, i.e., for the potential vortex with $n = -1$, $W_D = 0$ for $r > 0$, yet for a fluid rotating like a rigid body, $n = 1$ and $W_D = 2$. (In incompressible airfoil or propeller theory the free vortices leave along streamlines so that $\vec{v} \| \vec{\omega}$ and $W_D=0$ everywhere.) Where there is no acceleration, e.g., in stationary tube flow, $W_D = 1$. Again, in a boundary layer W_D is nearly 1.

The distribution of W_D in our stern flow is shown in Figures 40, 41, and 42 for $x = -73$, -19 and 50 mm. In the region with the highest $|\vec{\omega}|$-values, W_D is also about 1, similar to W_K. Again, only in the longitudinal vortex roll does W_D reach a maximum of up to 2 (Figure 42). Yet, it should be mentioned that the calculation of W_D showed more scatter than that of W_K. Hence, quantitatively these maximal values of W_D are probably not as reliable as those of W_K.

However, it may be concluded that in a wide region W_D is near to 1 and at the edge of stern flow and wake, W_D also decreases at least to about 0.5 in the test region, as does W_K.

TRANSITION FROM ROTATIONAL TO IRROTATIONAL FLOW

The decay of W_K and W_D at greater distances from the body seems quite trivial. Inside a boundary layer or wake the deformation consists mainly of rotation, but in

the potential flow outside there is only deformation (and change of kinematic energy $\rho\vec{v}^2/2$) but no longer rotation. Yet, surprisingly, in this respect the test results are more precise than all boundary-layer calculations, simply because the usual assumptions of boundary-layer theory (e.g., $\partial v/\partial x << \partial u/\partial y$) do not hold any longer at the edge of the boundary layer. There, the asymptotic transition into the outer potential flow is described correctly only to the first order for the velocities but not for the velocity gradients. Already Blasius' solution for the flat plate gives $\text{div}\ \vec{a} \leq 0$ everywhere and hence $W_K \geq 1$ for any wall distance.

The same deficiency is found with solutions for free plane flows of a boundary layer nature, meaning that the region of space in which a solution is being sought does not extend far in a traverse direction as compared with the main direction of flow, whether these flows are laminar or turbulent.

For such stationary plane flows with similarity solutions the stream function is[6,7]

$$\psi = C\, x^n F(\eta), \text{ resp } Uy - C\, x^n F(\eta) \text{ for wake flow, } \eta = \sigma y \cdot x^k$$

Then the divergence of acceleration is

$$2\ \text{div}\ \vec{a} = 4\ C^2\sigma^2 x^{2(n+k-1)} \cdot \{(n+k)^2 F'^2 + k(k+1)\eta F'F'' - n(n-1)F \cdot F''\}$$

and $W_K = |\vec{\omega}|/d = 1/\sqrt{1+2(\text{div}\ \vec{a})/\vec{\omega}^2}$

Examples are as follows:

1. Boundary layer along a flat plate: $n = 1/2$, $k = -1/2$, $2\ \text{div}\ \vec{a} = U^2 x^{-2}(F - \eta F')\ F'' \leq 0$ and $W_K \geq 1$ everywhere.

2. The smoothing out of a velocity discontinuity or the boundary of a plane turbulent jet: $n = 1$, $k = -1$ and $\text{div}\ \vec{a} = 0$ and $W_K = 1$ everywhere and even for any function $F(\eta)$ or any velocity profile F'.

3. Laminar free jet: $n = 1/3$, $k = -2/3$, $F = \tanh \eta$, $2\ \text{div}\ \vec{a} \sim F'^2 - 2\eta F'F'' + 2\ F\ F'' \leq 0$ and $W_K \geq 1$ for $\eta \geq 0.794$.

4. Turbulent free jet: $n = 1/2$, $k = -1$; approximation functions for ψ:

$F_1 = \tanh \eta$ gives $W_K \geq 1$ for $\eta \geq 0.658$

$F_2 = \frac{1}{\sqrt{\beta}} \int_0^{\eta\sqrt{\beta}} e^{-t^2}\, dt$ $W_K \geq 1$ for $\eta \geq 0.571$, as shown in Figure 43.

5. Plane wake, laminar or turbulent: $n = 0$, $k = -1/2$ and $F = \int e^{-\eta^2}\, d\eta$.

Similarity is found experimentally for $Ux/4\varepsilon > 600$ with ε = kinematic or eddy viscosity; then $2(\text{div } \vec{a})/\vec{\omega}^2 < 0.001$ or $W_K > 0.999_5$.

Unfortunately, for the transition from rotational to irrotational flow there is only one exact example known, namely the stagnation point flow. It is again a similarity solution and for plane laminar flow $n = 1$, $k = 0$, $\psi = \nu\, \xi F(\eta)$ with $\xi = x\sqrt{a/\nu}$, $\eta = y\sqrt{a/\nu}$ and $F'''+F\cdot F''-F'^2+1 = 0$. Here, $2 \text{ div } \vec{a} = 4\, a^2 F'^2 \geq 0$ or $W_K \leq 1$. As shown in Figures 44 and 45, W_K and W_D are both 1 at the wall, and they decrease monotonously with wall distance to zero. The axisymmetric stagnation point flow also shows this expected behavior.

Another exact solution of which one might think in this connection is the one for the flow in a convergent or divergent channel. There is only a radial velocity $\nu\, f(\alpha)/r$ (in polar coordinates) with $\omega = -\nu\, f'(\alpha)/r^2$ and $2 \text{ div } \vec{a} = 4\, \nu^2 f^2(\alpha)/r^4 \geq 0$. At the walls $f = 0$, $f' \neq 0$, $W_K = 1$; at the center plane $f \neq 0$, $f' = 0$, $W_K = 0$. (Only in the limiting case of flow between two parallel walls is there pure shear flow without acceleration and $W_K = 1$ everywhere.) Yet, there is no transition to irrotational flow. At the center plane W_K must vanish for symmetry reasons, since ω is changing sign there, just as it does at the center plane of a jet or wake.

A more pertinent example is the round laminar jet: in spherical polar coordinates $\psi = \nu\cdot R\cdot f(\eta = \cos\theta)$ with $f = 2(1-\eta^2)/(\varepsilon+1-\eta)$ and $\varepsilon << 1$. Figure 46 gives the velocity distribution in usual cylindrical coordinates, i.e., the axial component $u = v_R \cos\theta - v_\theta \sin\theta$ vs radial distance from the axis $r = R \tan\theta$ over $b = R \tan\theta_*$ with $u/u_o = 0.5$ at $r = b$. The arbitrary constant ε is assumed to be $\varepsilon = 0.01$ as in Reference 7, corresponding to $M/\rho\nu^2 = 3282.5$ with M = momentum of the jet; then $\theta_* = 5.184°$. W_K is about 1 in a wide range, viz., $W_K = 1 \pm 5\%$ for $0.3 < r/b < 4.6$ where u/u_o falls from 0.93 to 0.01. Only at greater axial distances W_K decays; e.g., $W_K = 0.5$ for $r/b = 6.67$ where $u/u_o = 0.0037$. In this special case the approximate "boundary layer solution" corresponds precisely to the limit of the exact solution for $\varepsilon \to 0$. For small angles θ near the axis f becomes $\xi^2/(1+\xi^2/4)$ with

$\xi = \theta\sqrt{2/\varepsilon} = \theta/4\nu\ (3/\pi\ M/\rho)^{1/2}$, since for $\varepsilon \to 0$ $M/\rho\nu^2 \to 32\ \pi/3\varepsilon$. This yields $u/u_o = 1/[1+(\sqrt{2}-1)(r/b)^2]^2$. Within the accuracy of drawing, both curves for u/u_o and W_K from this solution are indiscernible from those of the exact solution, though, for example, at $r/b = 6.67$, the approximate solution gives again $W_K = 0.5$ but $u/u_o = 0.0026$ instead of 0.0037.

For turbulent flow there are no exact solutions and here the transition from rotational to irrotational outer flow is obscured by intermittency anyway. Farther on, the vorticity numbers W_K and W_D derived from the acceleration $\bar{\vec{a}}$ and rotation $\bar{\vec{\omega}}$ of the mean velocity field are, perhaps, somewhat artificial physical quantities. Possibly, it would be more appropriate to use mean values of the real acceleration $\bar{\vec{a}}_*$ and rotation $\sqrt{\bar{\vec{\omega}}^2+\overline{\vec{\omega}'^2}}$; with $\vec{v}'$ and $\vec{\omega}'$ velocity and vorticity fluctuation

$$\bar{\vec{a}}_* = \text{grad}\left(\bar{\vec{v}}^2+\overline{\vec{v}'^2}\right)/2 - \overline{(\bar{\vec{v}}+\vec{v}') \times (\bar{\vec{\omega}}+\vec{\omega}')}$$

$$= \bar{\vec{a}} + \text{grad}\ \overline{\vec{v}'^2}/2 - \overline{\vec{v}'\times\vec{\omega}'} = -\frac{1}{\rho}\ \text{grad}\ \bar{p} - \nu\ \text{rot}\ \bar{\vec{\omega}}$$

Then the divergence of the mean of the real acceleration $\bar{\vec{a}}_*$ gives, as for laminar flow, simply

$$\text{div}\ \bar{\vec{a}}_* = -\Delta\bar{p}/\rho$$

At higher Reynolds numbers the viscous term ν rot $\bar{\vec{\omega}}$ is negligible, as has been checked in our tests; then, there exists an acceleration potential for $\bar{\vec{a}}_*$ namely $-\bar{p}/\rho$ + const. However, in order to determine "real" vorticity numbers, e.g., W_{K*}

$$W_{K*} = 1/\sqrt{1+2(\text{div}\ \bar{\vec{a}}_*)/\left(\bar{\vec{\omega}}^2+\overline{\vec{\omega}'^2}\right)}$$

one would have to know not only the mean velocity field in all details but the complete tensor of Reynolds stresses as well.

See the appendix for the deformation rate in potential flow.

SUMMARY

The stern flow and the near wake of the double model of a full ship in a wind tunnel have been measured at so many points that not only the mean velocity field but also all nine velocity gradients could be determined with sufficient accuracy. Not only in the boundary layer still adjacent to the hull but also after separation and in the near wake the velocity and vorticity vectors are mostly nearly perpendicular to each other. There is a region with especially strong cross vorticity of the order of up to 10/s to be expected on a large ship.

Two vorticity measures of C. Truesdell, W_K and W_D, are used to analyze this turbulent flow. There is a wide region with W_K and W_D near to one, and outward to the edge of stern flow or wake both vorticity numbers decay. This transition from rotational to irrotational flow is not described by known similarity solutions for laminar or turbulent jets and wakes because the usual boundary layer assumptions do not hold at the edge. Only the exact solution for laminar stagnation point flow yields correctly $W_{K,D} \to 0$ for increasing wall distance. Since the region with decreasing $W_{K,D}$ is very large for near-wake flow, as shown by these tests, an analytical study of such transition from inner rotational to outer potential flow seems necessary for a realistic description of wake flow.

Figure 1 - Model Geometry and Divergence Data

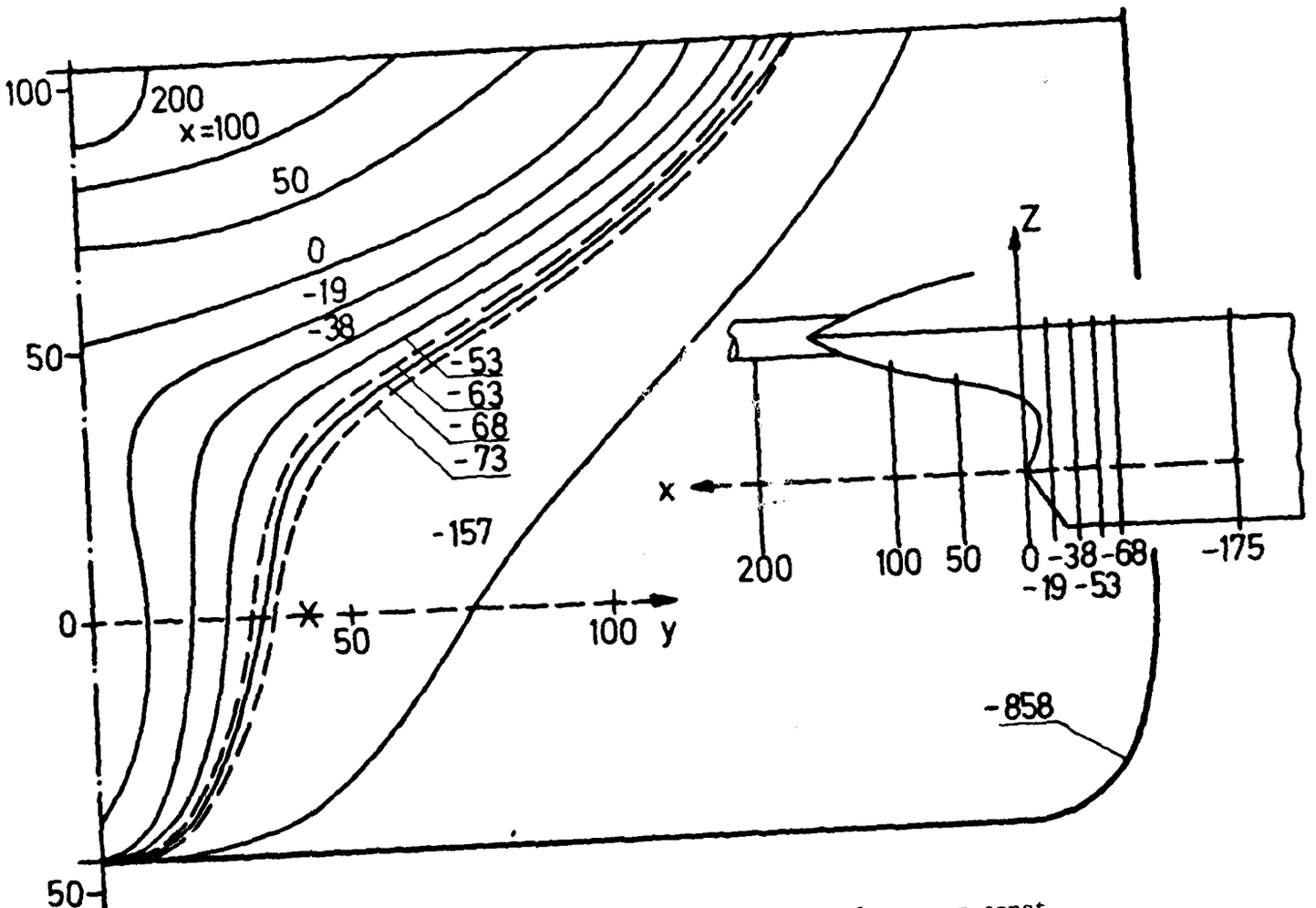

Figure 1a - Model Body Sections for Test Planes x = const

Figure 1 (Continued)

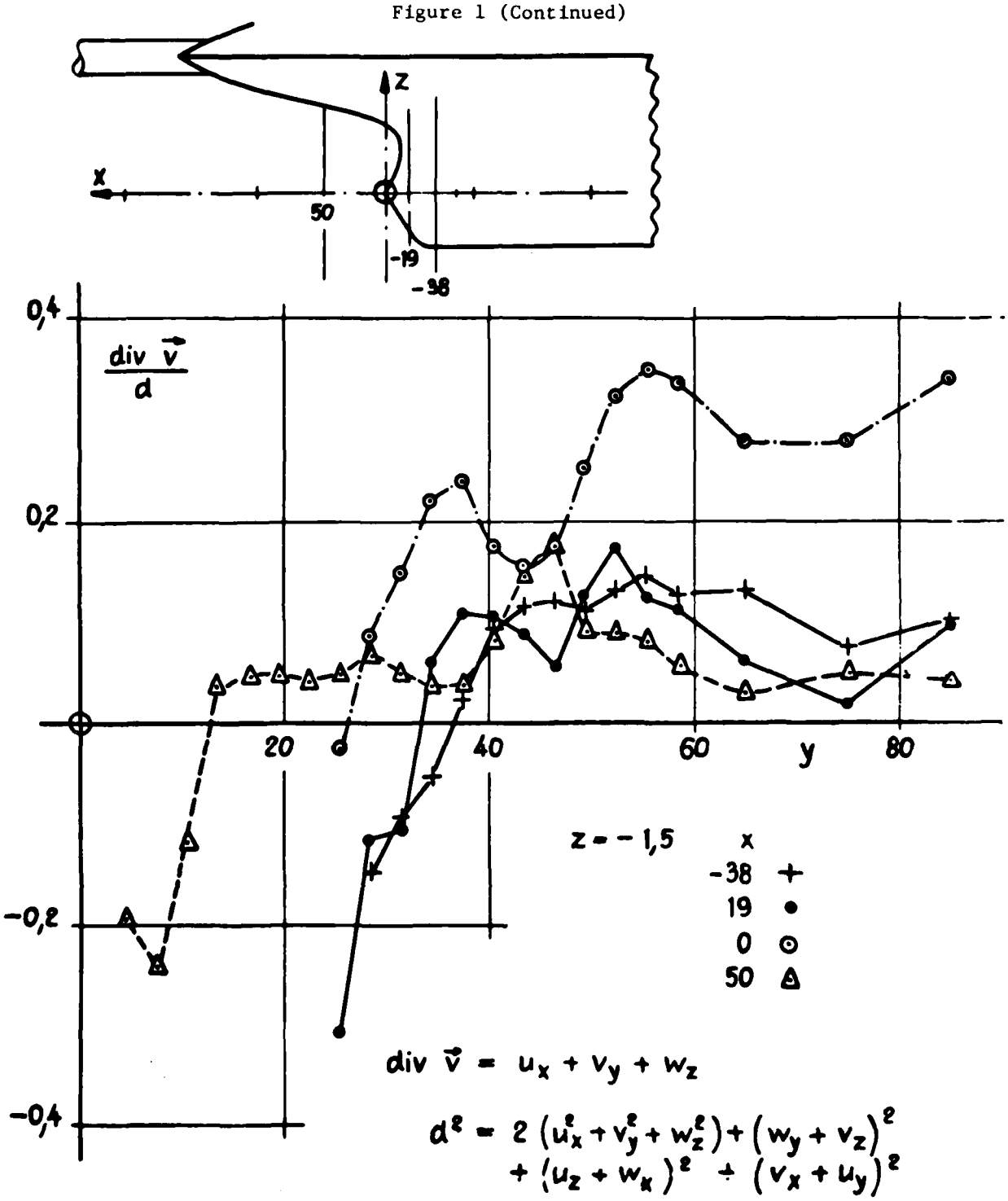

Figure 1b - Deviations of Test Data from Continuity Equation

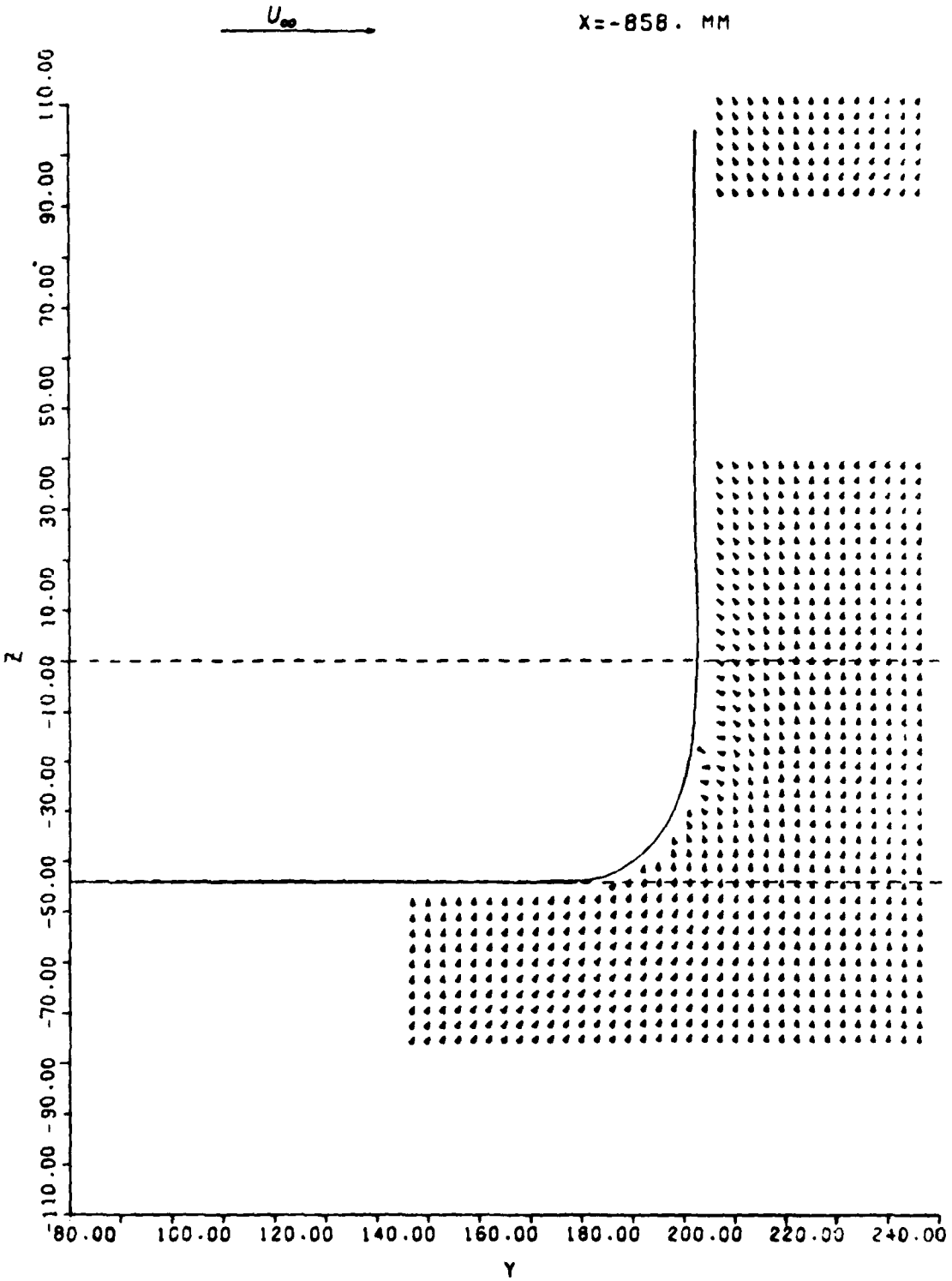

Figure 2 - Cross Flow in Plane x = -858

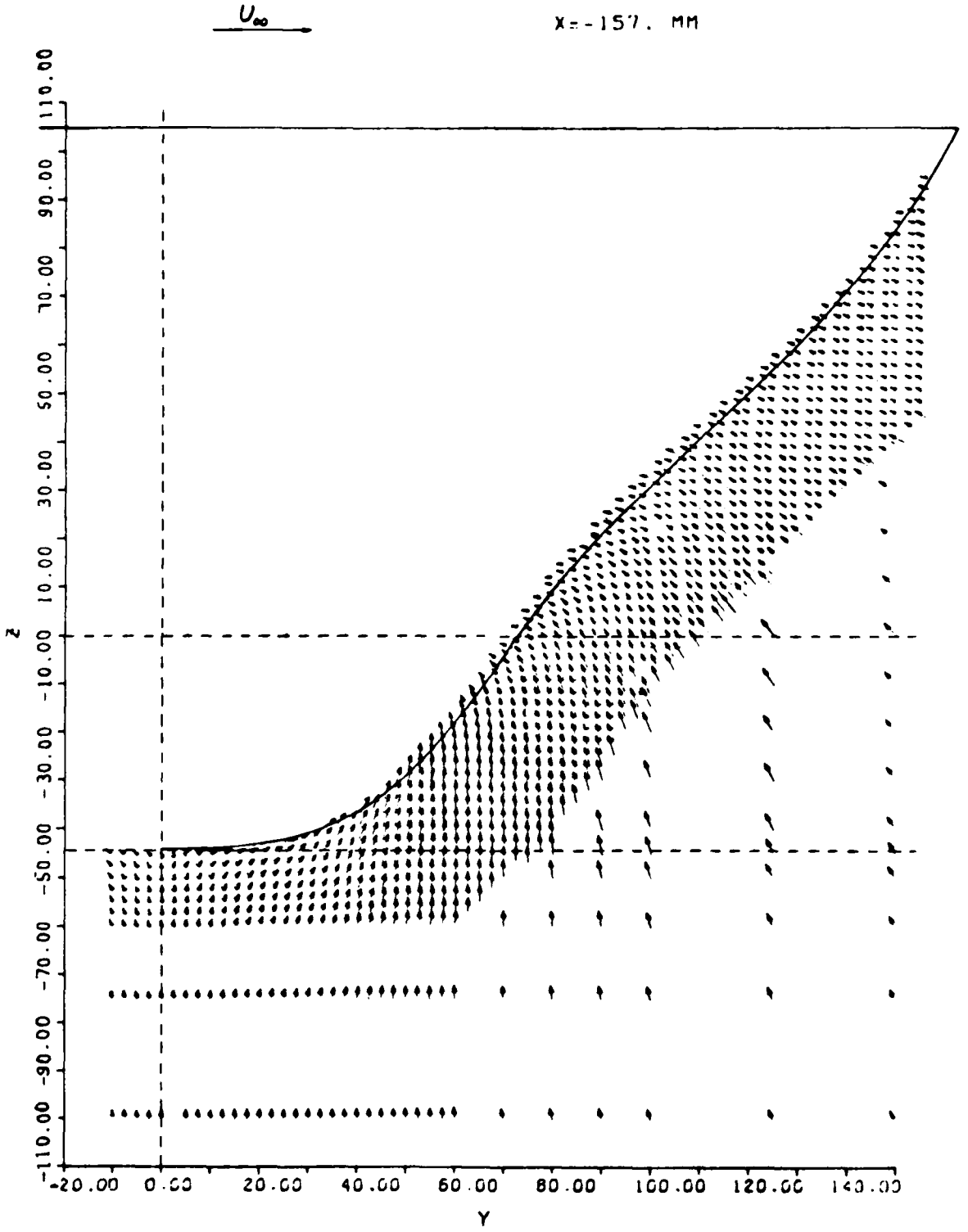

Figure 3 - Cross Flow in Plane x = -157

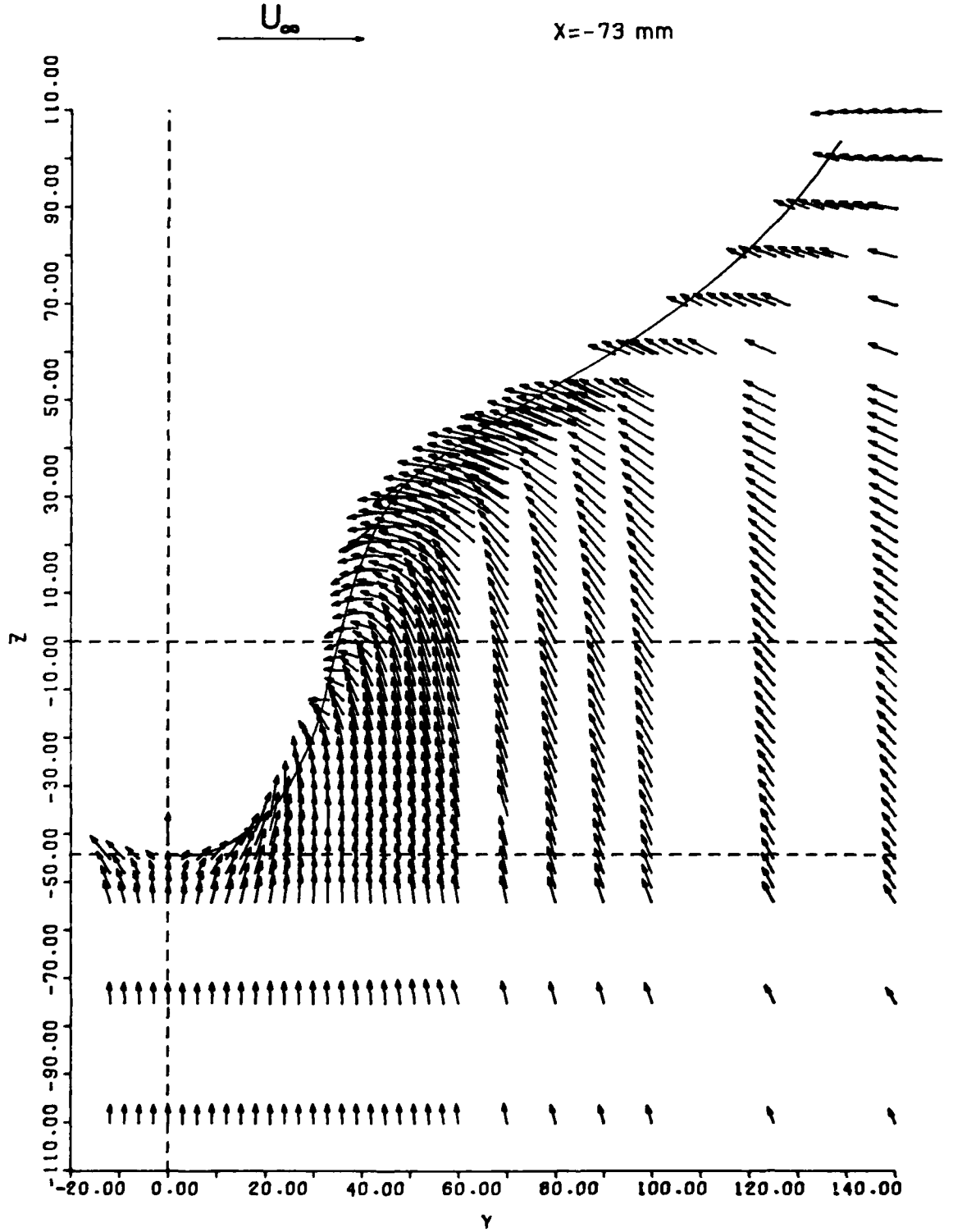

Figure 4 - Cross Flow in Plane x = -73

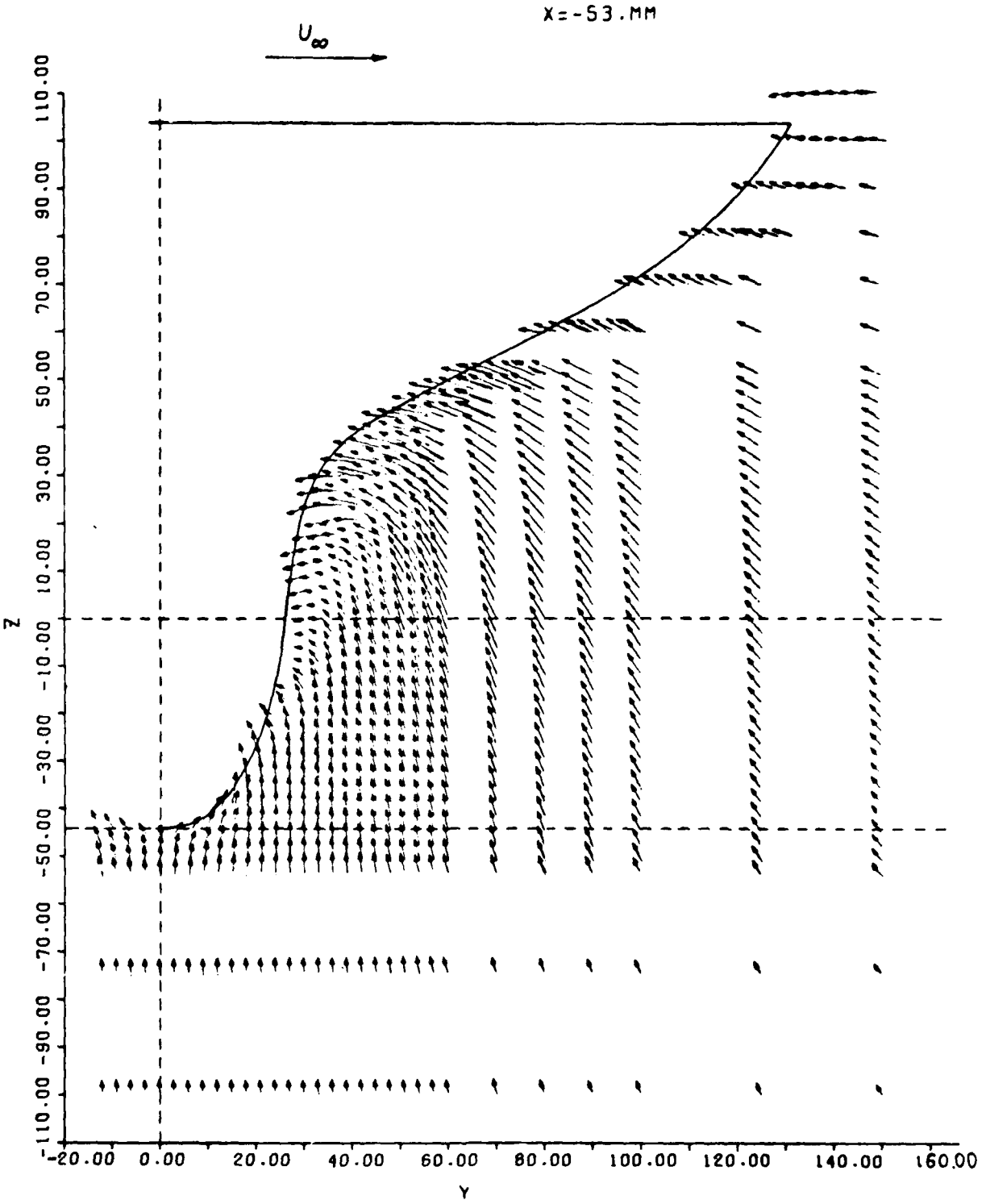

Figure 5 - Cross Flow in Plane x = -53

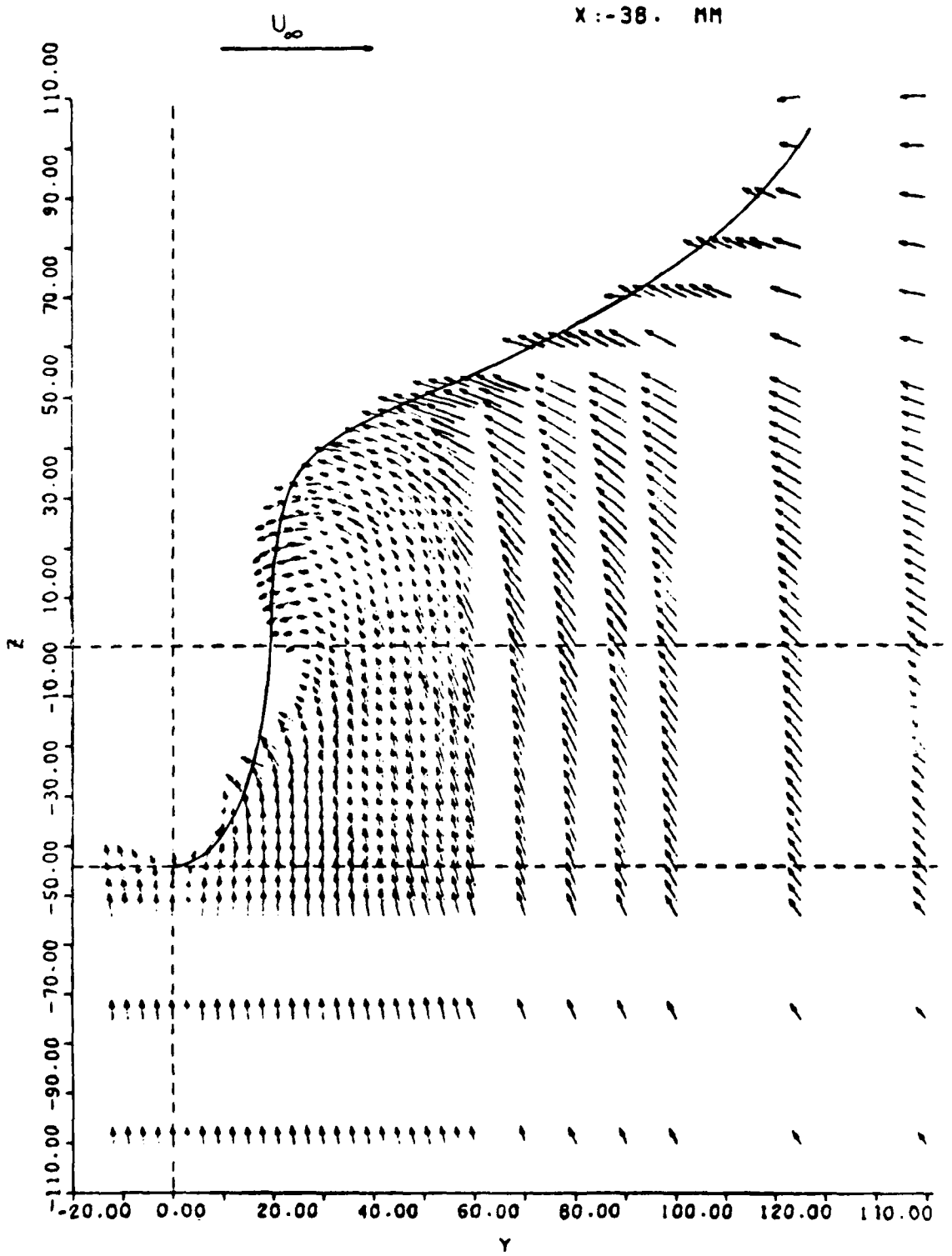

Figure 6 - Cross Flow in Plane x = -38

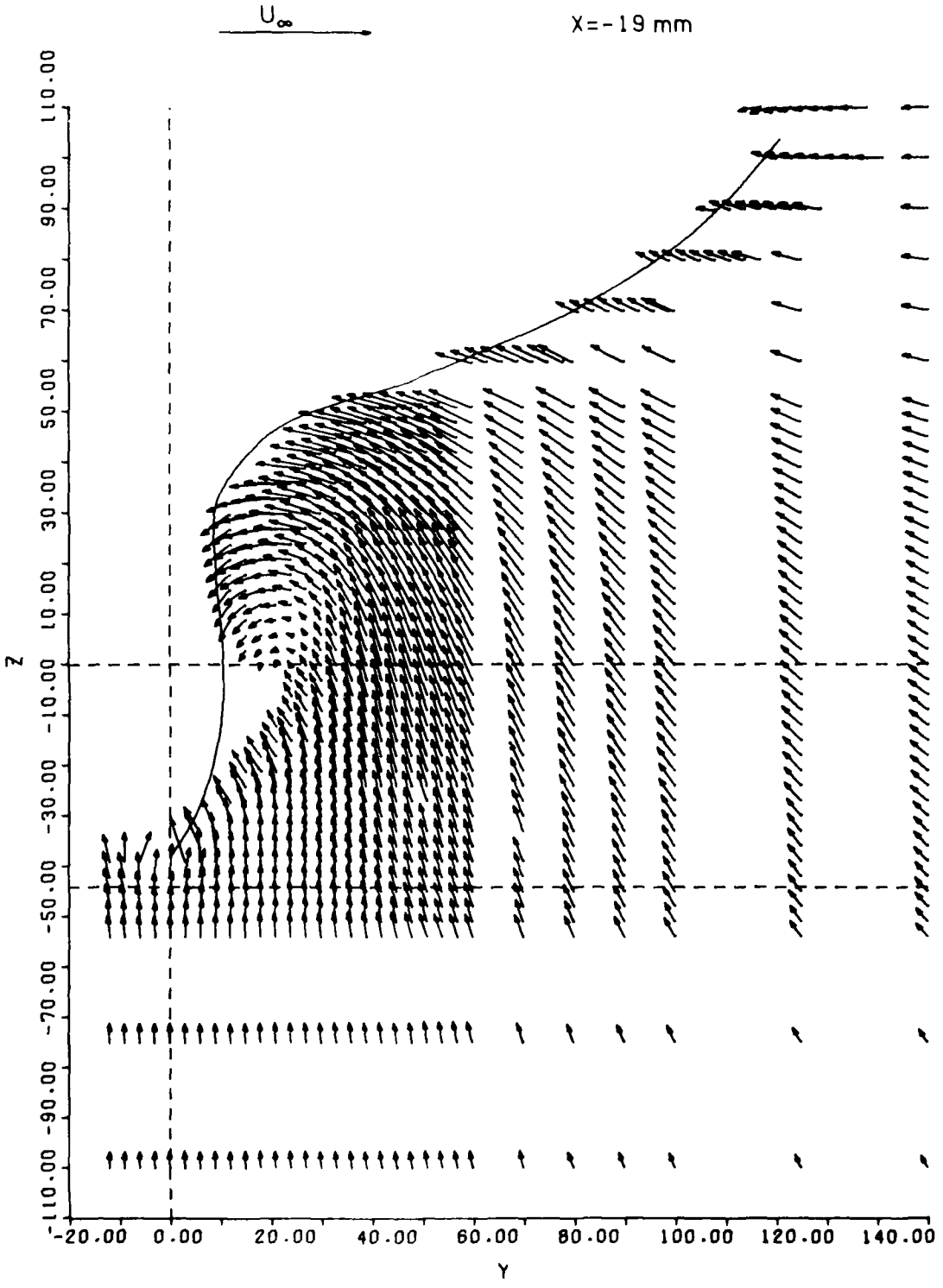

Figure 7 - Cross Flow in Plane x = -19

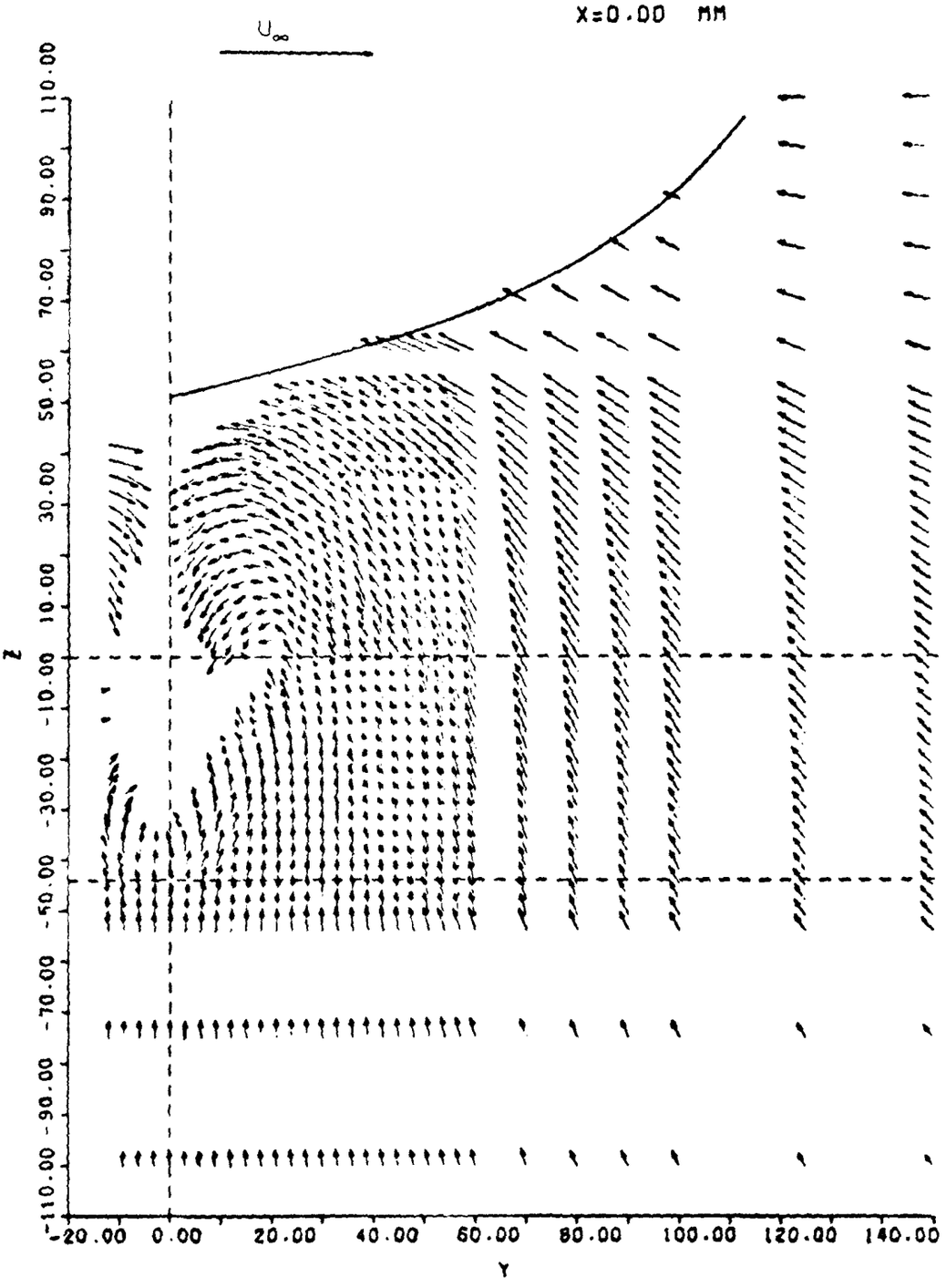

Figure 8 - Cross Flow in Plane x = 0

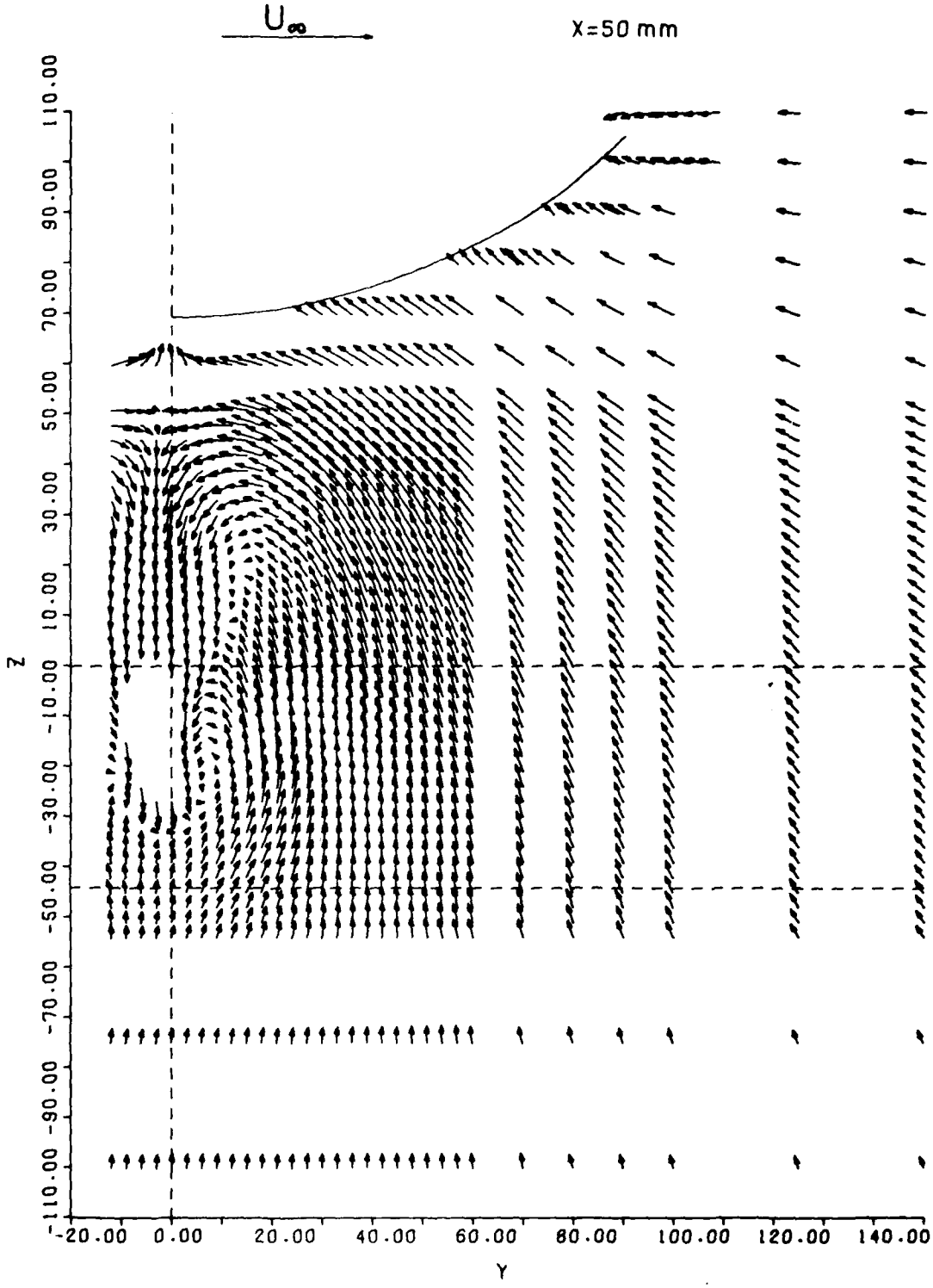

Figure 9 - Cross Flow in Plane x = 50

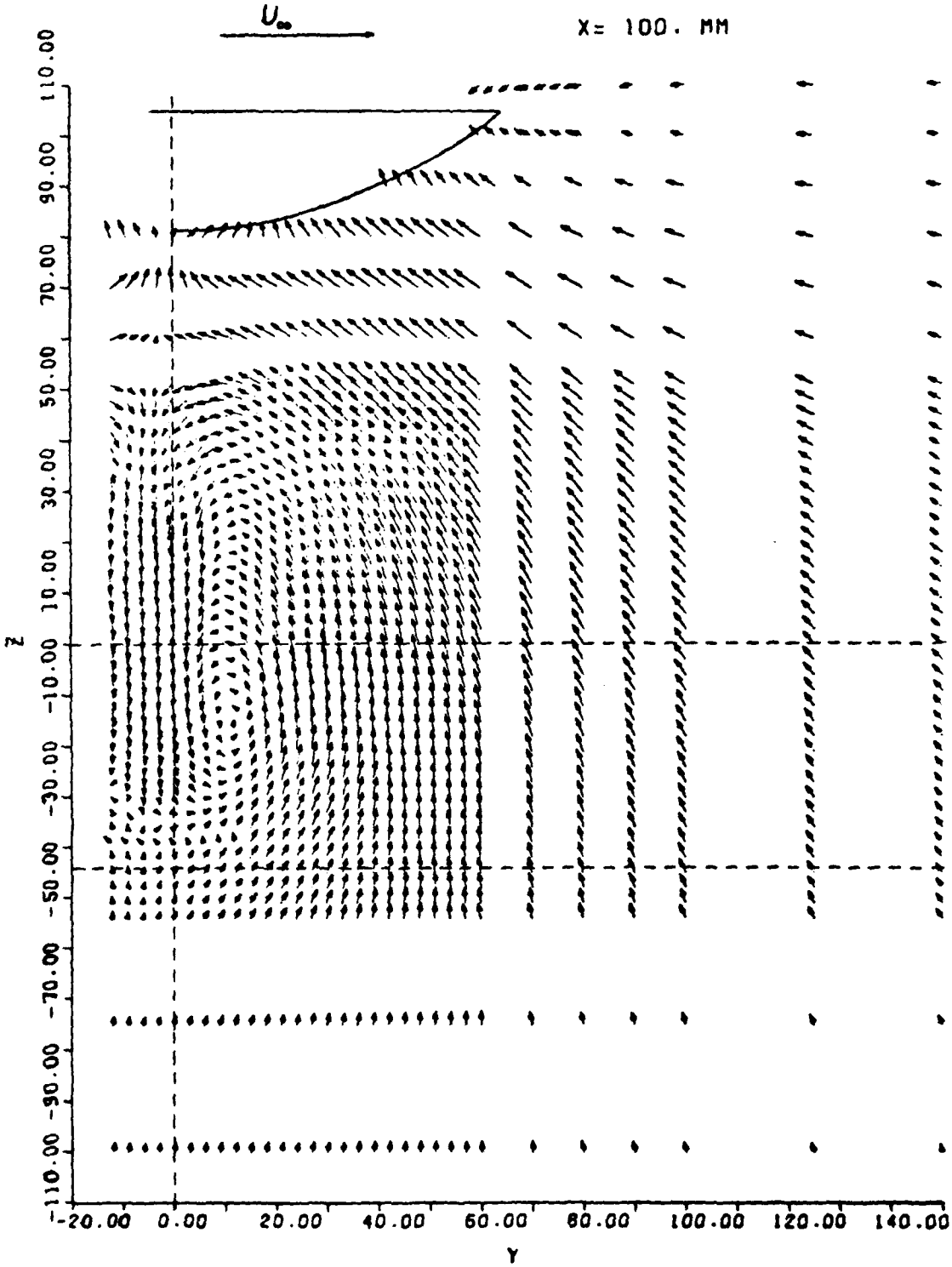

Figure 10 - Cross Flow in Plane x = 100

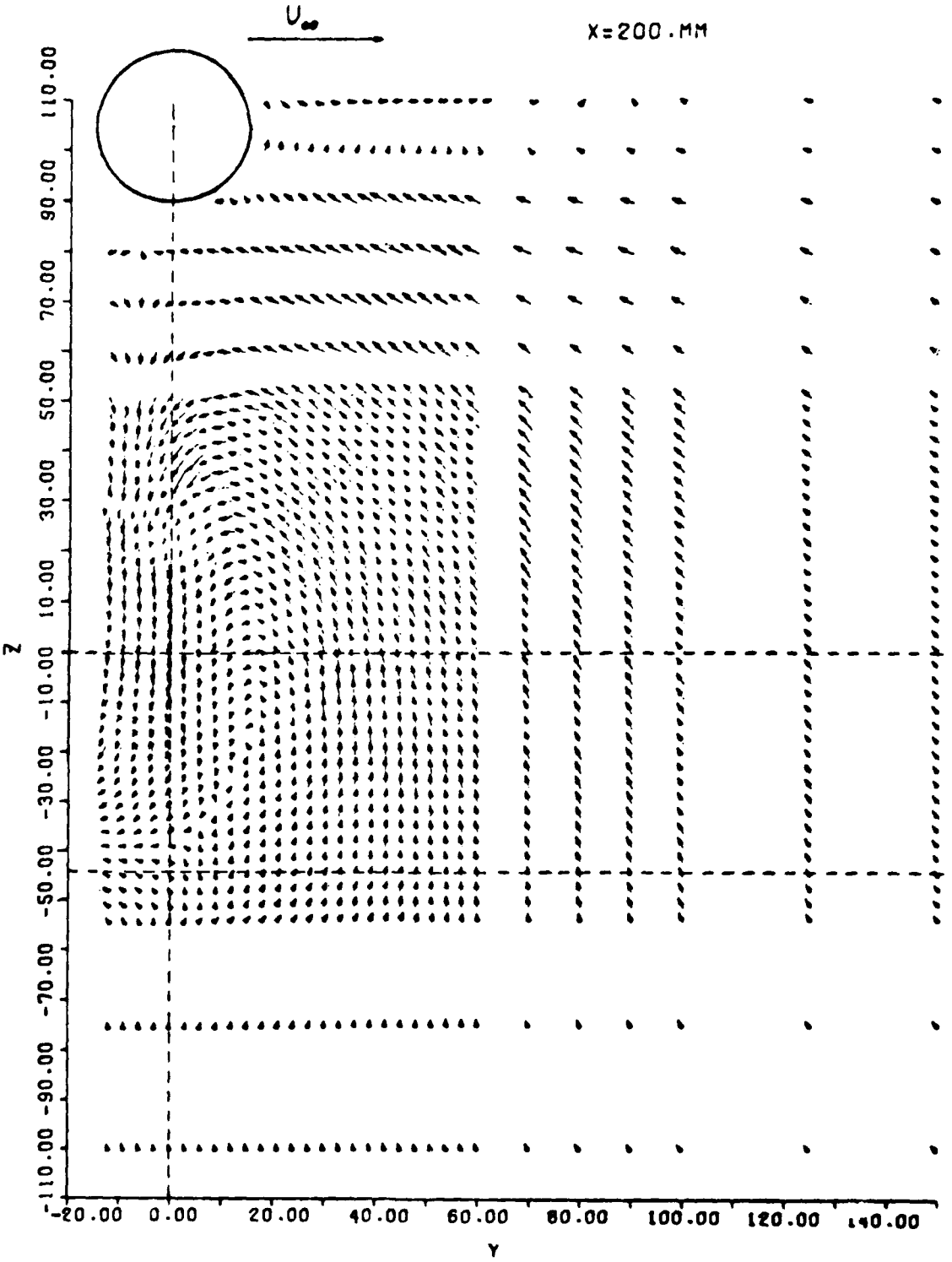

Figure 11 - Cross Flow in Plane x = 200

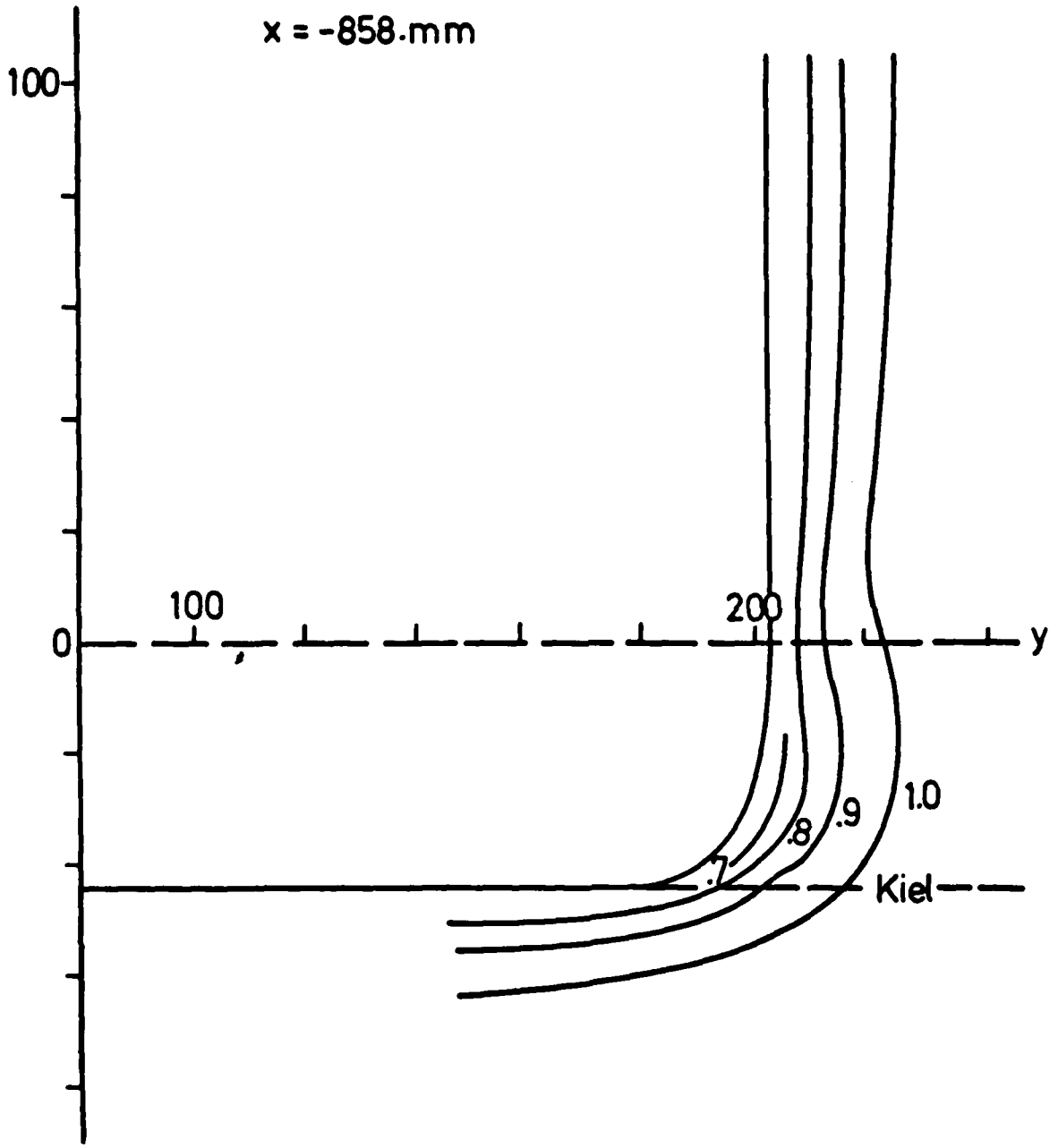

Figure 12 - Isotachs of Longitudinal Velocity u in Plane x = -858

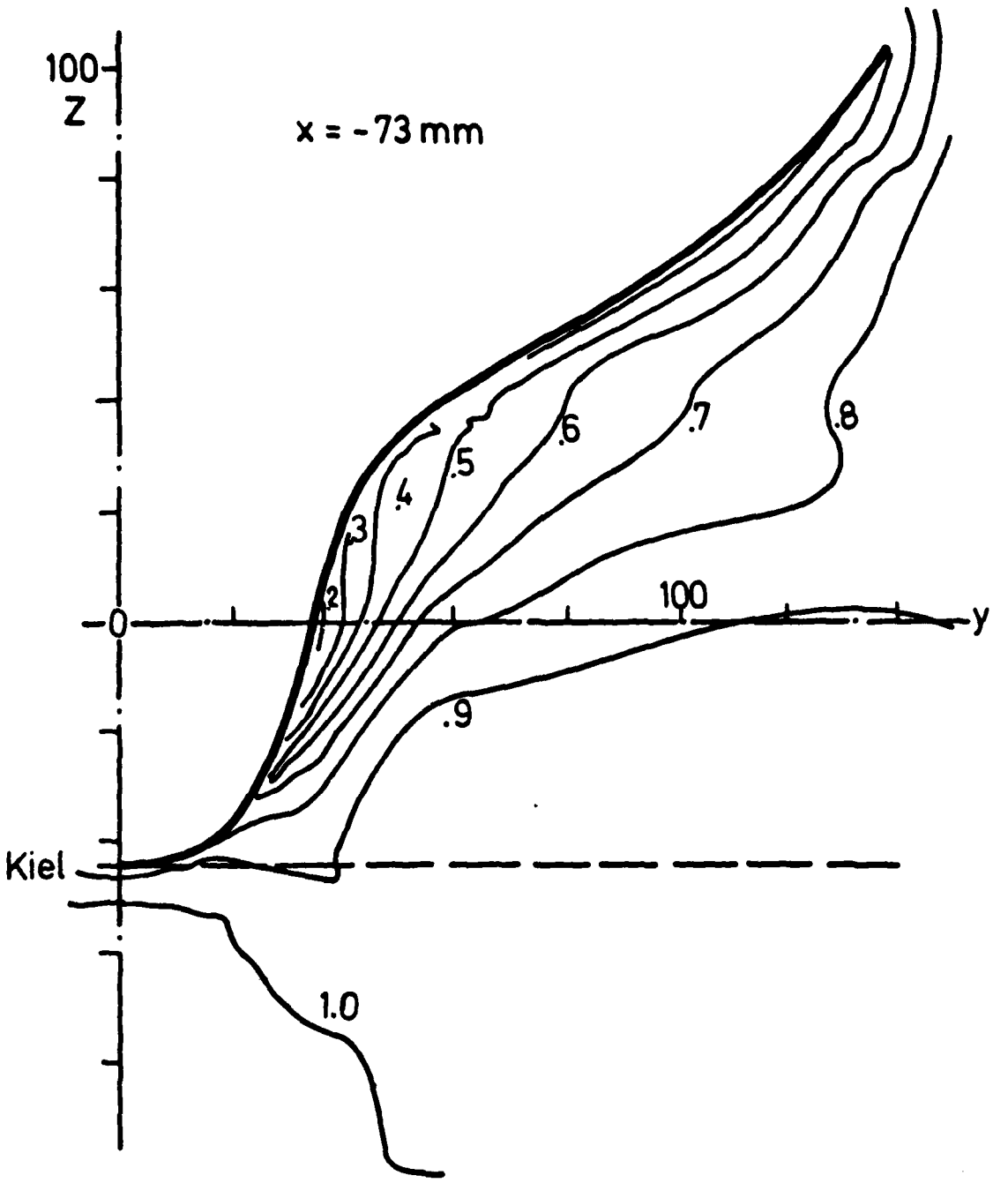

Figure 13 - Isotachs of Longitudinal Velocity u in Plane x = -73

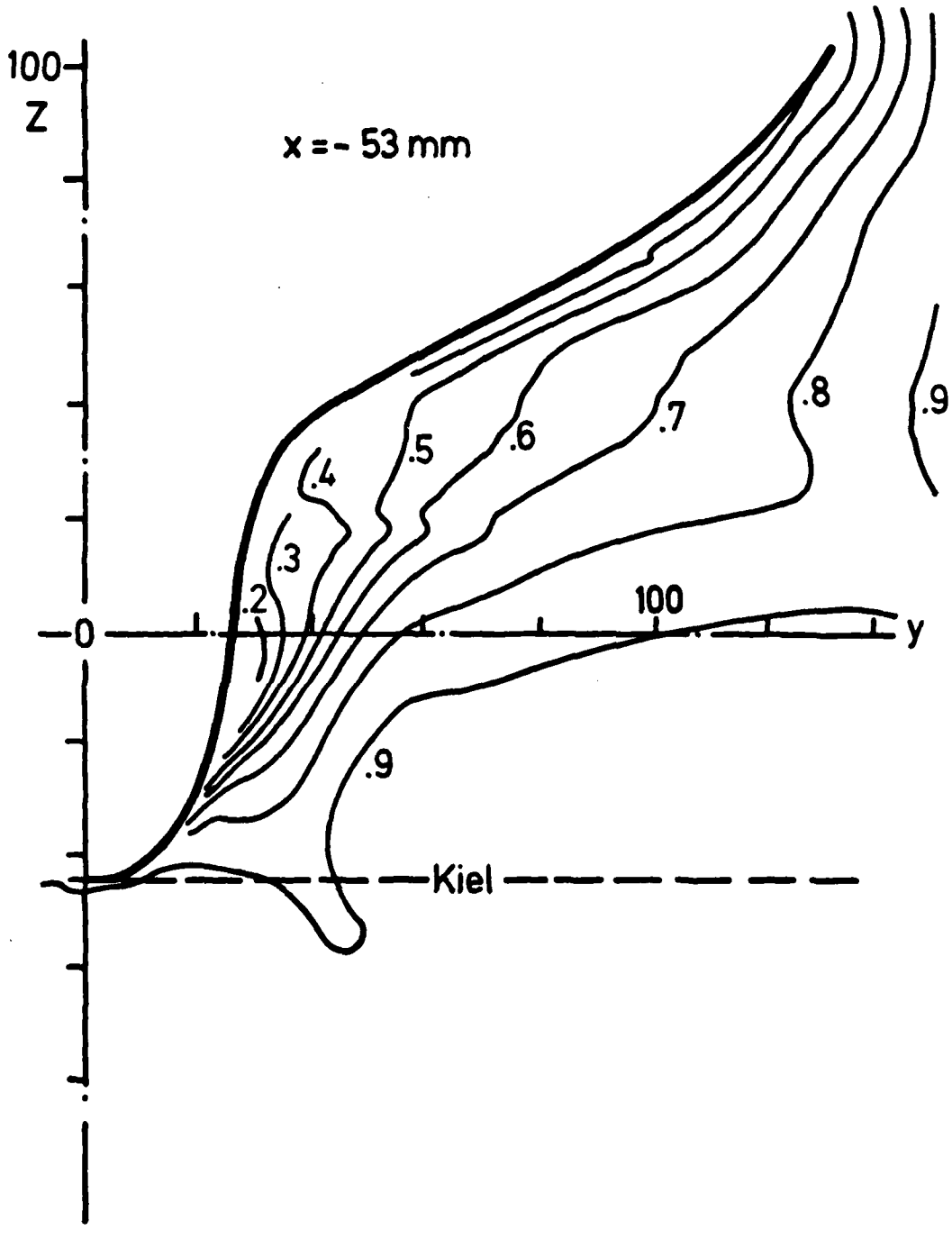

Figure 14 - Isotachs of Longitudinal Velocity u in Plane x = -53

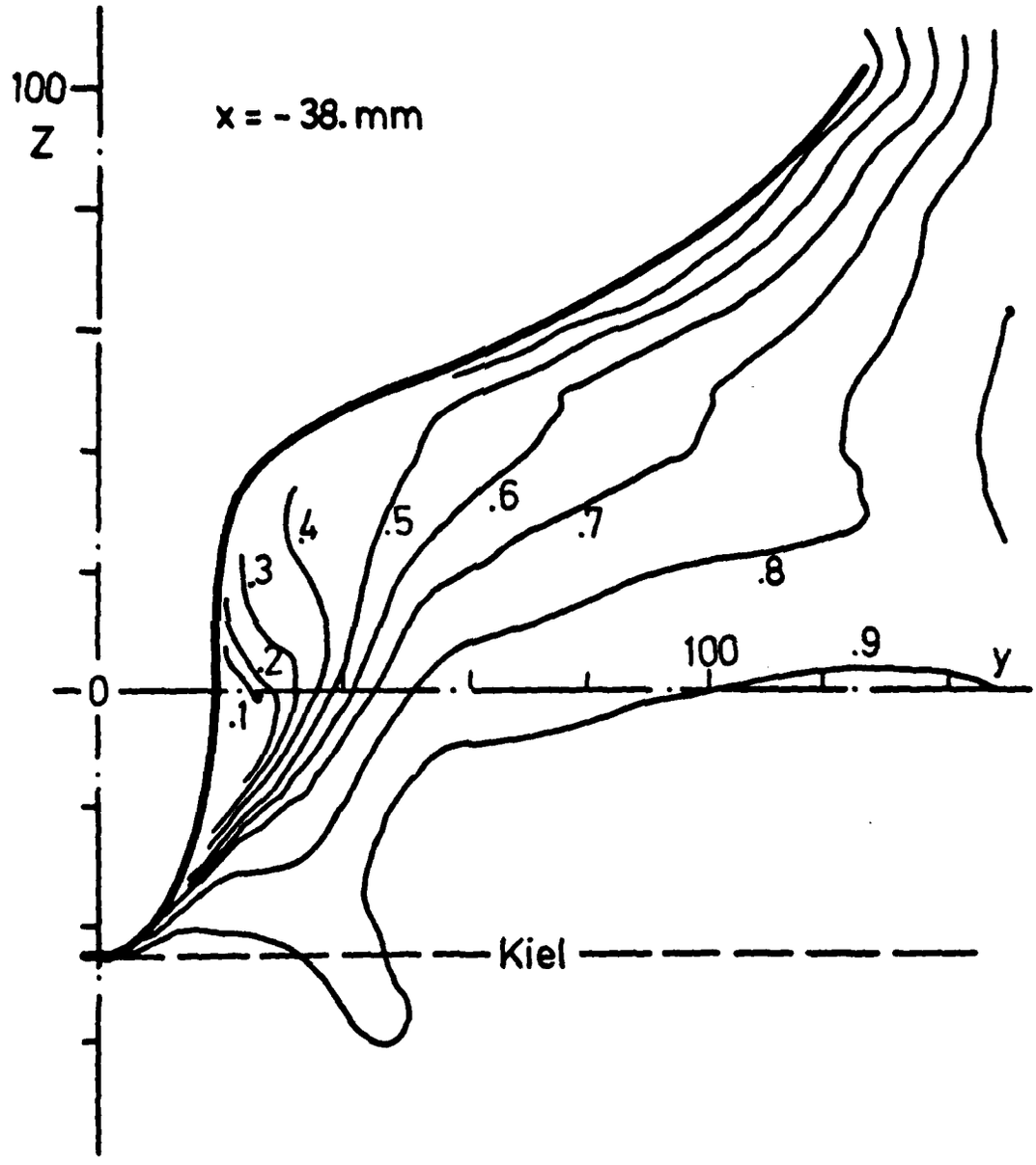

Figure 15 - Isotachs of Longitudinal Velocity u in Plane x = -38

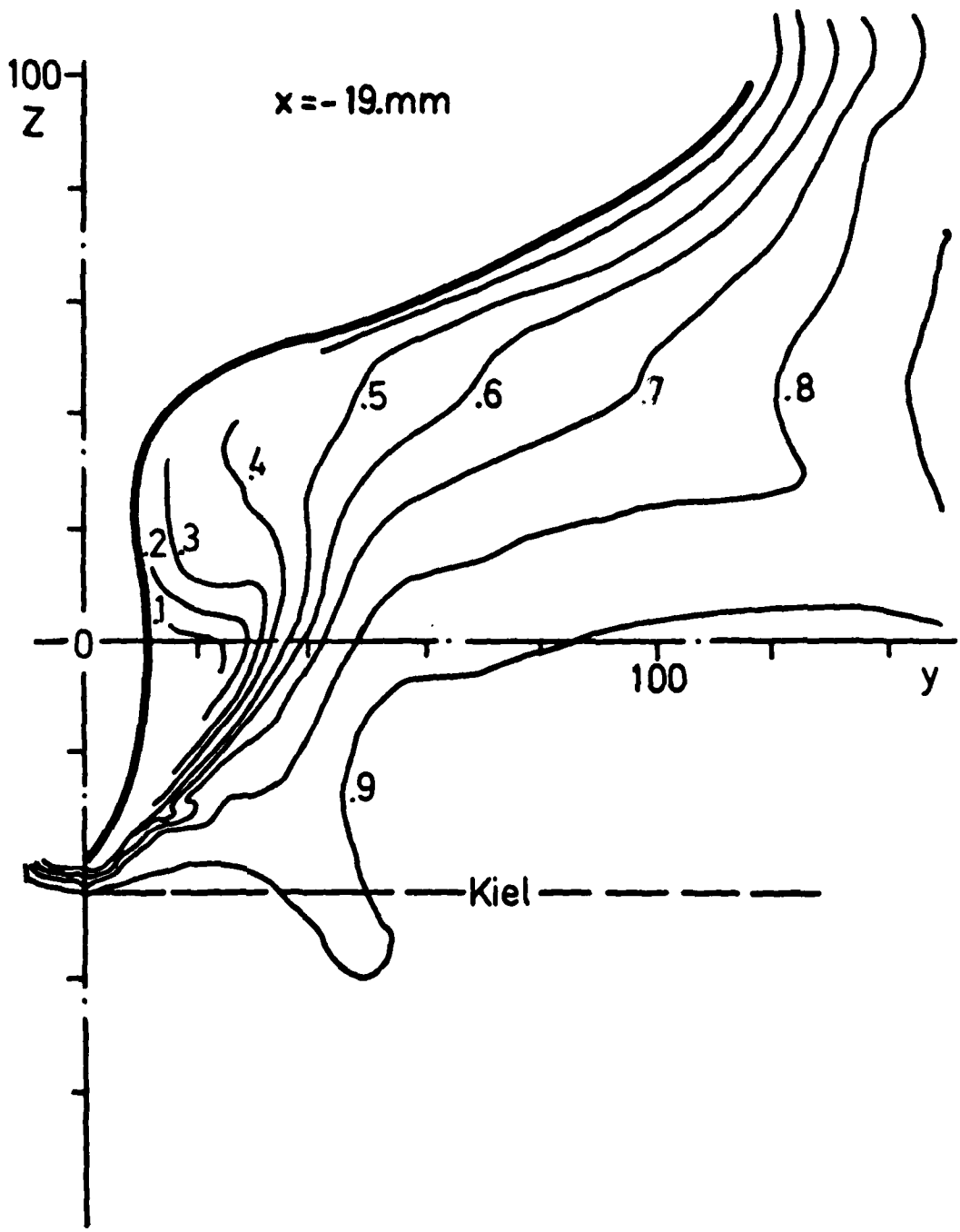

Figure 16 - Isotachs of Longitudinal Velocity u in Plane x = -19

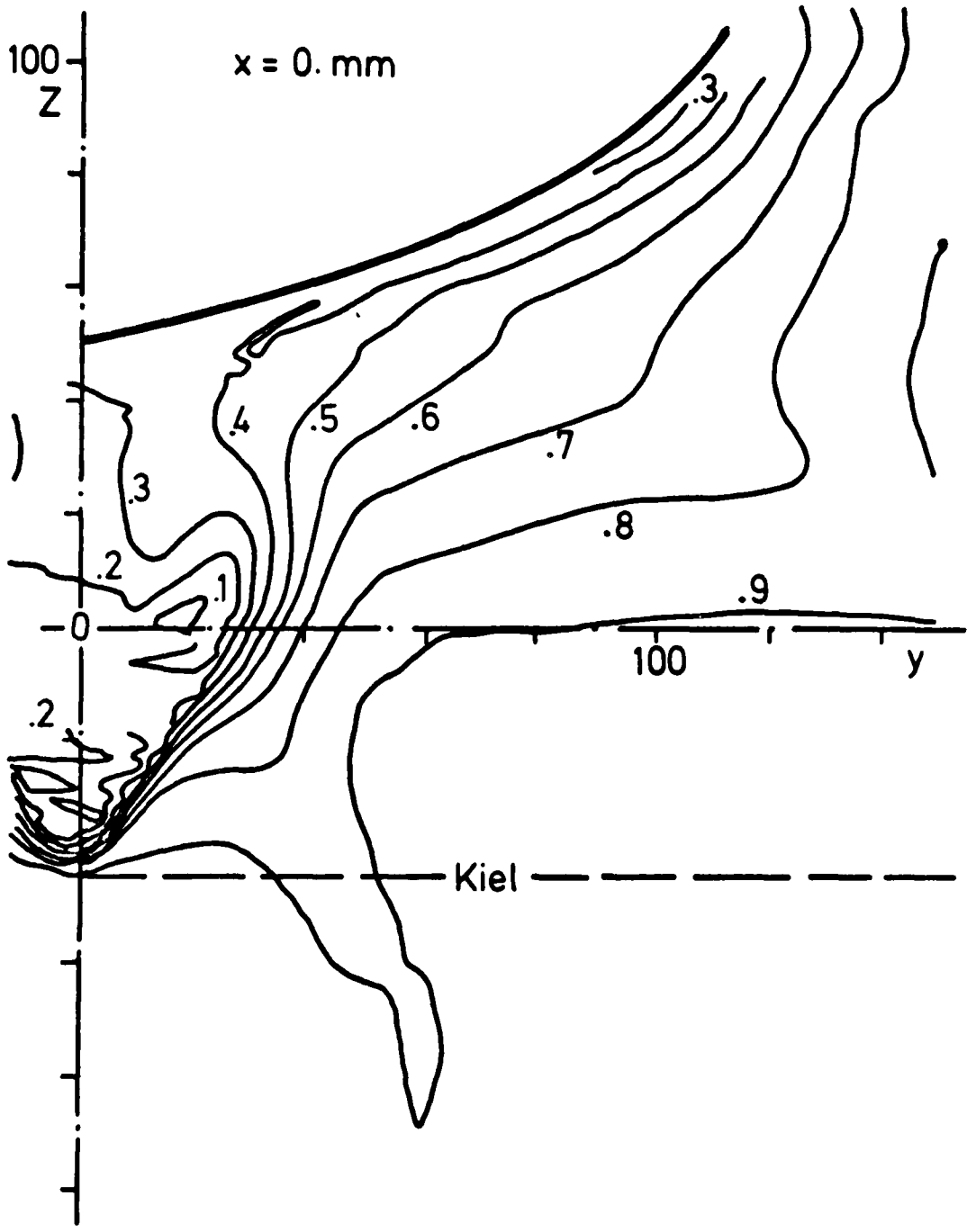

Figure 17 - Isotachs of Longitudinal Velocity u in Plane x = 0

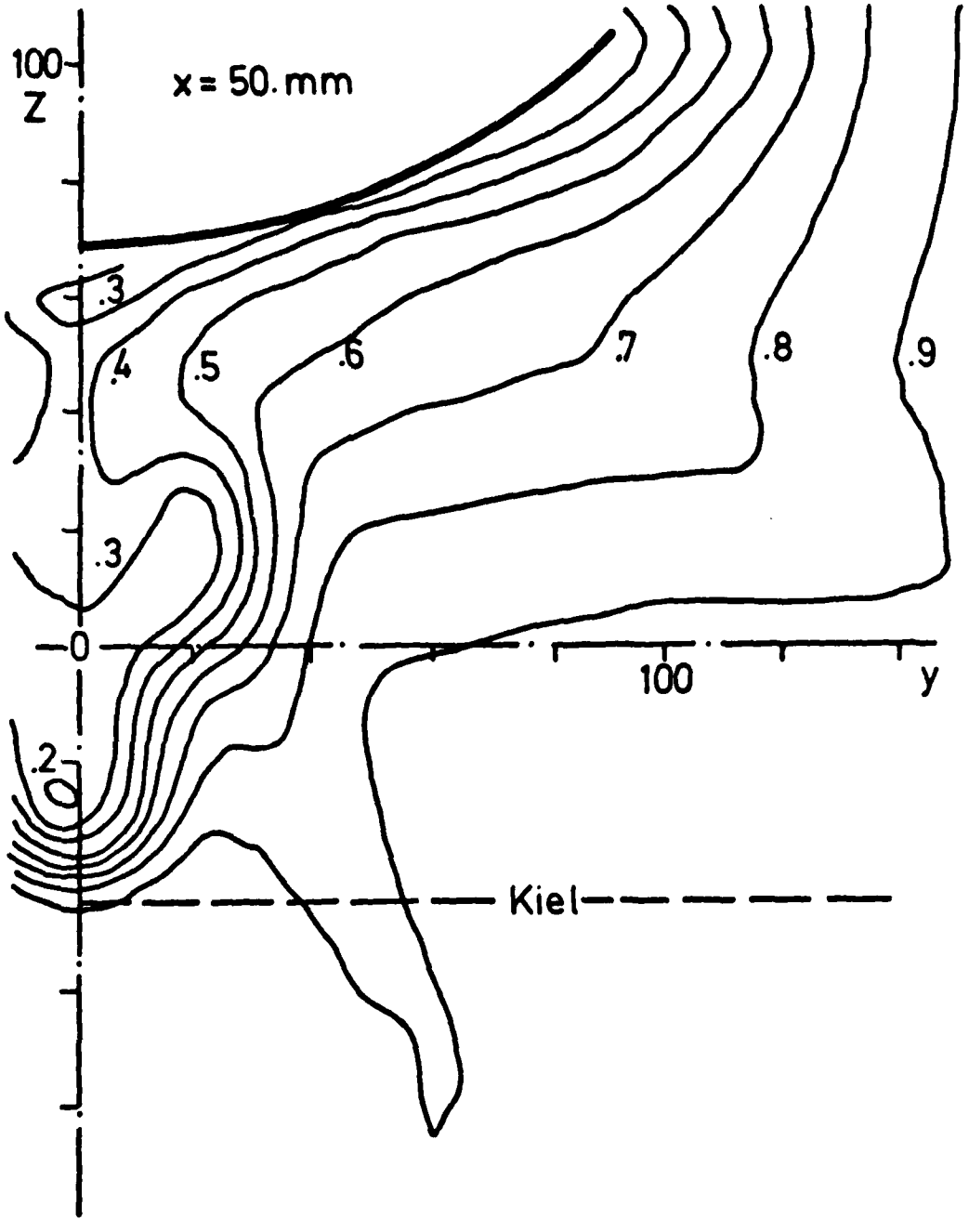

Figure 18 - Isotachs of Longitudinal Velocity u in Plane x = 50

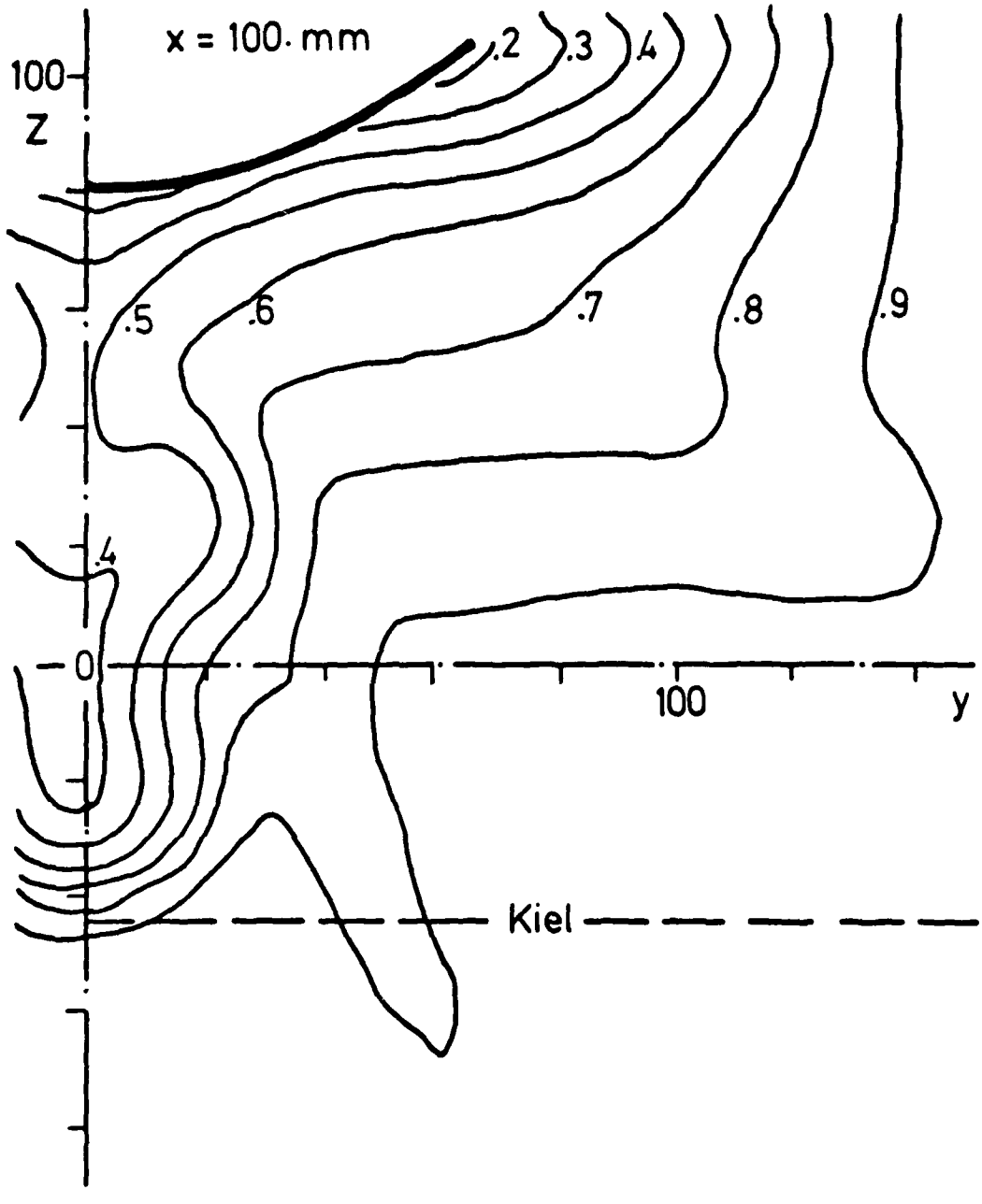

Figure 19 - Isotachs of Longitudinal Velocity u in Plane x = 100

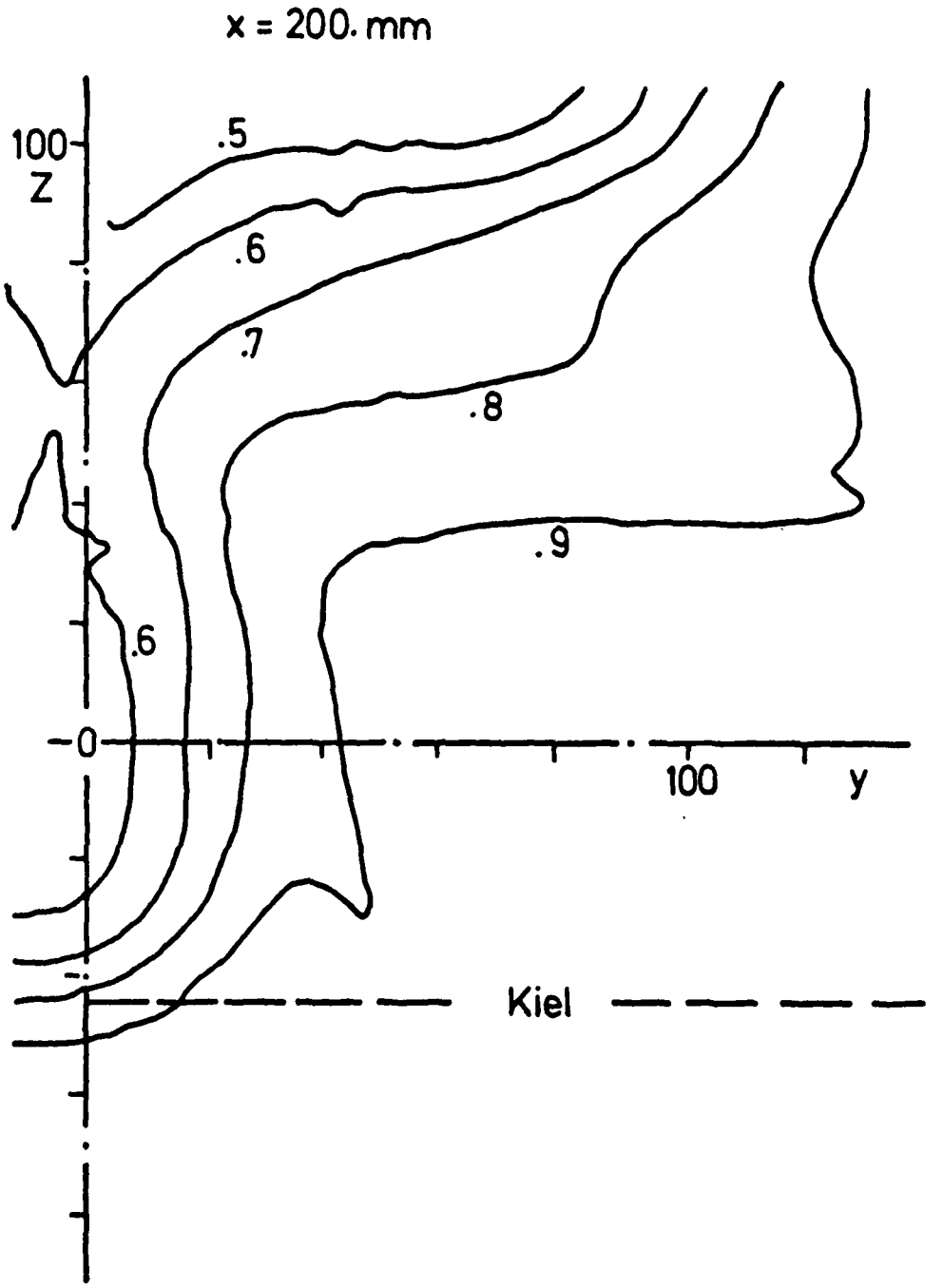

Figure 20 - Isotachs of Longitudinal Velocity u in Plane x = 200

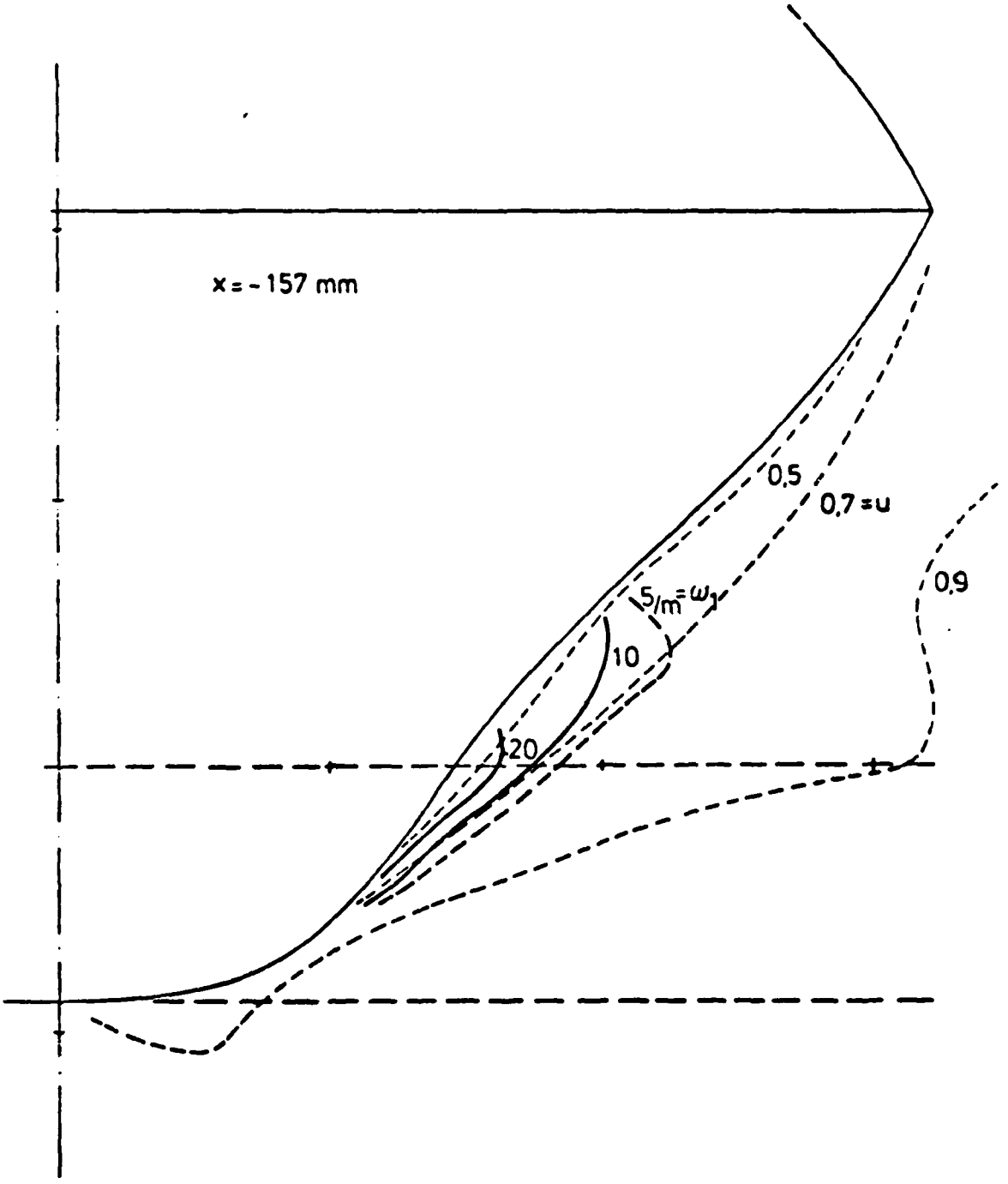

Figure 21 - Longitudinal Vorticity at x = -157

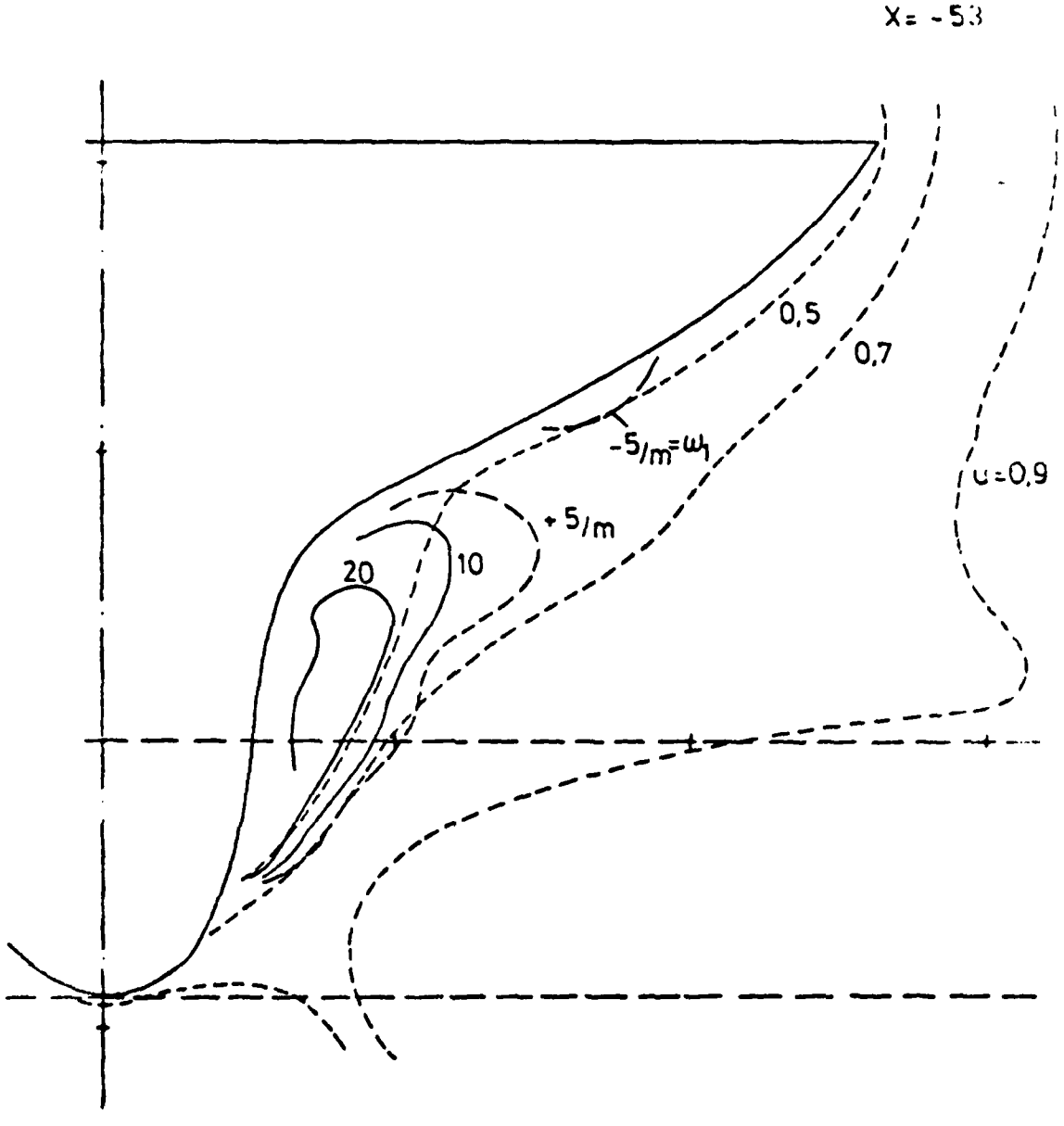

Figure 22 - Longitudinal Vorticity at x = -53

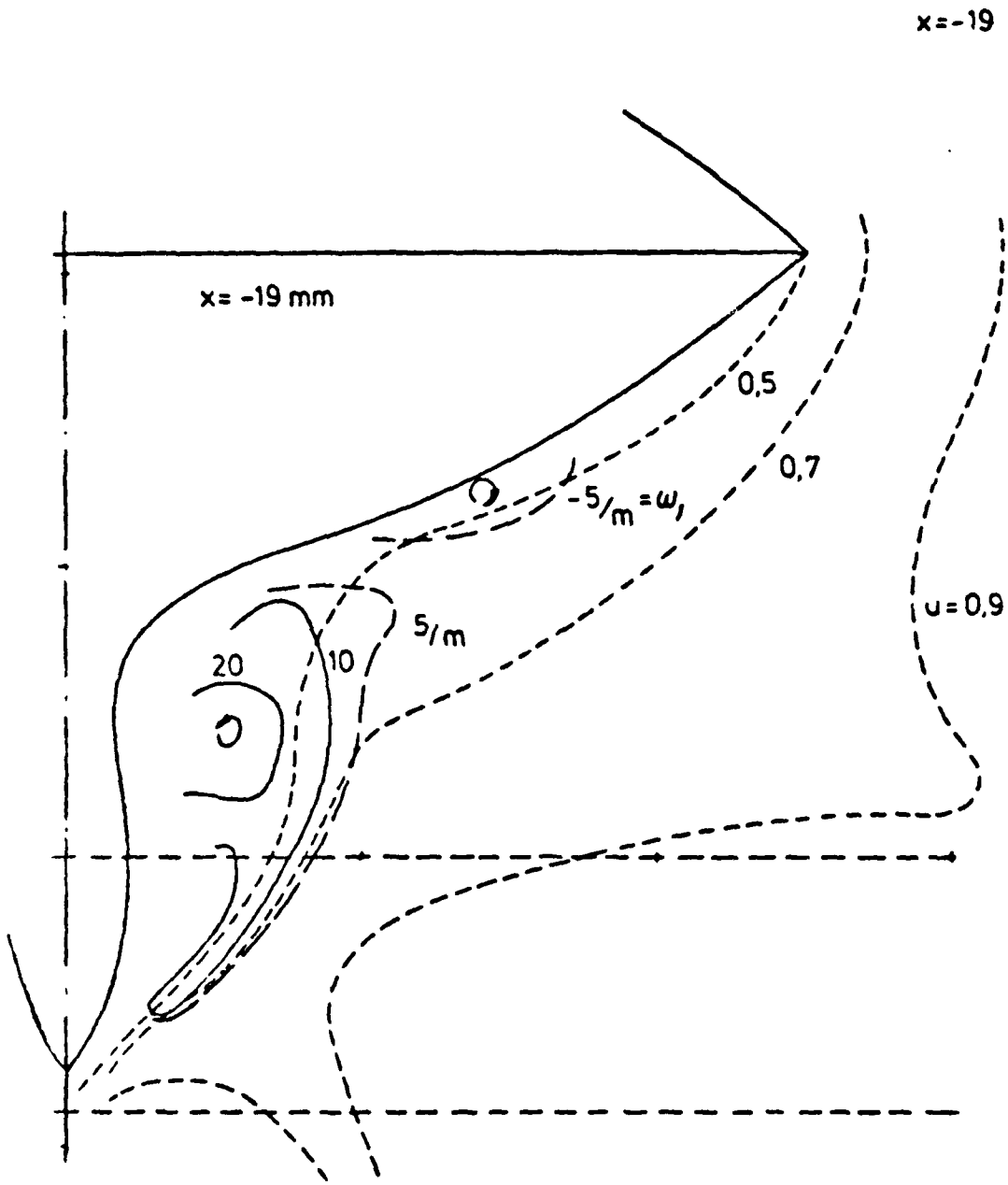

Figure 23 - Longitudinal Vorticity at x = -19

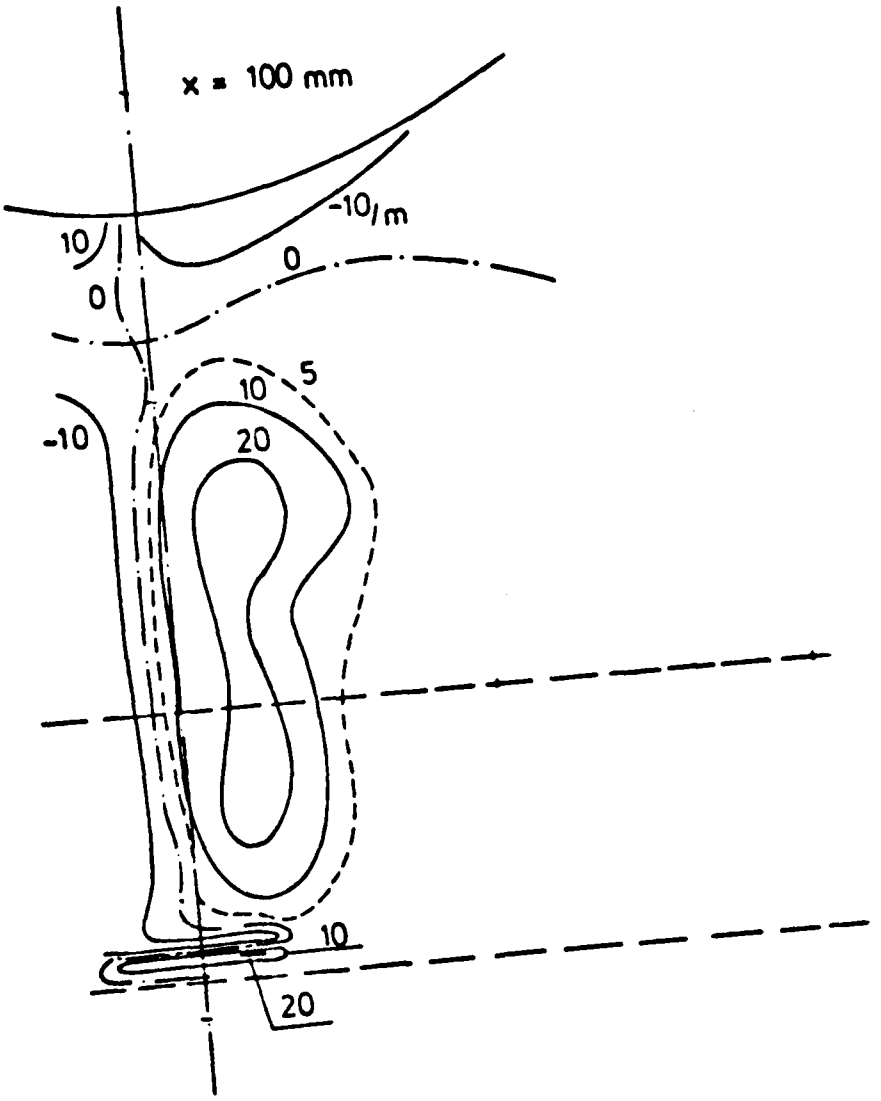

Figure 24 - Longitudinal Vorticity at x = 100

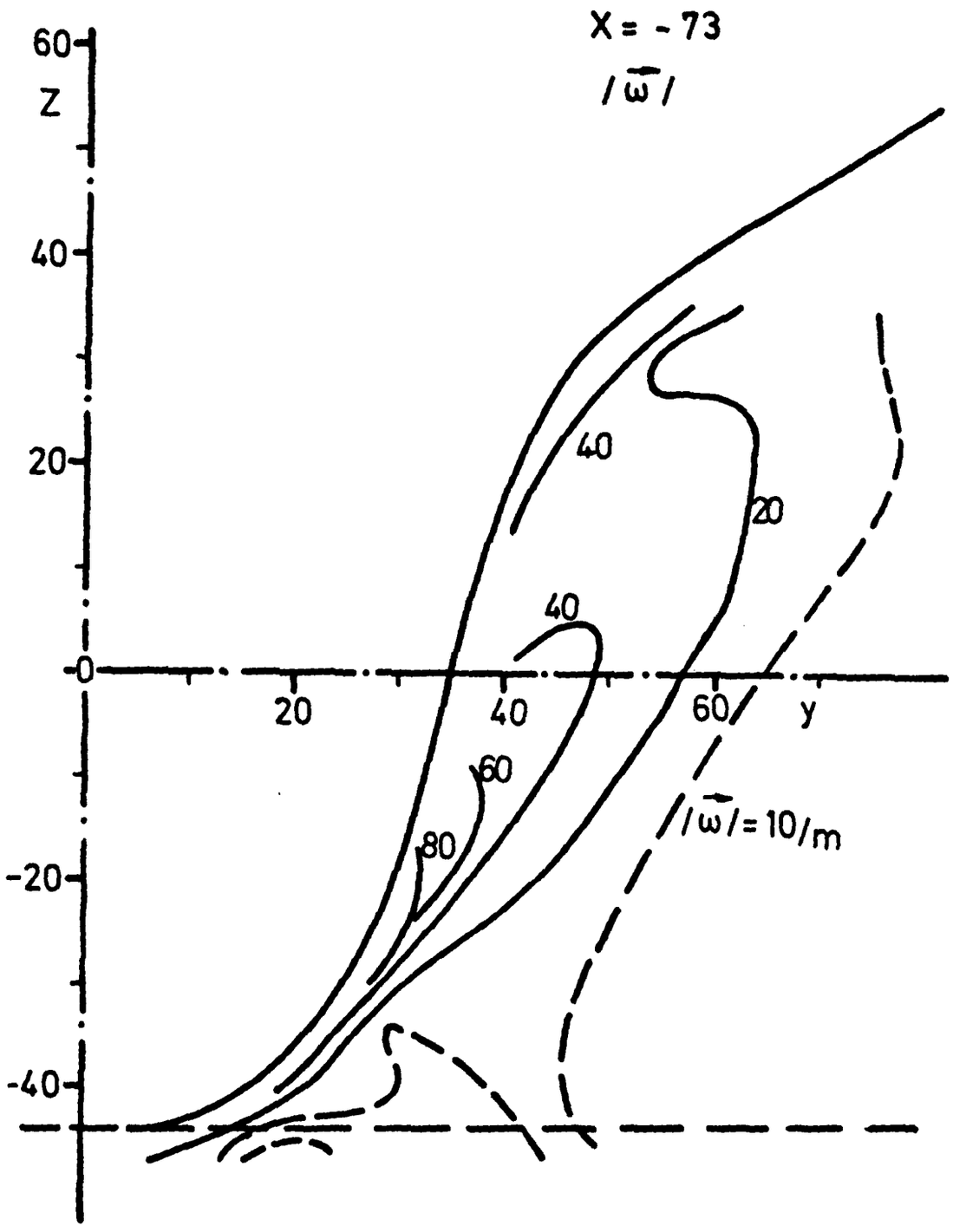

Figure 25 - Magnitude of Vorticity $/\vec{\omega}/$ at x = -73

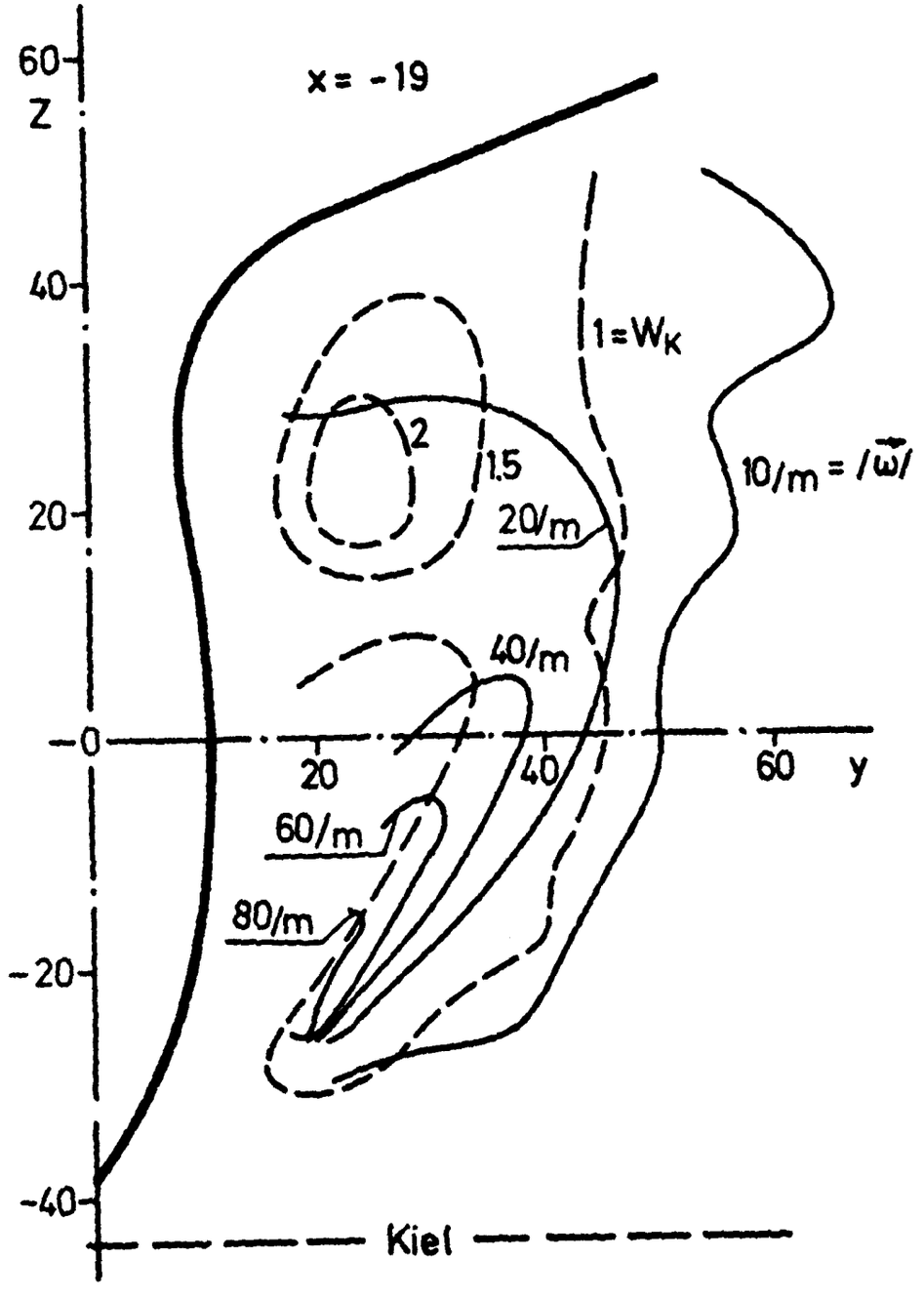

Figure 26 - Magnitude of Vorticity $/\vec{\omega}/$ and W_K at x = -19

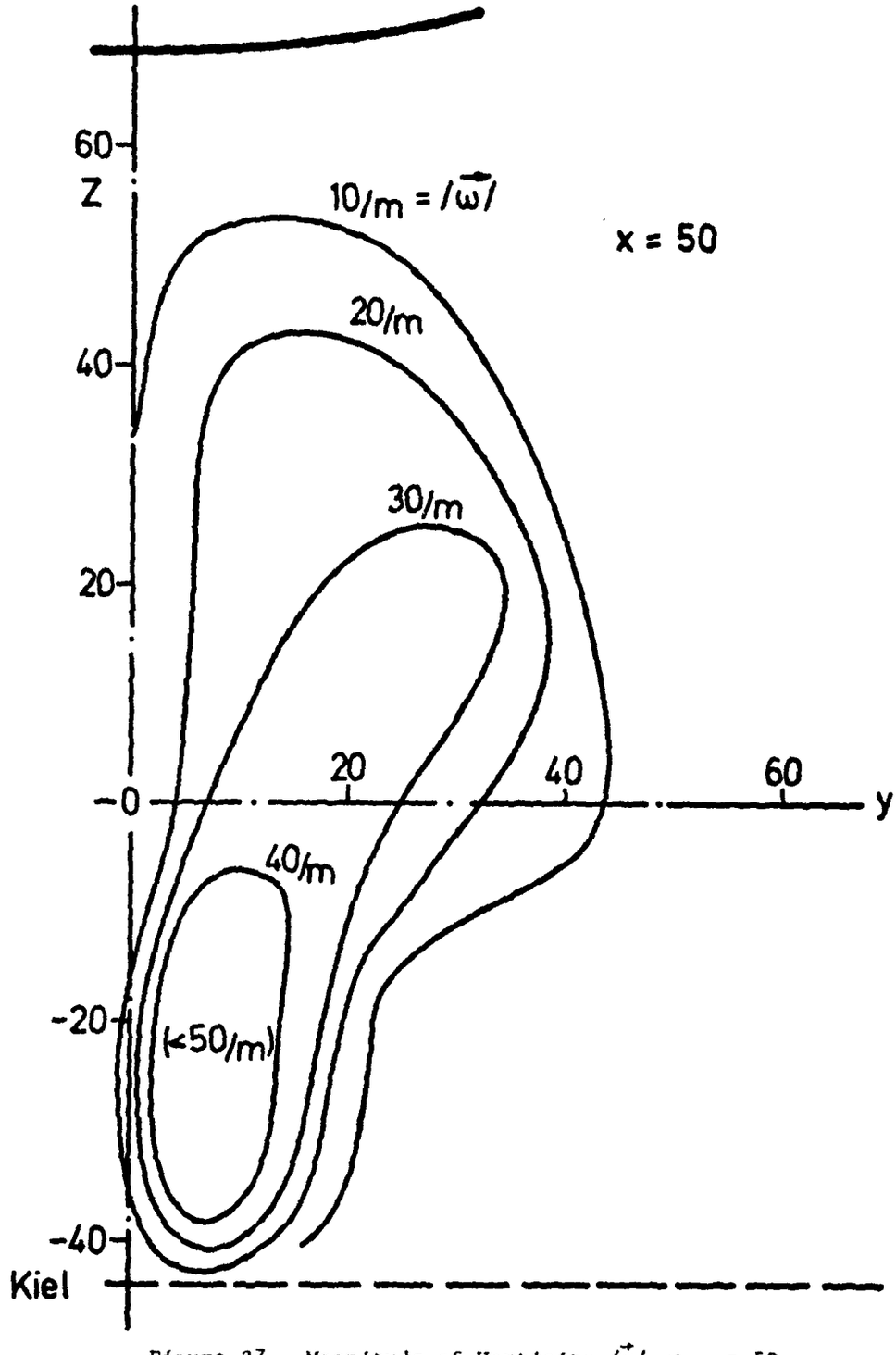

Figure 27 - Magnitude of Vorticity $/\vec{\omega}/$ at x = 50

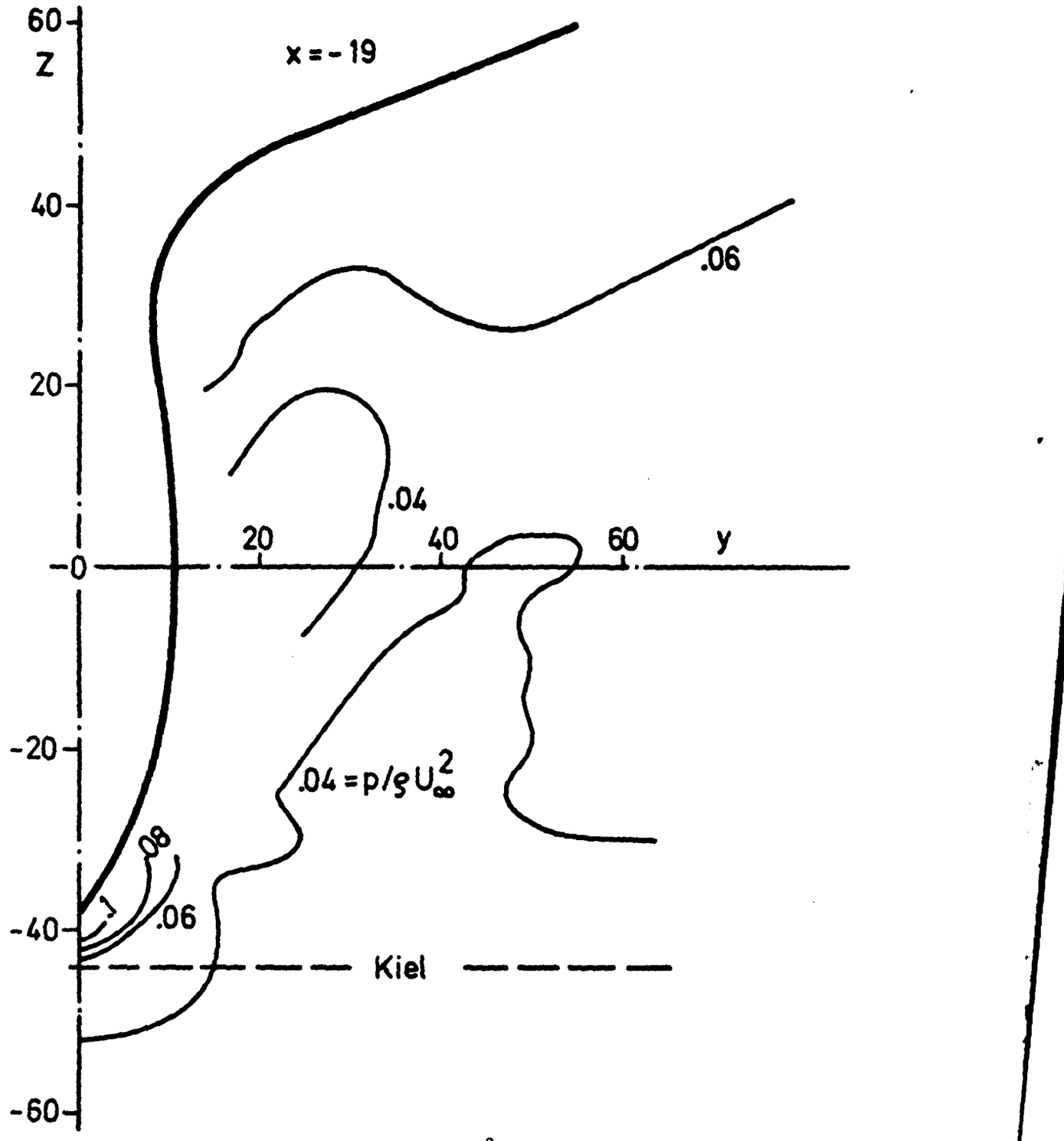

Figure 28 - Isobars $p/\rho\ U_\infty^2$ at x = -19

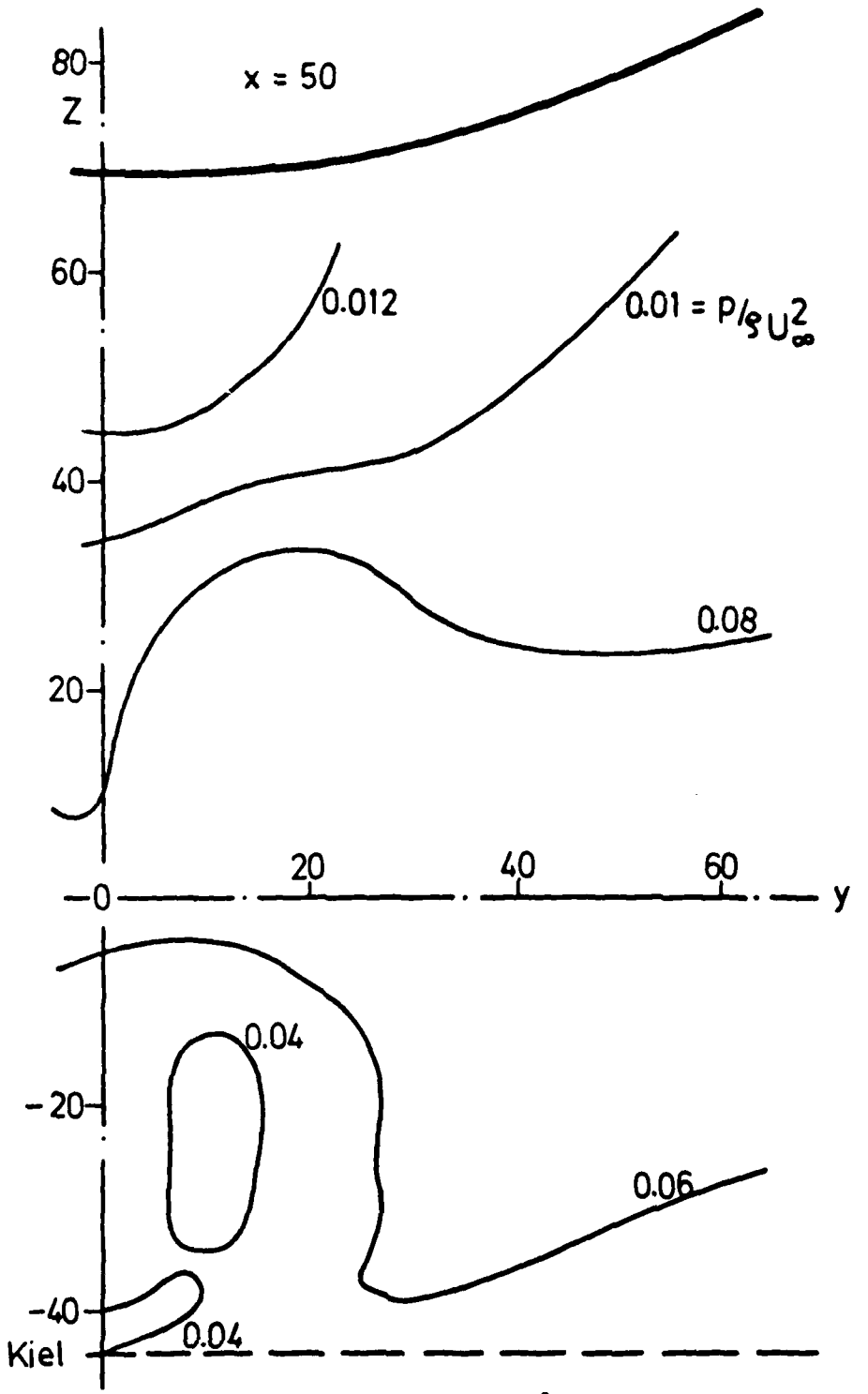

Figure 29 - Isobars $p/\rho\ U_\infty^2$ at x = 50

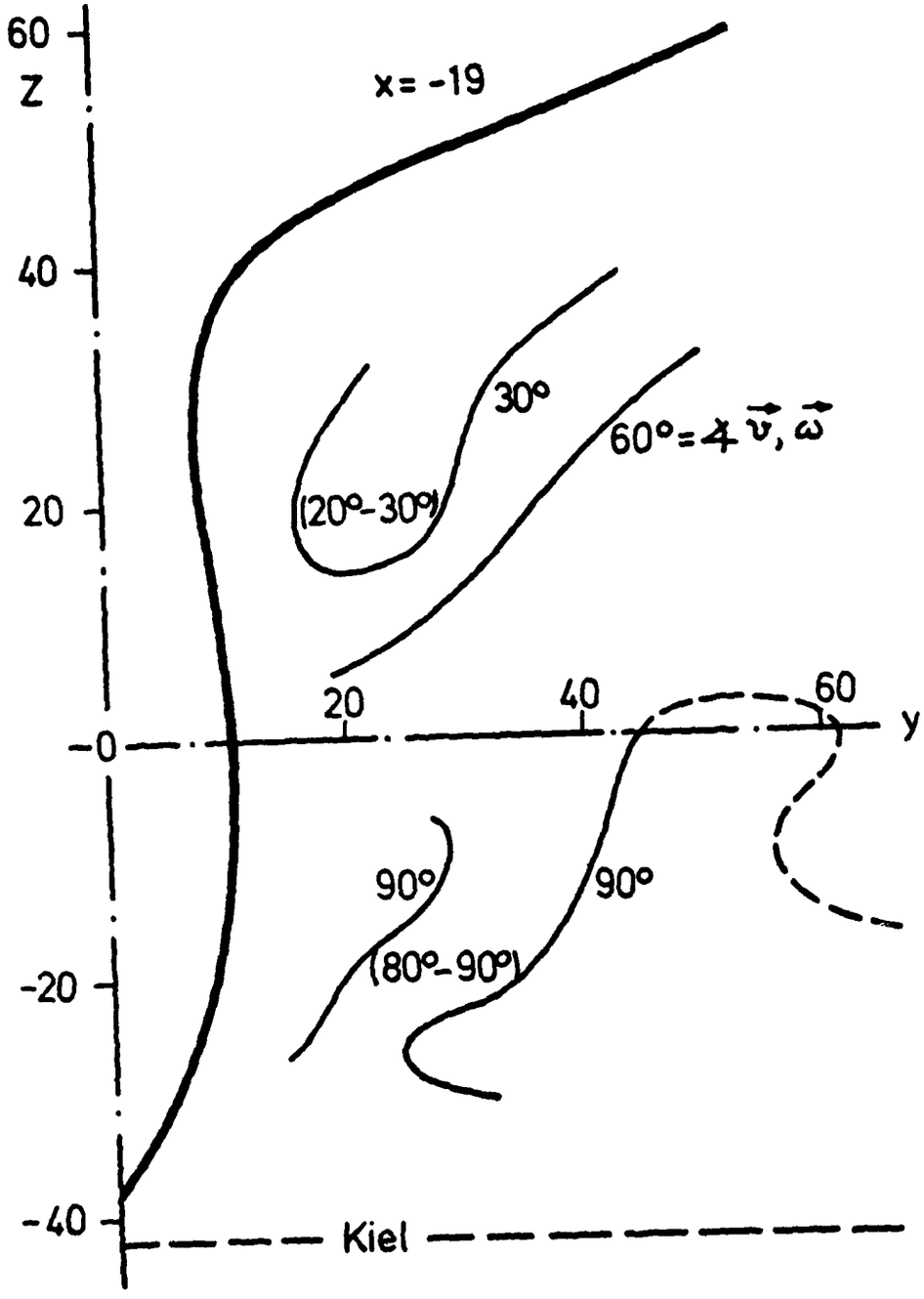

Figure 30 - Lines for Constant Angle between Velocity and Vorticity at x = -19

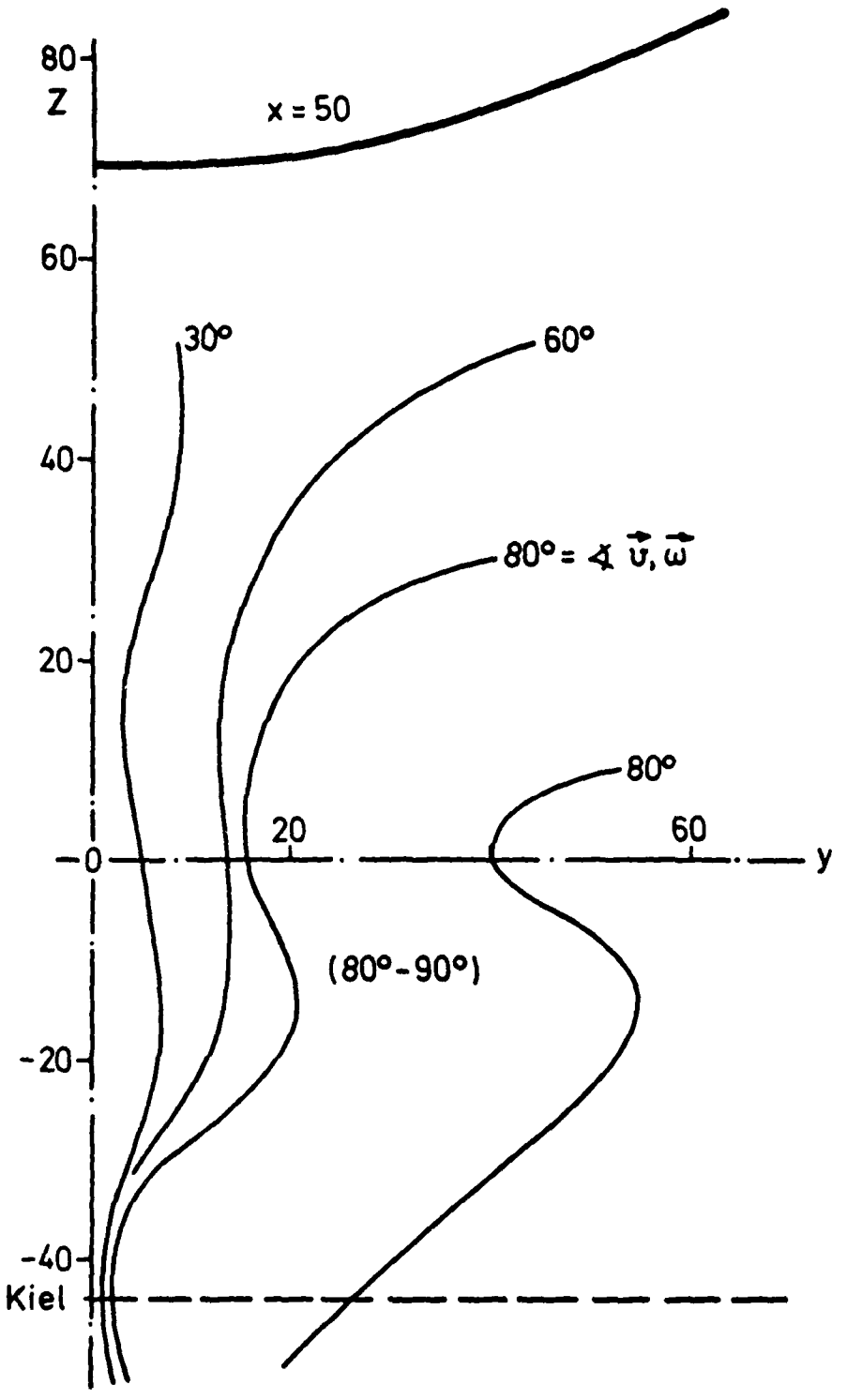

Figure 31 - Lines for Constant Angle between Velocity and Vorticity at x = 50

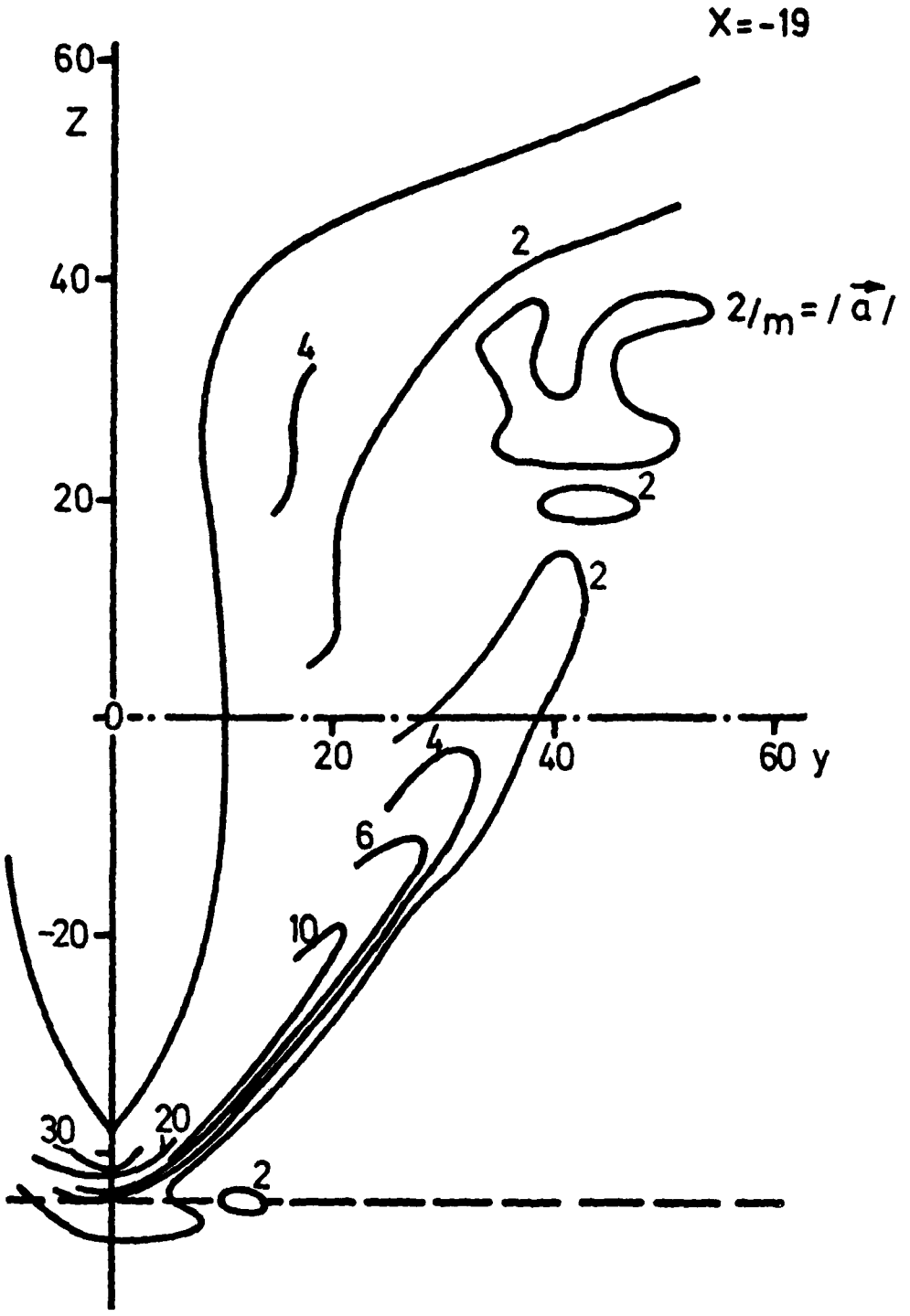

Figure 32 - Magnitude of Acceleration $/\vec{a}/$ (Divided by U_∞) at x = -19

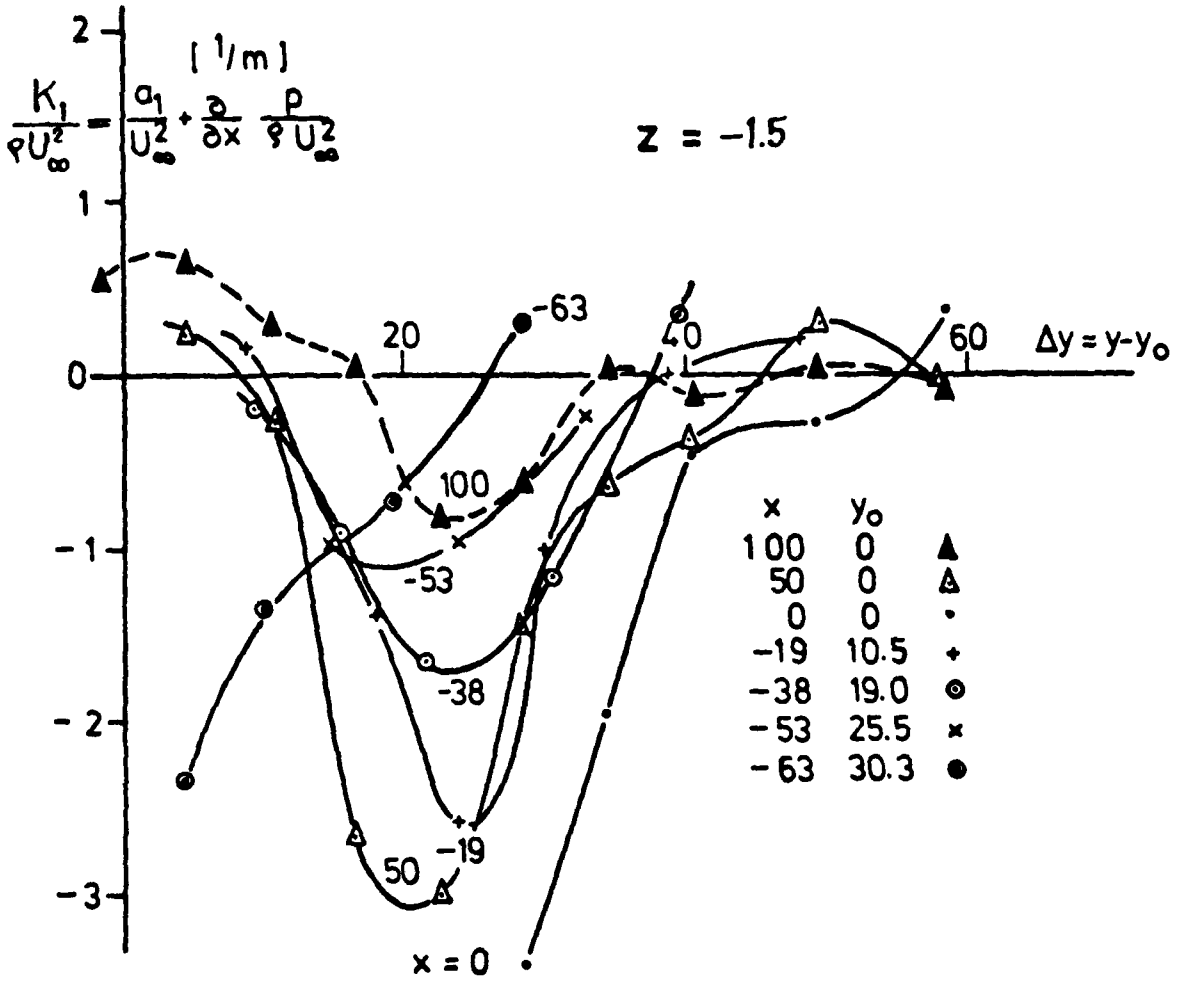

Figure 33 - Longitudinal Force by Reynolds Stresses $K_1/\rho\ U_\infty^2$ vs Horizontal Wall Distance Δy at z = -1.5 in Various Test Planes

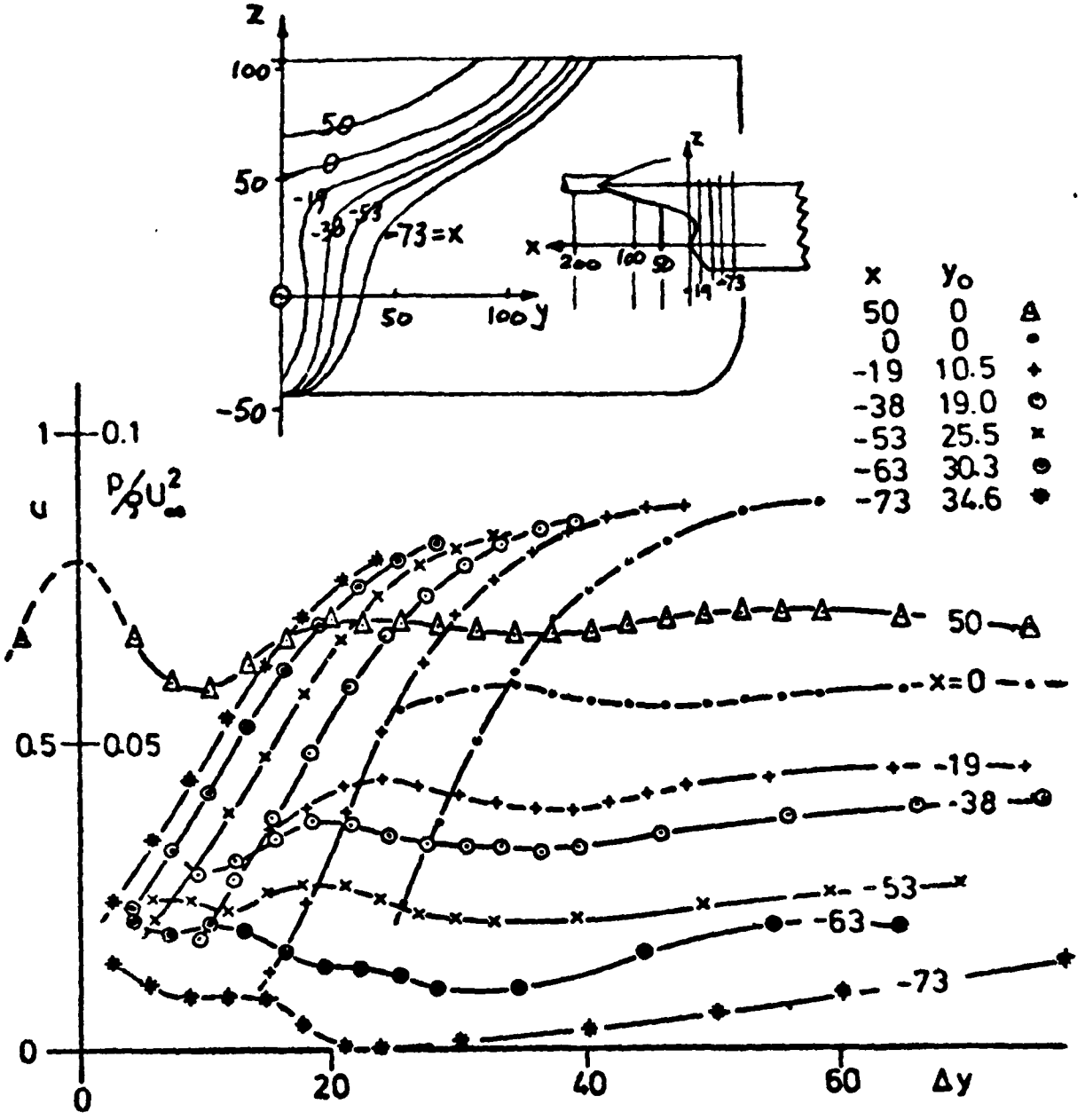

Figure 34 - Profiles of Longitudinal Velocity u and of Static Pressure $p/\rho\ U_\infty^2$ vs Horizontal Wall Distance Δy at $z = -1.5$ in Various Test Planes

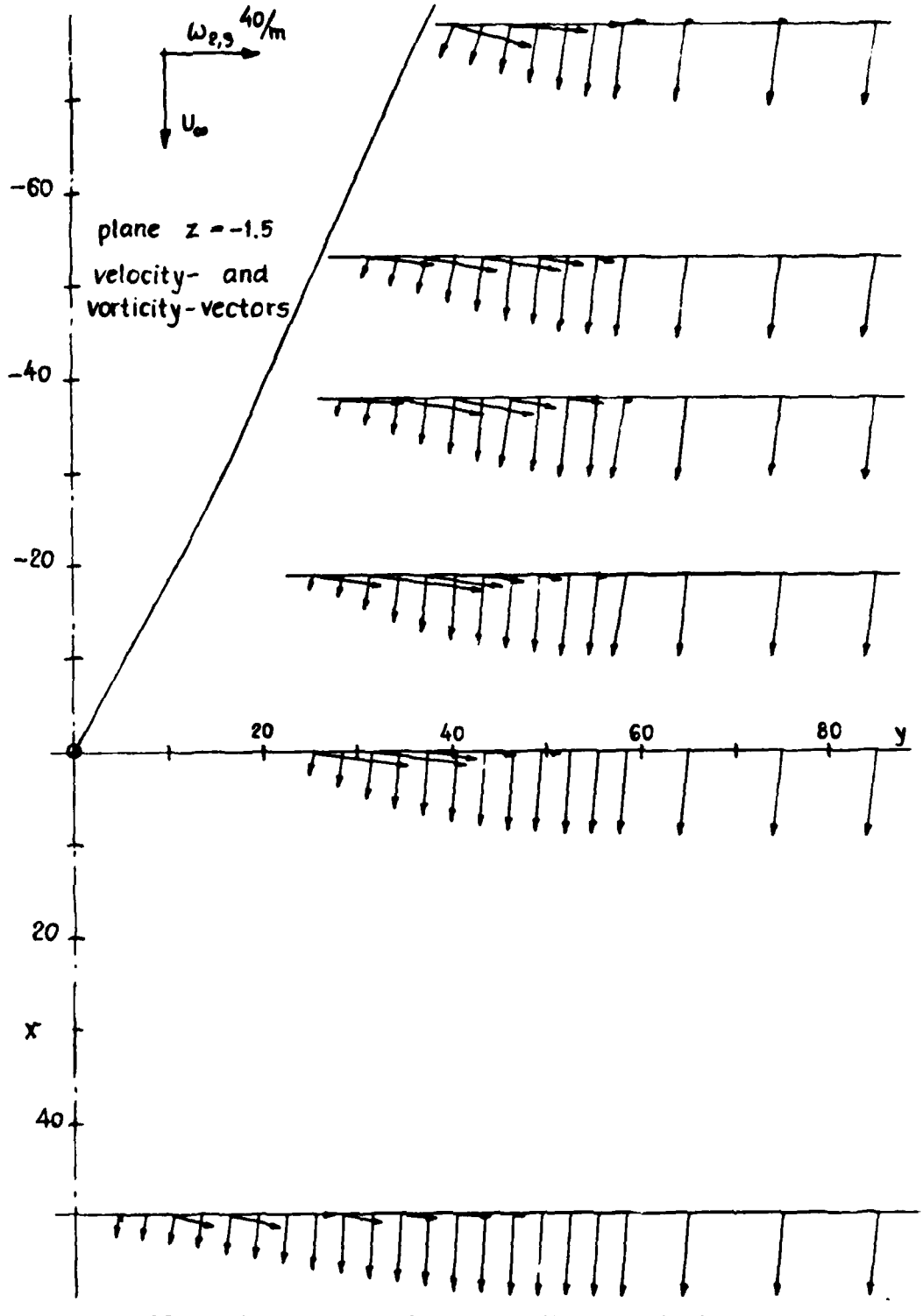

Figure 35 - Velocities u and v in the Horizontal Plane z = -1.5 at Various Stations x

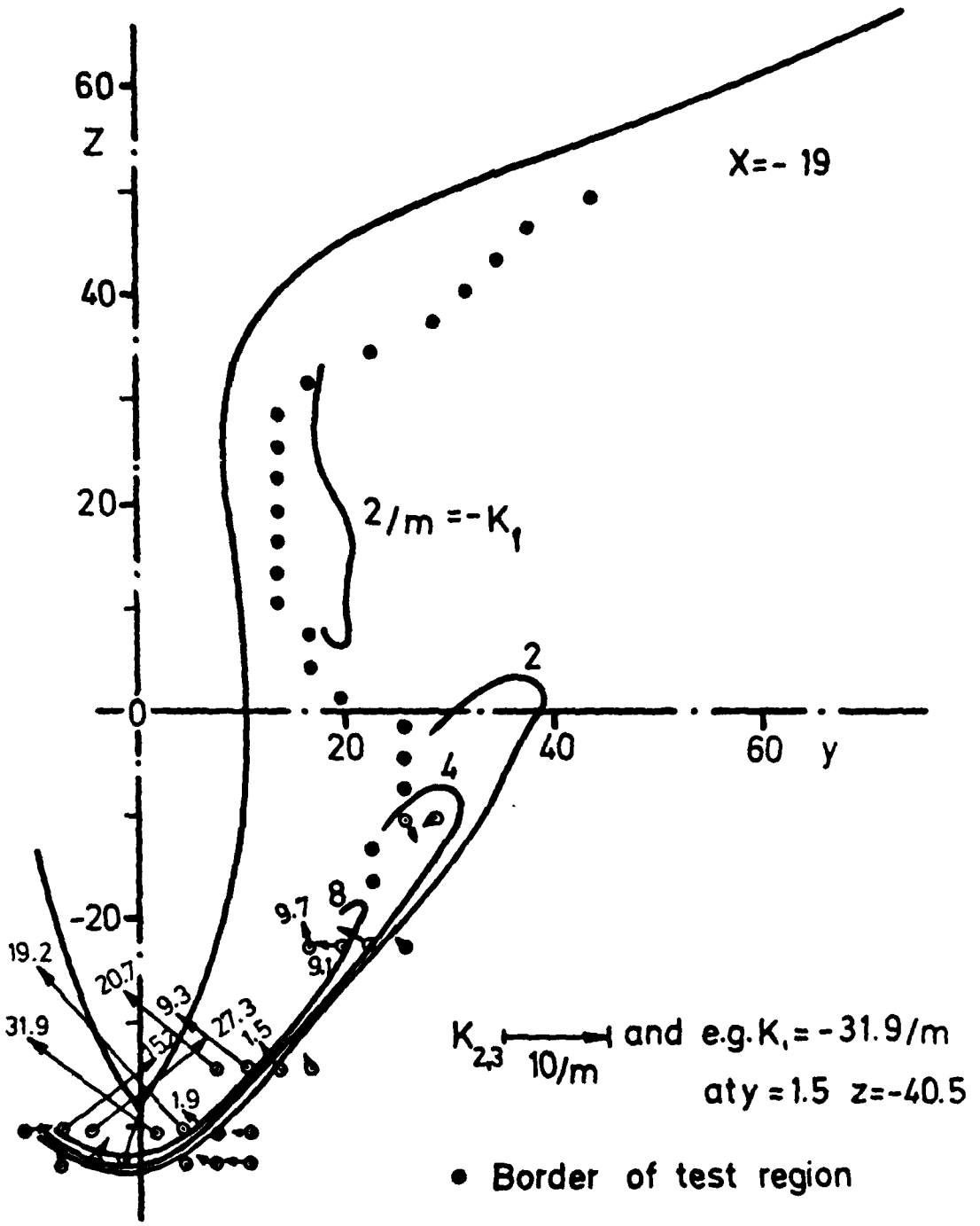

Figure 36 - Force Components K Resulting from Reynolds Stresses: Lines for K_1 - const and Arrows for Cross Component $\sqrt{K_2^2 + K_3^2}$ in the Vertical Plane z = -1.5 at x = -19

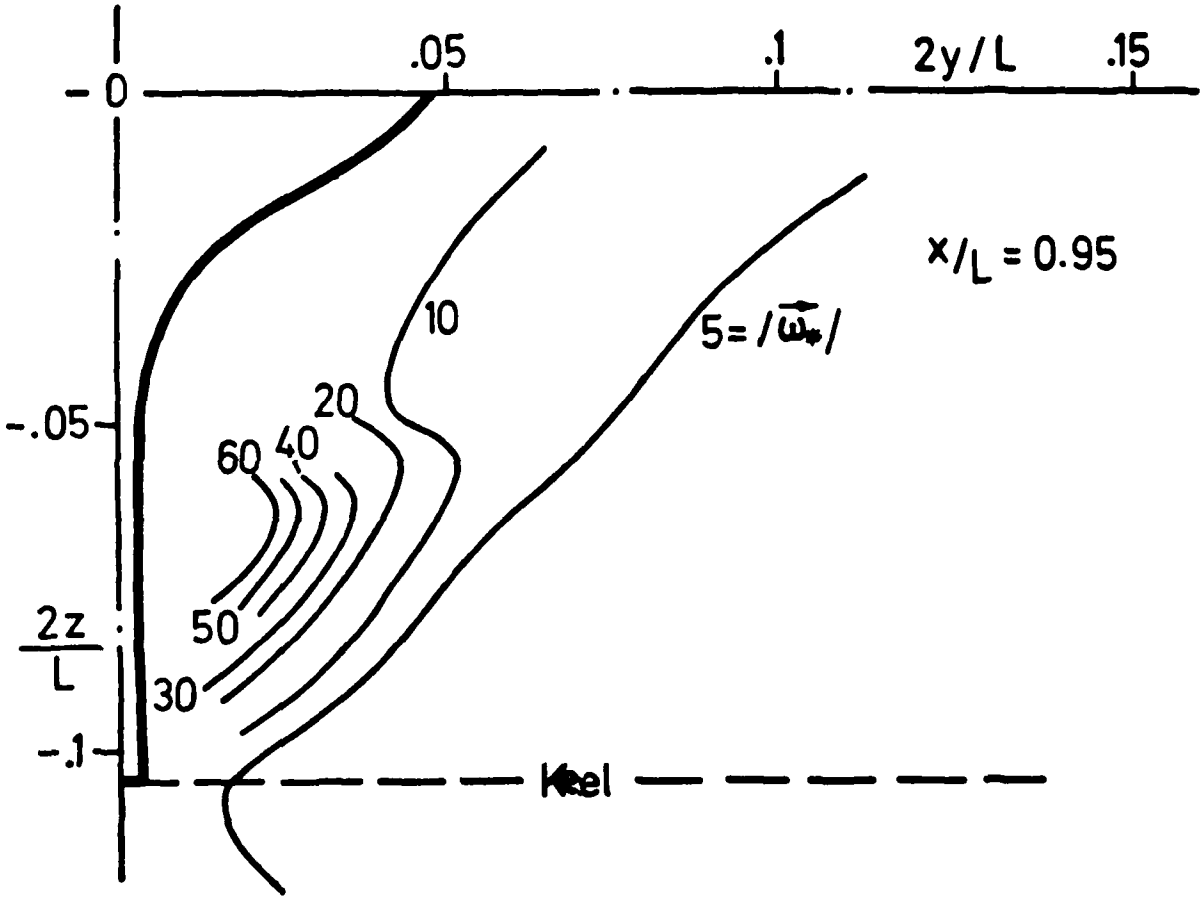

Figure 37 - Magnitude of Vorticity $|\vec{\omega}_*| = |\vec{\omega}|\frac{L}{2}/U_\infty^2$ at x/L = 0.95 after [2]

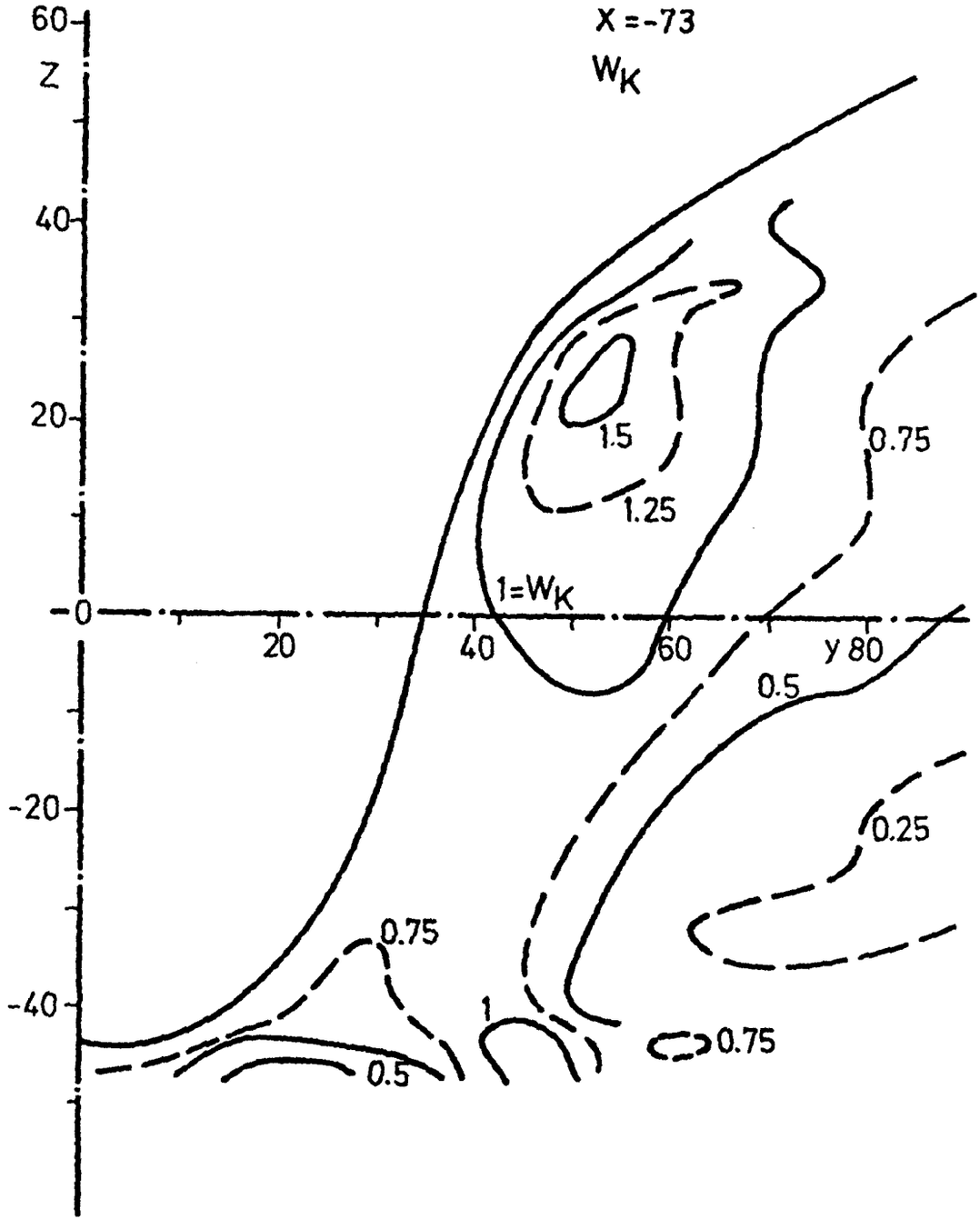

Figure 38 - Kinematic Vorticity Number W_K at x = -73

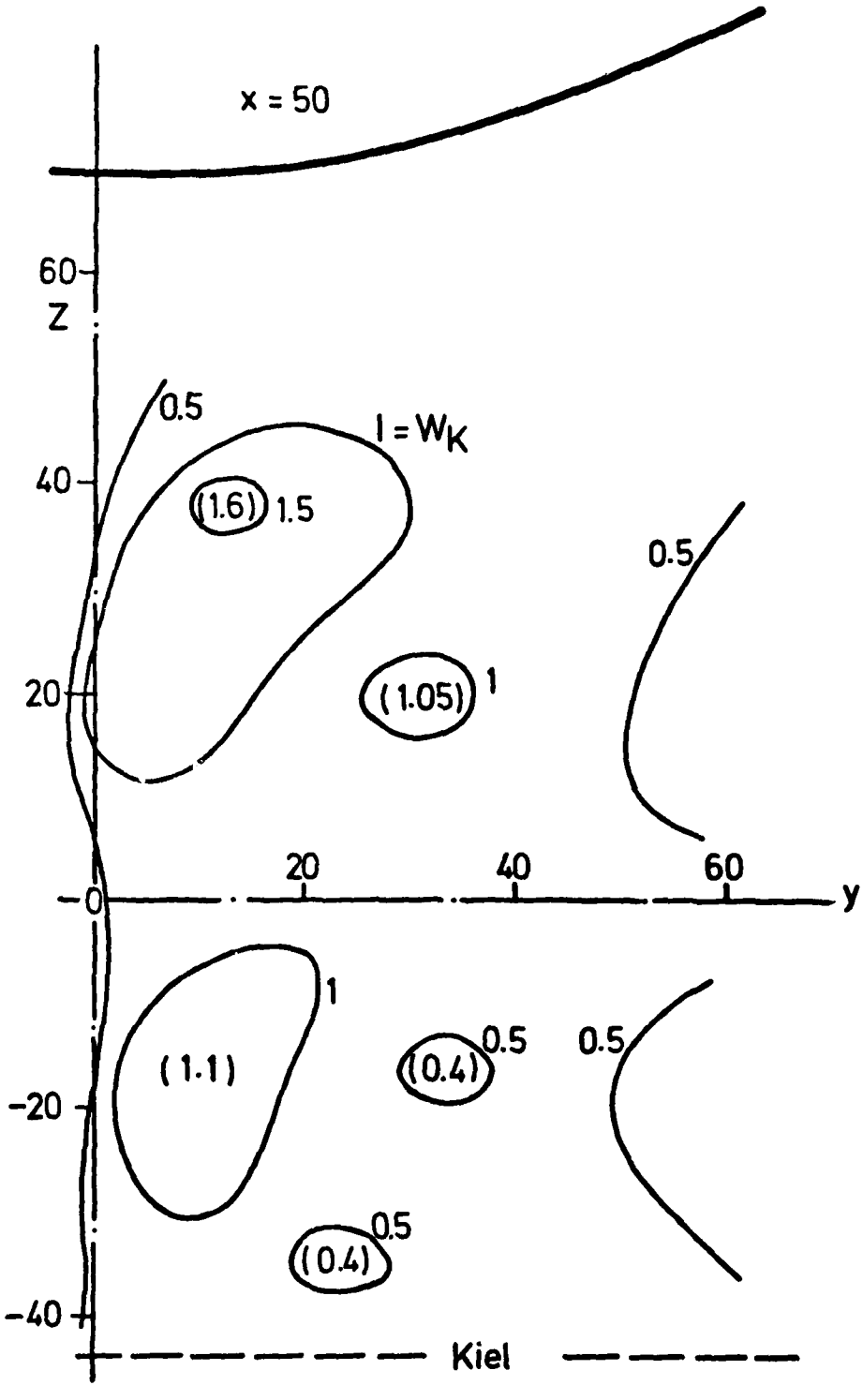

Figure 39 - Kinematic Vorticity Number W_K at x = 50

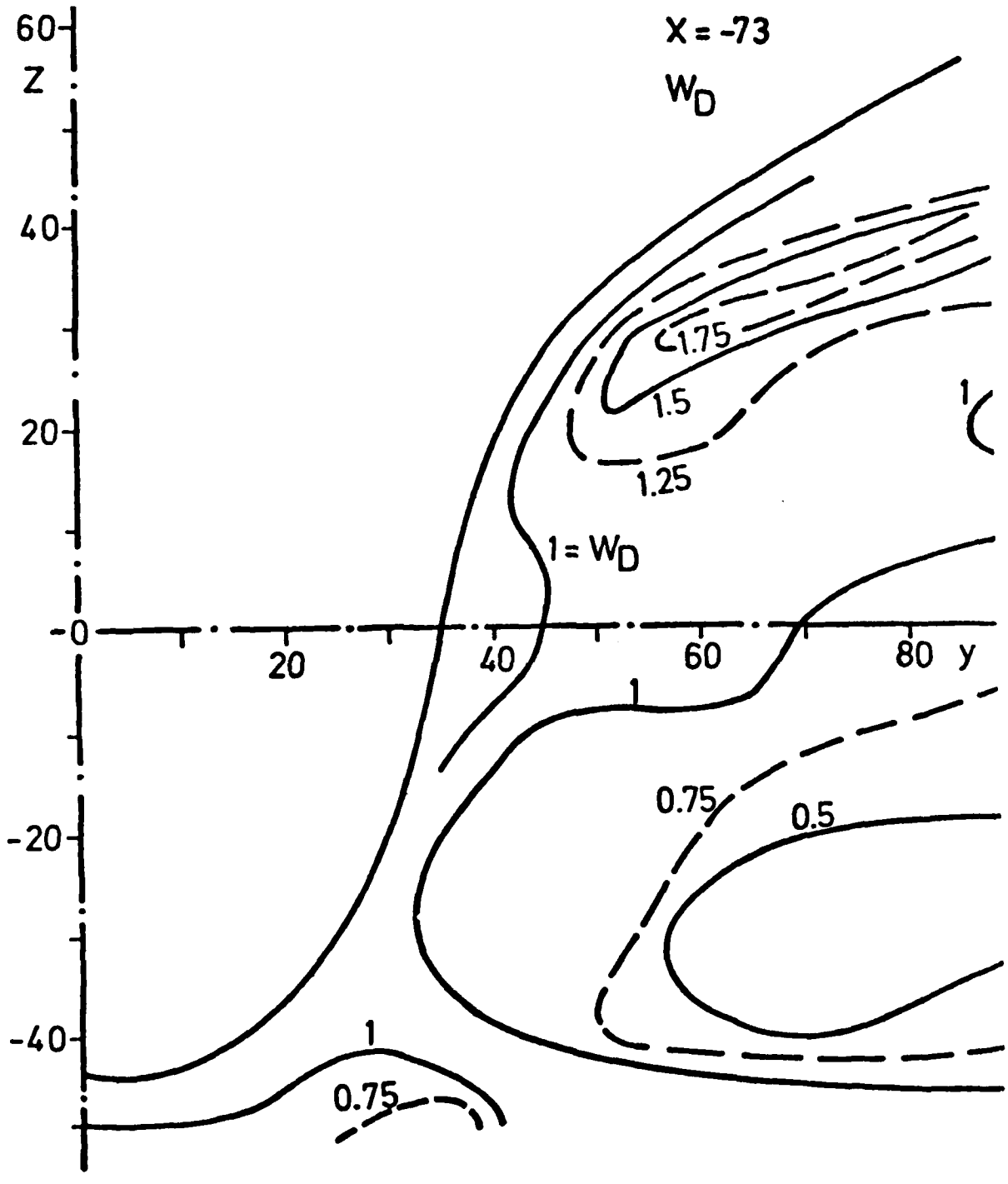

Figure 40 - Dynamical Vorticity Number W_D at x = -73

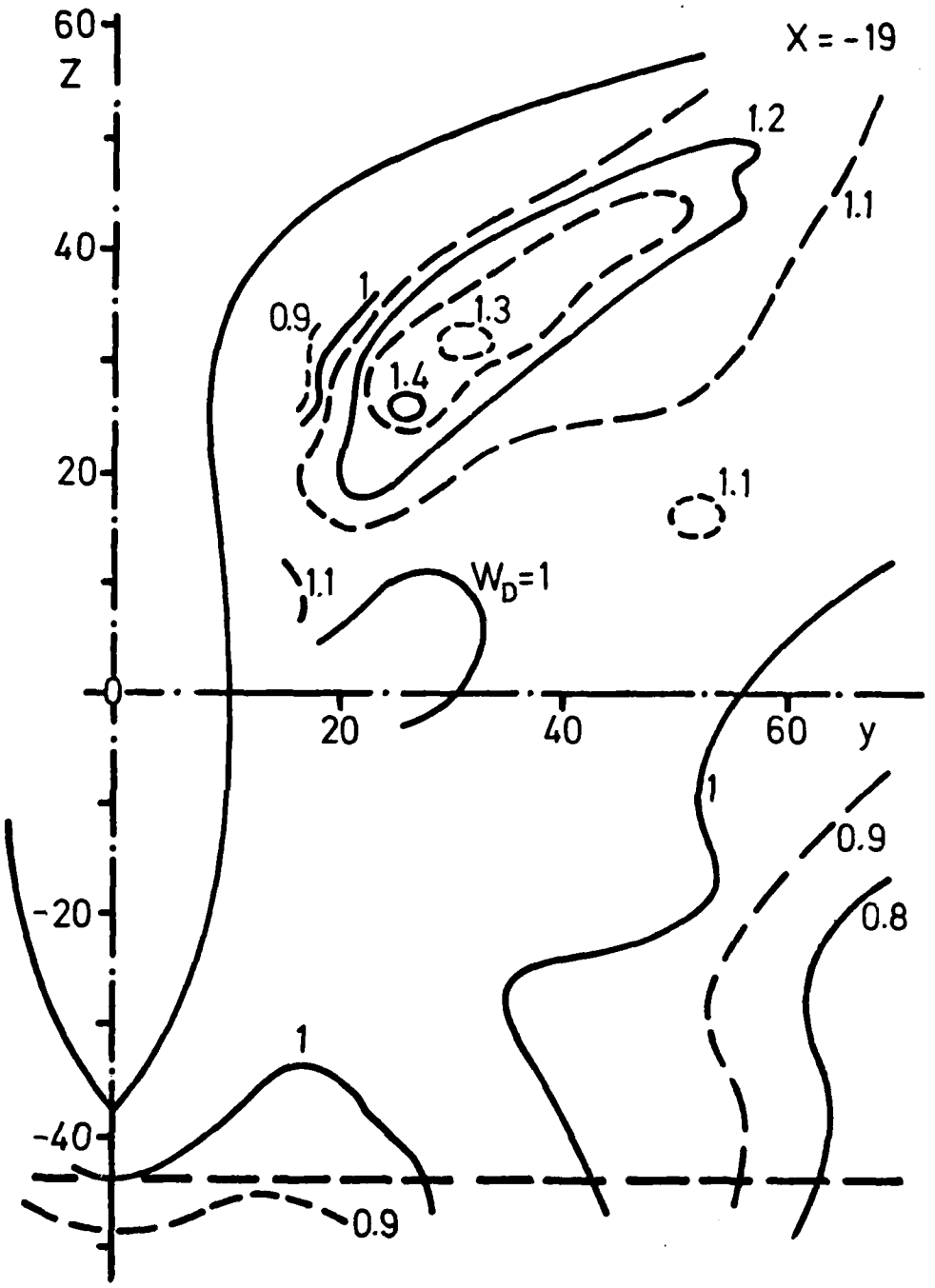

(Large scatter for $W_D \leq 1$ at right edge)

Figure 41 - Dynamical Vorticity Number W_D at x = -19

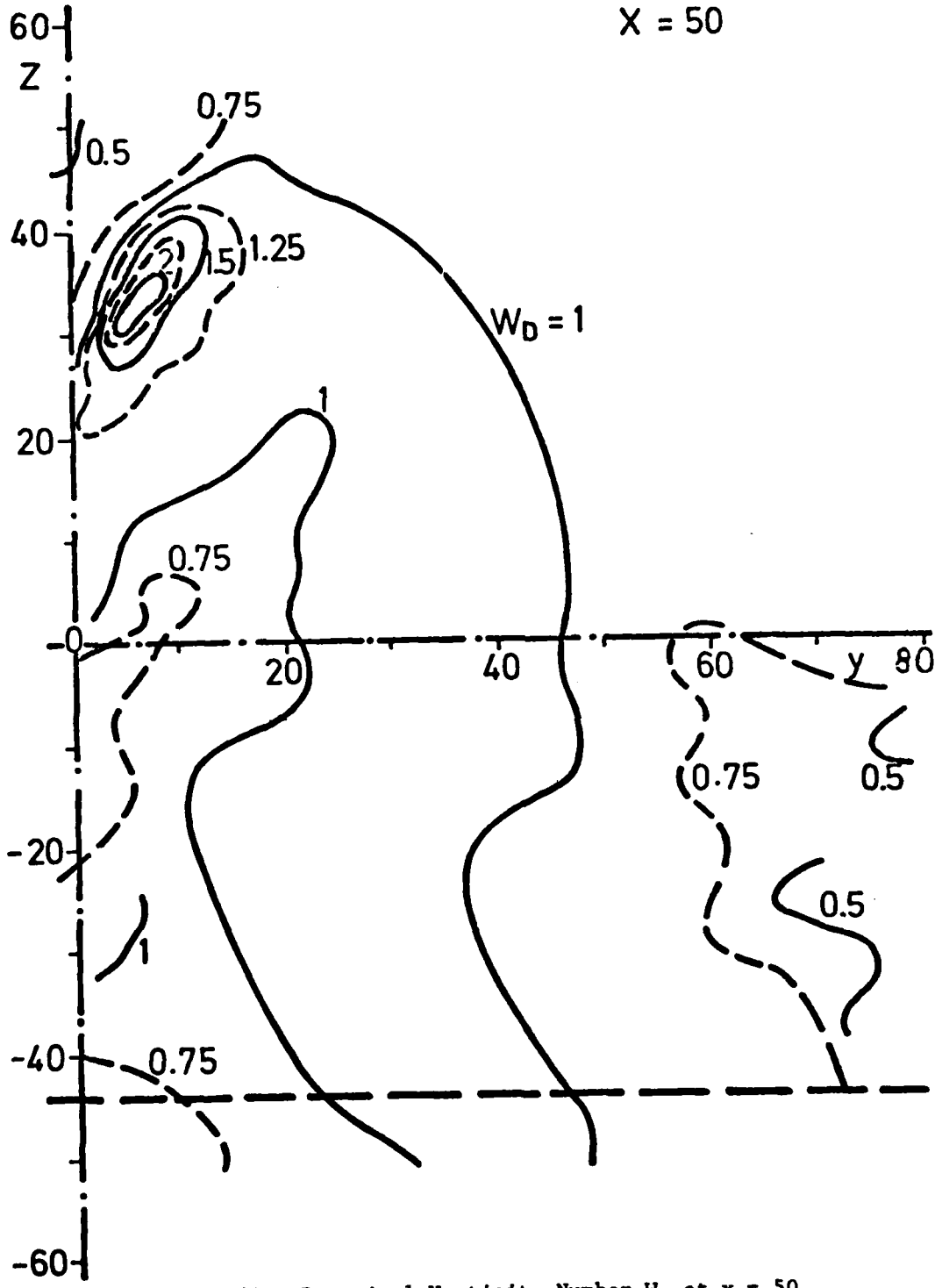

Figure 42 - Dynamical Vorticity Number W_D at x = 50

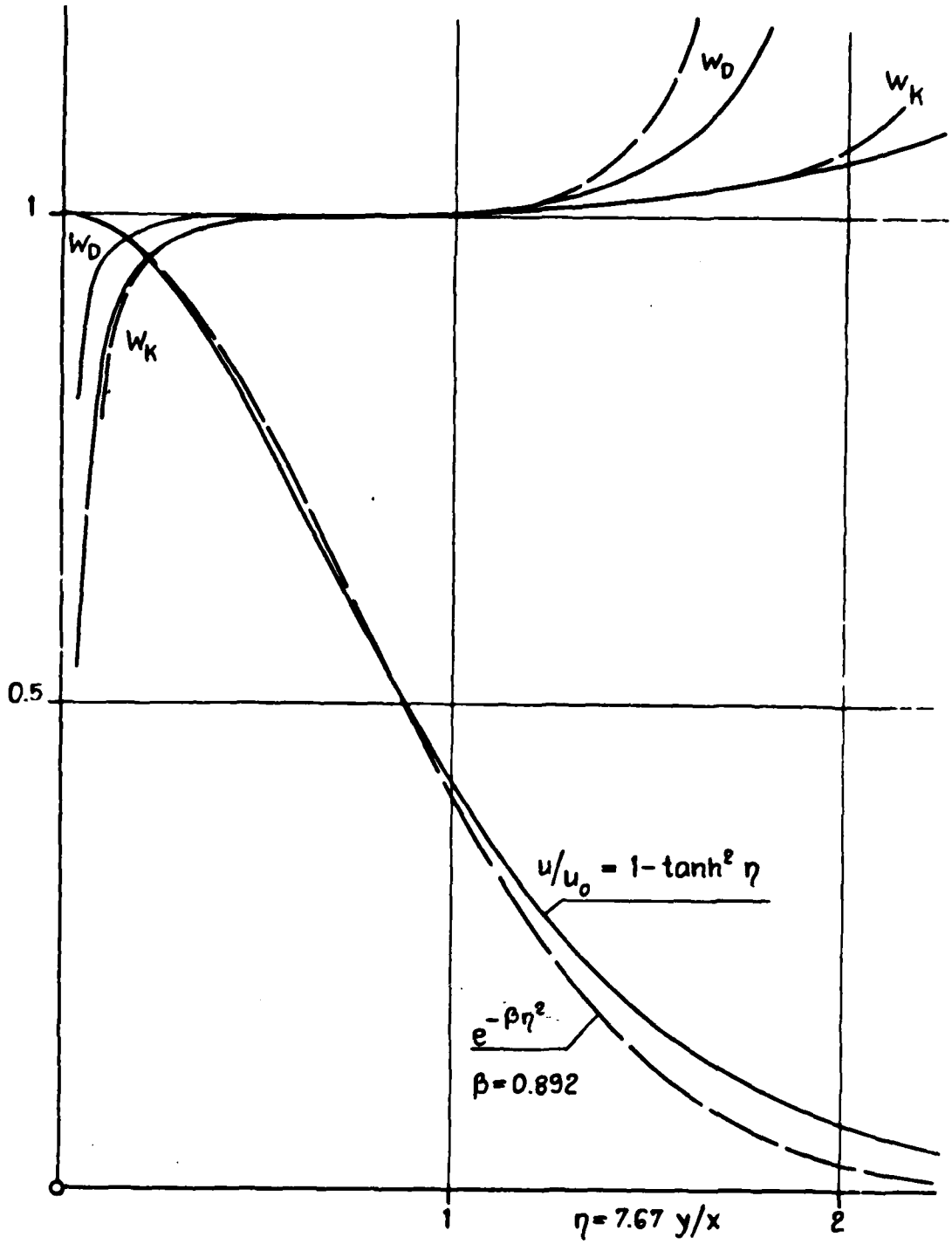

Figure 43 - Turbulent Plane Jet: Vorticity Numbers W_D and W_K for Two Velocity Profiles

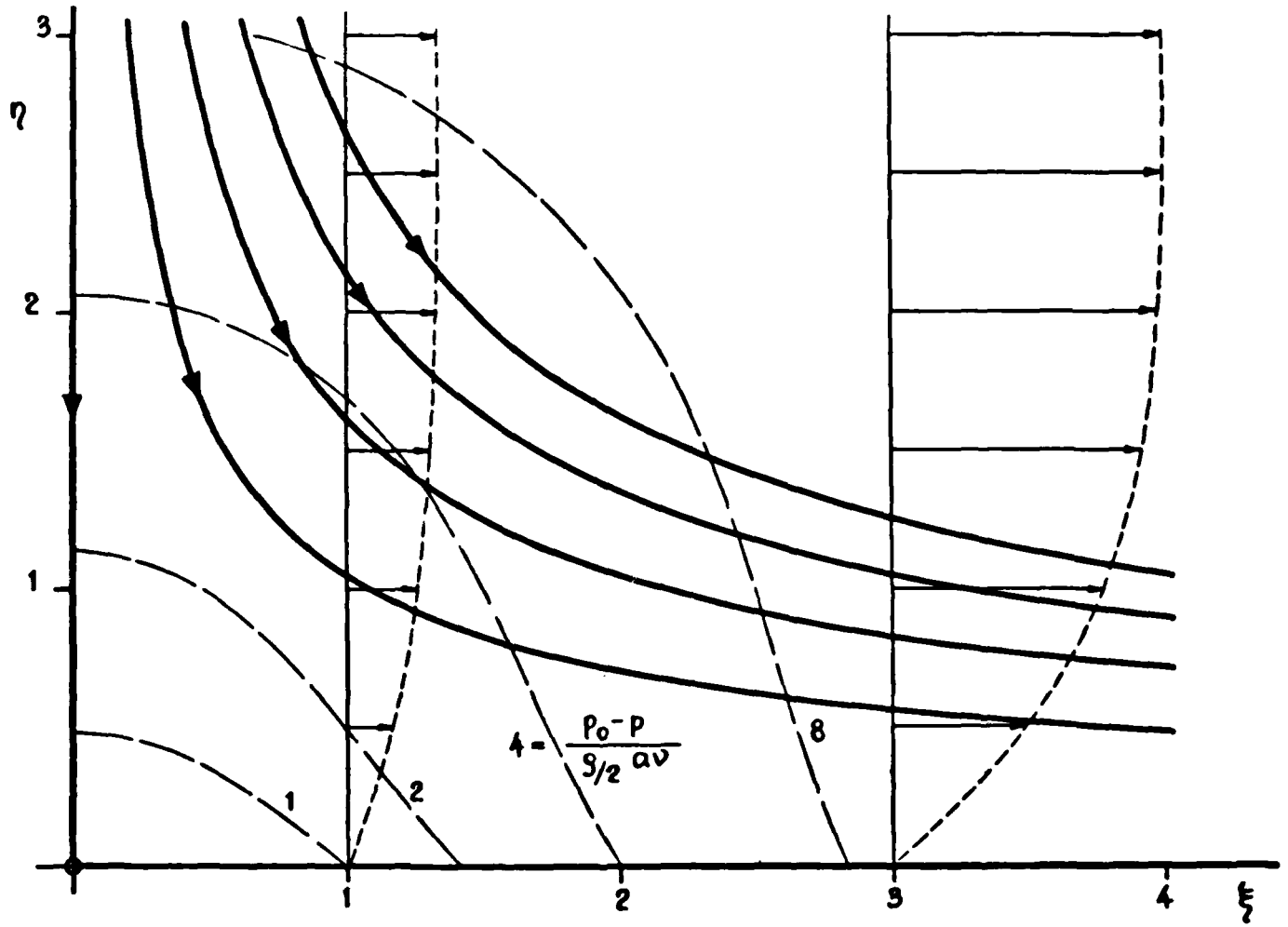

Stagnation - point flow : streamlines, isobars, velocity profile.

$$\psi = v\xi\varphi(\eta) \; ; \quad \xi, \eta = \sqrt{\frac{a}{v}}\, x, y$$

Figure 44 - Laminar Stagnation Point Flow: Streamlines, Isobars, and Velocity Profile

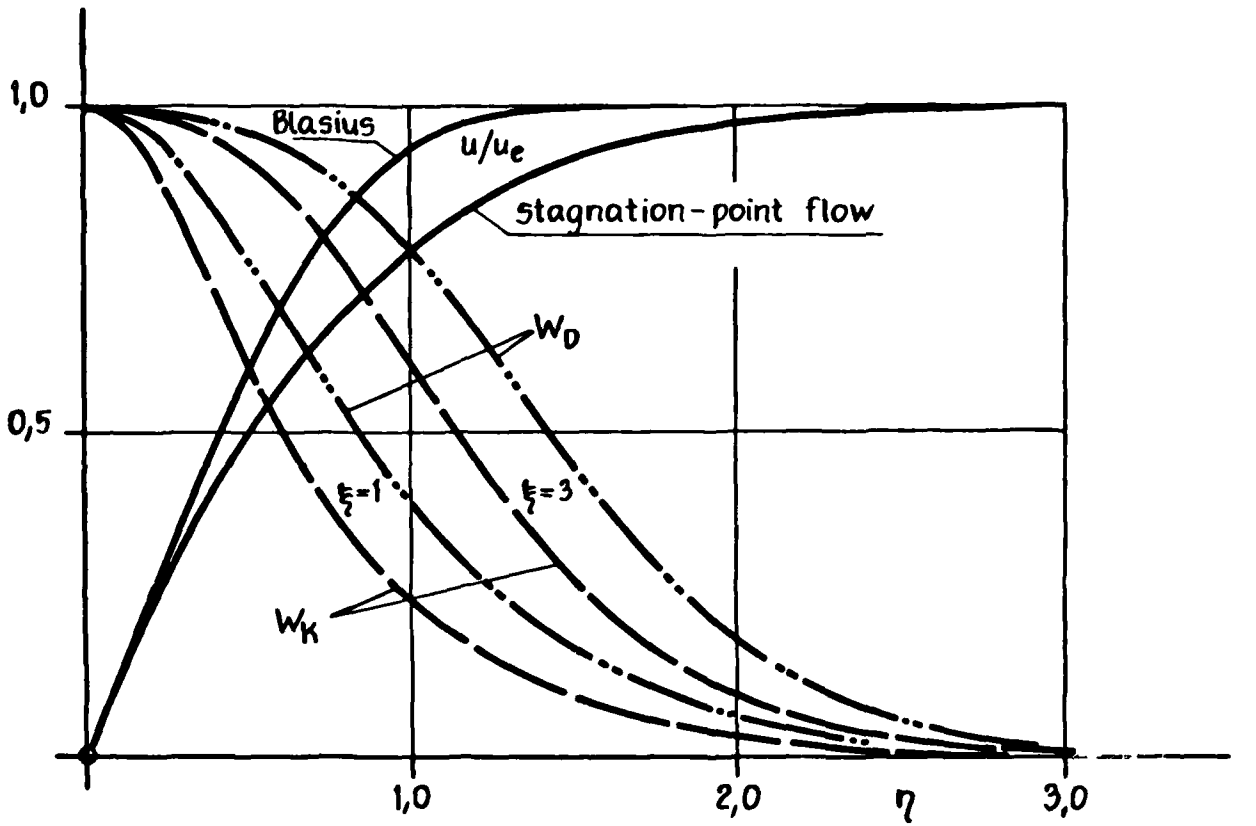

Figure 45 - Laminar Stagnation Point Flow: Vorticity Numbers W_K and W_D

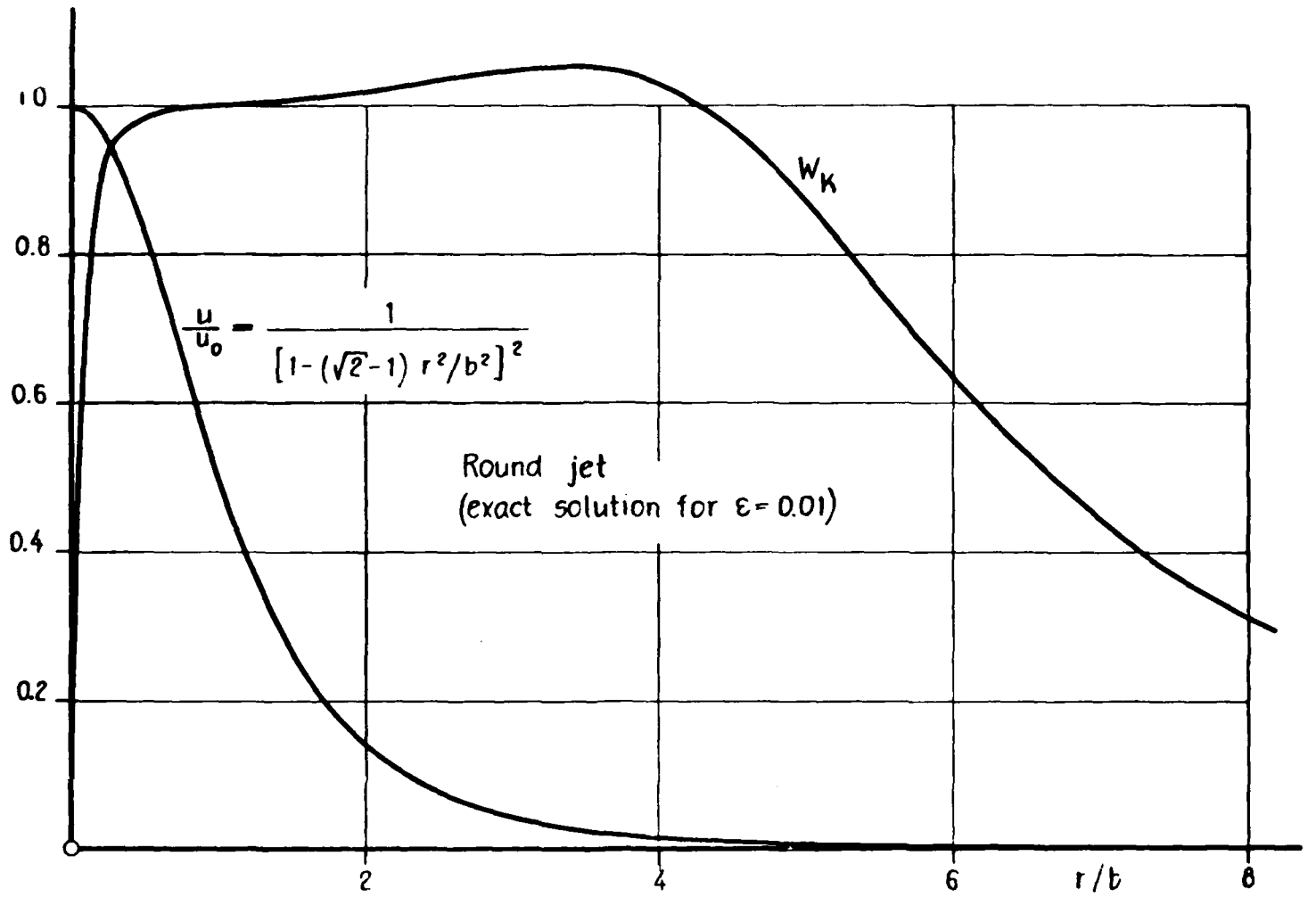

Figure 46 - Round Laminar Jet: Velocity Profile and W_K vs Distance from Axis

APPENDIX

REMARKS ON THE DEFORMATION RATE IN POTENTIAL FLOW

To get used to the deformation rate in incompressible fluid, it might be helpful to consider simple examples from plane potential flow, although here $W_K = W_D = 0$, of course. In general, a plane flow with a stream function ψ has a deformation rate d:

$$d^2 = \omega^2 + 2 \operatorname{div} \vec{a} = (\Delta\psi)^2 + 4 \cdot (\psi_{xy}^2 - \psi_{xx}\psi_{yy})$$

In a potential flow with $\omega = -\Delta\psi = 0$ and $F(z=x+iy) = \phi + i\psi$

$$d^2 = 2 \operatorname{div} \vec{a} = 4(\phi_{xy}^2 - \phi_{xx}\phi_{yy})$$

$$= 4(\psi_{xy}^2 - \psi_{xx}\psi_{yy})$$

$$= 4\, F''\, \overline{F''} = (2|F''|)^2 \geq 0$$

i.e., the deformation rate is simply twice the magnitude of F".

This gives for point singularities such as

$$\text{source } F = \frac{q}{2\pi} \ln z,\ d = |q|/\pi r^2$$

$$\text{vortex } F = \frac{\Gamma}{2\pi i} \ln z,\ d = |\Gamma|/\pi r^2$$

$$\text{dipole } F = m/(2\pi z),\ d = |m|/\pi r^3$$

The addition of a parallel flow $\Delta F = U z$ does not alter F". Hence, the lines of constant deformation rate are circles also for the halfbody or the circular cylinder. For inviscid stagnation point flow $F = a/2\, z^2$, the deformation rate is the same everywhere, $d = 2|a|$.

After conformal mapping $\xi(z)$ one has

$$\frac{d^2F}{d\xi^2} = \frac{1}{(d\xi/dz)^2} \cdot \left\{ \frac{d^2F}{dz^2} - \frac{d^2\xi}{dz^2} \frac{1}{d\xi/dz} \frac{dF}{dz} \right\}$$

For example, the flow around a circular cylinder in the z-plane at an angle of incidence γ

$$F(z) = U(ze^{-i\gamma}/R + Re^{i\gamma}/z)$$

is transformed by $\xi = z + c^2/z$ into that around an ellipse with axes $a = R(1+c^2)$ and $b = R(1-c^2)$. With $\xi = \rho\, e^{i\beta}$ and $c^2 = (a-b)/(a+b)$ the deformation rate d becomes

$$\frac{d}{d_o} = \frac{(1-c^2)^3}{[\rho^4 - 8c^2\rho^2 \cos 2\beta + 16c^4]^{3/4}}$$

with

$$d_o = d_{max} = \frac{U_\infty (a+b)^2}{b^3} \sqrt{1-2c^2 \cos 2\gamma + c^4}$$

For an elliptical strut, $a = 3\ b$ or $c^2 = 1/2$ at $\gamma = 15°$ incidence, lines $d/d_o = \text{const}$ are shown in Figure 47. It is remarkable that only the magnitude of deformation rate depends on the angle of incidence: $d_o(\gamma)$, but the distribution d/d_o is independent of γ! Yet, this holds only for the elliptical strut, as can be shown easily.

On the ellipse itself the deformation rate is proportional to the local curvature of the ellipse, i.e.:

$$d \cdot R_C = 2\ U_\infty (1+b/a) \sqrt{1+(a^2/b^2-1) \sin^2\gamma}$$

with R_C = radius of curvature. Again, this is only true for an elliptical strut. Yet, it is mentioned here because K. Oswatitsch[8] proposed as a vorticity number in plane flow (including compressible flow) the product of local vorticity and radius of curvature of the streamline over velocity: $|\omega| \cdot R_C/U_\infty$. For an elliptical profile this is exactly proportional to $W_K = |\omega|/d$ on the profile itself.

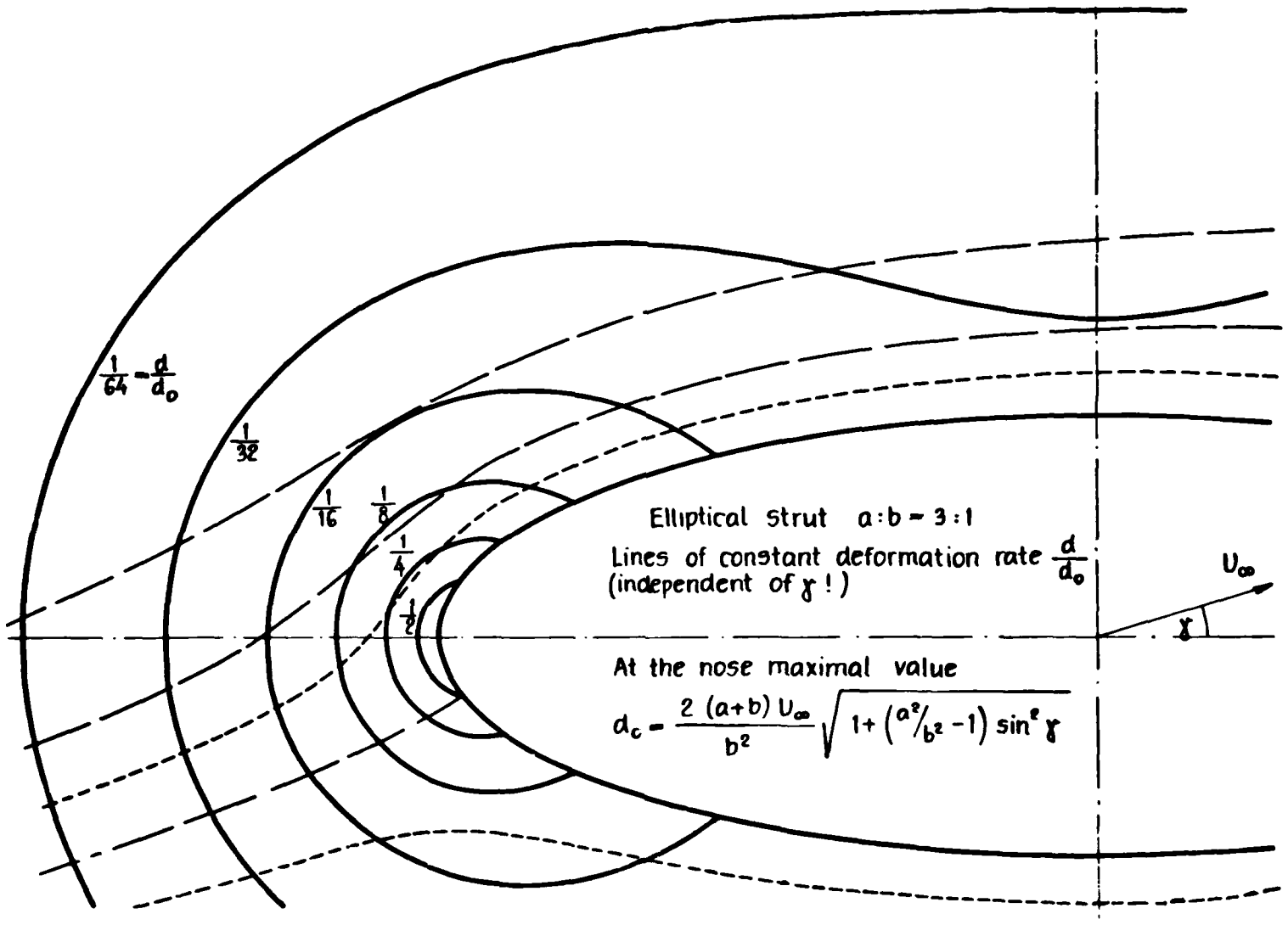

Figure 47 - Elliptical Strut in Potential Flow at Angle of Incidence $\gamma = 15°$: Streamlines and Lines for Constant Deformation Rate

REFERENCES

1. Hoffmann, H.P., "Untersuchung der 3-dimensionalen, turbulenten Grenzschicht an einem Schiffsdoppelmodell im Windkanal," Inst. f. Schiffbau, Hamburg, Ber. 343 (1976).

2. Hatano, S. et al., "Calculation of Velocity Distribution in Ship Wake," J.S.N.A. Japan, Vol. 138 (1975) and Vol. 141 (1977).

3. Winter, K.G. and L. Gaudet, "Turbulent Boundary-Layer Studies at High Reynolds Numbers at Mach Numbers between 0.2 and 2.8," RAE Report and Memorandum 3712 (1970).

4. Wieghardt, K. and J. Kux, "NominellerNachstrom auf Grund von Windkanalversuchen," J.S.T.G. 74 (1980).

5. Truesdell, C., "Two Measures of Vorticity," J. Rat. Mech. Anl. 2 (1953) 173.

6. Schlichting, H., "Boundary Layer Theory," Pergamon (1980).

7. Rosenhead, L., "Laminar Boundary Layers," Oxford (1963).

8. Oswatitsch, K., "Uber Wirbelkennzahlen und Wirbelmaße," ZAMP 20 (1969) 628.

INITIAL DISTRIBUTION

Copies	
1	US Army Waterways Experiment Station Research Center Lib
3	CHONR/Code 432
1	ONR/Boston
1	ONR/Chicago
1	ONR/Pasadena
1	USNA/Lib
1	NAVPGSCOL
1	NROTC & NAVADMINU
1	NAVWARCOL
1	NRL/Lib
6	NAVSEA 1 SEA 003 1 SEA 31B 1 SEA 321 2 SEA 3213 1 SEA 521
1	NAVFACENGCOM
1	NAVOCEANO/Lib
1	NADC
1	NWC
1	NOSC
1	CEL/Code L31
1	NSWC/White Oak/Lib
1	NSWC/Dahlgren/Lib
1	NUSC NPT
1	NUSC NLONLAB

Copies	
1	NAVSHIPYD BREM/Lib
1	NAVSHIPYD CHASN/Lib
1	NAVSHIPYD MARE/Lib
1	NAVSHIPYD NORVA/Lib
1	NAVSHIPYD PEARL/Lib
1	NAVSHIPYD PHILA/Lib
1	NAVSHIPYD PTSMH/Lib
12	DTIC
1	AFFDL/FDDS/J. Olsen
2	AFFDL/FYS 1 Dale Cooley 1 S. J. Pollock
2	COGARD 1 COM (E), STA 5-2 1 Div of Merchant Marine Safety
1	LC/Sci & Tech Div
1	MARAD/Adv Ship Prog Office
1	MMA/Tech Lib
1	NASA AMES RESEARCH CENTER/ R. T. Medan, Ms 221-2
4	NASA LANGLEY RESEARCH CENTER 1 J. E. Lamar, Ms 404A 1 Brooks 1 E. C. Yates, Jr., Ms 340 1 D. Bushnell
1	NASA/Sci & Tech Info Facility
1	NSF/Eng Div

Copies	
1	Univ of Bridgeport Prof. E. Uram Mech Eng Dept
4	Univ of California, Berkeley College of Eng, NA Dept 1 Lib 1 J. R. Paulling 1 J. V. Wehausen 1 W. Webster
3	CA Inst of Tech 1 A. J. Acosta 1 T. Y. Wu 1 Lib
1	Colorado State Univ M. Albertson Dept of Civ Eng
1	Univ of Connecticut V. Scottron Hyd Research Lab
1	Cornell Univ Grad School of Aero Eng
1	Florida Atlantic Univ Ocean Eng Lib
1	Harvard Univ/Dept of Math G. Birkhoff
1	Univ of Hawaii/Dr. Bretschneider
1	Univ of Illinoise/Coll of Eng J. M. Robertson Theoretical & Applied Mech
3	State Univ of Iowa Iowa Inst of Hyd Research 1 L. Landweber 1 J. Kennedy 1 V. C. Patel
1	Kansas State Univ Engr Exp Station/D. A. Nesmith
1	Lehigh Univ Fritz Lab Lib

Copies	
1	Long Island Univ Grad Dept of Marine Sci David Price
1	Delaware Univ/Math Dept
4	Univ of Maryland 1 Eng Lib 1 P. F. Cunniff 1 C. L. Sayre 1 F. Buckley
7	Mass Inst of Tech Dept of Ocean Eng 1 R. Yeung 1 J. R. Kerwin 1 J. N. Newman 1 P. Leehey 1 M. Abkowitz 1 A. T. Ippen/Hydro Lab 1 T. F. Ogilvie
3	Univ of Mich/Dept/NAME 1 Library 1 R. Beck 1 R. B. Couch
4	Univ of Minn/St. Anthony Falls 1 R. Arndt 1 J. M. Killen 1 F. Schiebe 1 J. M. Wetzel
3	City College, Wave Hill 1 W. J. Pierson, Jr. 1 A. S. Peters 1 J. J. Stoker
1	Univ of Notre Dame A. F. Strandhagen
1	Penn State Univ Applied Research Lab
2	SAI/Annapolis 1 N. Salvesen 1 C. von Kerczek

Copies	
3	Southwest Research Inst 1 H. N. Abramson 1 G. E. Transleben, Jr. 1 Applied Mech Review
3	Stanford Univ/Dept of Div Eng 1 R. L. Street 1 B. Perry 1 Dept of Aero and Astro/ J. Ashley
1	Stanford Research Inst/Lib
3	Stevens Inst of Tech/Davidson Lab 1 J. P. Breslin 1 S. Tsakonas 1 Lib
1	Utah State Univ/Col of Eng Roland W. Jeppson
2	Univ of Virginia/Aero Eng Dept 1 J. K. Haviland 1 Young Yoo
2	Webb Institute 1 Lib 1 L. W. Ward
1	Worcester Poly Inst/Alden Research Lab
1	Woods Hole, Ocean Eng Dept
1	SNAME
1	Aerojet-General/W. C. Beckwith
1	Bethlehem Steel Sparrows Tech Mgr
1	Bolt, Beranek & Newman, MA

Copies	
11	Boeing Company/Aerospace Group 1 R. R. Barber 1 H. French 1 R. Hatte 1 R. Hubard 1 F. B. Watson 1 W. S. Rowe 1 T. G. B. Marvin 1 C. T. Ray 1 Commercial Airplane Group 1 P. E. Rubbert 1 G. R. Saaris
1	CALSPAN, Inc. Applied Mech Dept
1	Flow Research, Inc.
1	Eastern Research Group
2	General Dynamics Corp 1 Convair Aerospace Div A. M. Cunningham, Jr. Ms 2851 1 Electric Boat Div V. T. Boatwright, Jr.
1	Gibbs & Cox, Inc. Tech Info Control Section
1	Grumman Aircraft Eng Corp W. P. Carl, Mgr/Grumman Marine
3	Hydronautics, Inc. 1 P. Eisenberg 1 M. P. Tulin 1 R. Barr
4	Lockheed Aircraft Corp Lockheed Missiles & Space 1 R. L. Waid 1 R. Lacy 1 R. Perkins 1 R. Kramer
1	Marquadt Corp/F. Lane General Applied Sci Labs
1	Martin Marietta Corp/Rias

Copies	
3	McDonnel-Douglas Corp/Douglas Aircraft Company 1 Lib 1 T. Cebeci
1	Newport News Shipbuilding/Lib
1	Nielsen, NA Rockwell
1	North American Rockwell Los Angeles Div J. R. Tulinius/Dept 056-015
2	Northrop Corp/Aircraft Div 1 J. T. Gallagher 1 J. R. Stevens
1	Hydromechanics/Paul Kaplan
1	Sperry Sys Mgmt
1	Robert Taggart, Inc.
1	Tracor
1	VPI/J. Schetz

CENTER DISTRIBUTION

Copies	Code	Name
1	012.2	B. V. Nakonechny
1	11	
1	115	
1	1151	
1	1152	
1	1154	
1	15	
1	1502	
1	1504	
1	1505	
1	1506	
1	1507	
2	152	
2	1521	
2	1522	
1	1523	
4	154	
1	1541	
50	1542	
3	1543	
2	1544	
2	156	
1	1561	
2	1562	
2	1563	
1	1564	
1	16	
1	167	
1	169	R. J. Englar
1	17	
1	18	
1	1802.1	
2	1843	
1	1843	H. Cheng
1	19	
1	1966	Y. Liu
1	273	
1	2732	
10	5211.1	Reports Distribution
1	522.1	Library (C)
1	522.2	Library (A)

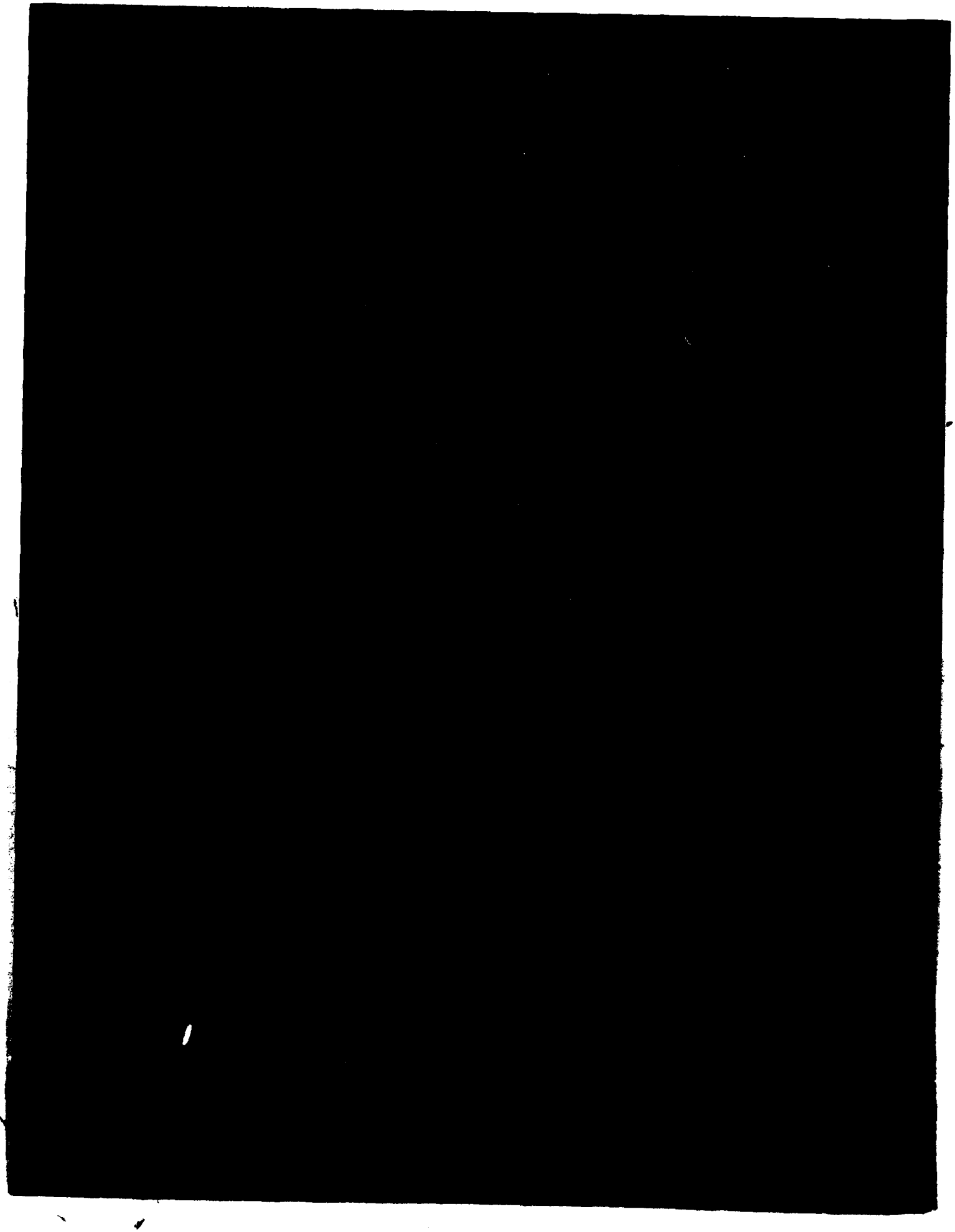


DATE
ILME